



UNIVERSITÀ
DEGLI STUDI
FIRENZE

Scuola di Ingegneria

Corso di Laurea Magistrale in
Ingegneria Energetica

“Sviluppo di un metodo di riduzione dati sperimentali e di un modello bifasico di una turbina Tesla per fluidi organici”

**“Development of an experimental data reduction
method and a two-phase model of a Tesla turbine
for organic fluids”**

Candidate
Giovanni Sarti

Tutor
Prof. Daniele Fiaschi
Ing. Lorenzo Talluri

Co-tutor
Prof. Vincent Lemort
Ing. Olivier Dumont

Acknowledgment

First of all I want to thank prof. Fiaschi for the opportunity given to me, it was a wonderful experience doing the internship in Liège that made me grow as a man and as an engineer. Thank you Lorenzo Talluri for all the support and the incredible availability during my internship and all of my thesis. I'd like to thank also Prof. Vincent Lemort, Olivier Dumont and all of the "Thermodynamic laboratory" of University of Liège for support, welcome and friendship during my experience; especially I want to thank Nicolas Leqlerq for help and availability in Liège but also in remote way during Covid-19 lockdown. Thanks to my friends Francesco N., Edoardo, Andrea, Mattia, Matteo, Haji, Leonardo, Marco, Francesco S., Luigi and all the others who make the world around me an interesting and happy place . Thanks to Tommaso B. and Tommaso M. who made me live these University's years with joy and laugh. A special thanks to my family, to my parents who have taught me the life leaving me the freedom of mistakes, you are the best example I could have ever had. Last but not least I want to thank Giulia for your support during this work, for love you give me every day; you helped me to go beyond my limits to follow my dreams and every day you grow inside my heart a great desire to dream together always looking for new challenges and adventures...love you!

Abstract

Over the last years, the increase in energy consumption coupled with ever more stringent regulations on pollutants emissions and the massive advent of renewables in the energy market, have promoted the development of distributed energy systems and thus of an increasing interest towards small and micro power generation systems. In this context, the ORC progressively became the leading technology in the field of low size energy conversion systems (<100 kW) and low temperature applications ($<150^{\circ}\text{C}$). Nonetheless, this technology still deserves further developments, especially regarding the design of specific components, which should grant features of reliability, acceptable performance level and, often even more important, affordable price in order to ensure the attractiveness of the whole energy system. It is the case of the small and micro expanders (tens to few kW scale). A possible solution for micro-size expanders is the Tesla expander, which is a viscous bladeless turbine that holds the desired characteristics of low cost and reliability. This expander was first developed by N. Tesla at the beginning of the 20th century, but it did not stir up much attention due to the strong drive towards large centralized power plants, where this technology becomes no longer competitive against those belonging to bladed expanders. In the recent years, due to the increasing appeal towards micro power generation and energy recovery from wasted flows, this cost effective expander technology rose a renovated interest.

In the present study, a Tesla prototype projected by University of Florence was taken into account for an experimental campaign for an ORC application using R1233zd(E) as working fluid. This campaign has been conducted in 2018 and its results were considered for the first section of this study to perform a data reduction method which makes a data oscillation around the standard deviation allowed by the instrument and finds solutions which respect the energy balance with a very small error.

These tests were made at University of Liège, so first of all the test bench and data acquisition platform (Labview) are explained, results are loaded in an Excel file that is used in the data reduction code. The code is elaborated in Matlab and is inspired by a method called “Reconciliation method”. Results show a good energy balance’s solution for most of thermodynamic configurations tested and sometimes mean values and reconciled values are very different, this method can therefore avoid having results affected by gross errors.

The experimental campaign conducted in 2018 showed a very low efficiency caused especially by blocking, windage and pumping losses.

Consequently, it’s planned to modify the prototype taking off the thinner disks (0,8 mm) to provide an easier entrance for the flow in the rotor in order to reduce all of the losses.

This “new” prototype could be useful for a two-phase flow; so the second section of this study is about possible two-phase Tesla applications and also a thermo fluid dynamic model developed in EES.

There are many two-phase applications like for example ORC, but the prototype built at the end of this research is going to be used as a lamination valve in a refrigeration cycle or in a heat pump in order to improve the energy efficiency of the cycle.

The model developed in EES is divided in four main sections: nozzle profile, stator, stator-rotor coupling model and rotor. A separated flow model has been used for stator and rotor, discretizing these components in sections on which separated model’s equations were applied.

Abstract

Model's results highlights stator's importance: especially when stator exit velocity is high, rotor's performances have an influence lower and lower, also if a good match between tangential and peripheral velocity at rotor exit remain a crucial parameter to have satisfactory turbine's performances.

Table of contents

Acknowledgment	2
Abstract	3
Nomenclature	7
1 Introduction.....	10
1.1 Objective and structure.....	10
1.1.1 Objective	10
1.1.2 Structure.....	10
2 Literature Review.....	11
2.1 Overview of Organic Rankine Cycle	11
2.2 ORC State of the art	14
2.2.1 Overview of ORC market	14
2.2.2 ORC architectures	17
2.2.3 Working fluid selection.....	20
2.2.4 Expander assessment.....	23
2.2.5 Micro expanders.....	24
2.3 The Tesla turbine	28
2.3.1 Principle of operation.....	28
2.3.2 Typical configurations	28
2.3.3 The ORC prototype	30
3 The experimental campaign	34
3.1 Test bench.....	34
3.2 Turbine maintenance and issues	36
3.3 Labview	38
3.3.1 Labview code University of Liege.....	40
3.3.2 Conduction of tests.....	43
3.4 Global methodology to handle experimental data.....	44
3.4.1 Introduction	44
3.4.2 Reconciliation Method	44
3.4.3 Methodology	45
3.4.4 Reconciliation method-Application	52
3.5 Experimental Results.....	58
3.5.1 Reconciliation method's effects	58
3.5.2 Reconciled results	61
3.6 Future prototype development.....	66

4	Two-phase model	67
4.1	Possible applications	67
4.2	2D model developed in EES	74
4.2.1	Nozzle Profile	75
4.2.2	Stator model	77
4.2.3	Stator–rotor coupling model	81
4.2.4	Rotor model.....	84
4.3	Two phase model results	91
4.3.1	Component analysis	91
4.3.2	Individual variables optimization.....	91
4.3.3	Combined variables.....	95
4.3.4	Tangential velocity ratio	98
4.3.5	Compactness and rotational speed	99
5	Conclusions and Recommendations	100
5.1	Conclusions	100
5.2	Recommendations	101
	Bibliography.....	102

Nomenclature

\dot{m}	Mass flow rate [kg/s]	P	Power [W]
W	Power [W]	p	Pressure [Pa]
A	Area [m^2]	Q	Heat [W]
A_x	Radial distance from center [m]	Q	Control Volume [m^3]
b	Channel height [m]	r	Radius [m]
b	Bottom-line [m]	Re	Reynolds number [-]
C	Chilsom parameter	rpm	Revolution per minute
C_c	Contraction coefficient	SH	Super heating level [$^\circ C$]
CF	Compactness factor [W/cm^3]	SS	Speed of sound [m/s]
Chord	Chord [m]	t	Time [s]
Constr.	Constraints [W]	T	Temperature [$^\circ C$]
c_p	Specific heat	TW	Throat width [m]
D	Diameter [m]	u	Peripheral velocity [m/s]
d	Distance [m]	u	Up-line [m]
Dh	Hydraulic diameter [m]	ubm	Mean-line [m]
E	Kinetic energy [J/kg]	v	Absolute velocity [m/s]
EES	Engineering Equation Solver	V	Volume [m^3]
EoS	Equations of State	w	Relative velocity [m/s]
Eta	Efficiency	W	HR Waste Heat Recovery
f	Body force per unit mass [m/s^2]	x	Quality[-]
f	Friction factor [-]	X, Y	Cartesian coordinates
F	Force [N]	Z	Number of nozzles [-]
G	Gap [m]		
h	Specific enthalpy [J/kg]		
H	Height [m]		
I	Specific Rothalpy [J/kg]		
M	Moment [Nm]		
m	Angular coefficient [-]		
Ma	Mach number [-]		
n_{ch}	Number of Rotor channels per Stator		
NR	Total number of rotor discretization		
ORC	Organic Rankine Cycle		

Greek symbols

α	Absolute flow angle [$^\circ$]
α	Flow type modulus [-]
β	Expansion ratio [-]
β	Relative flow angle [$^\circ$]
ε	Void fraction [-]
η	Efficiency [-]

θ	Tangential direction	n	Number of element
μ	Dynamic viscosity [kg/ms]	pack	Stator package
ν	Kinematic viscosity [m^2/s]	perp	Perpendicular
χ	Lockart-Martinelli parameter [-]	out	Outlet
ϕ	Two-phase frictional multiplier [-]	r	Radial direction
ρ	Density [kg/m^3]	r	Relative
σ	Standard deviation	rt	Rotor
σ_t	Tangential velocity ratio [-]	s	Stator
σ_a	Area ratio [-]	st	Stator
τ	Wall shear stress [Pa]	su	Superior
ω	Angular speed (rad/s)	t	Tangential
Subscripts and superscripts		Tesla	Total to static
$0x$	Total condition at section x	th	Thermodynamic
0	Stator inlet value	tot	Total
1	Stator outlet value	tp	Two-phase
2	Rotor inlet value	u	Utilization
3	Rotor outlet value	up	Upper bound
ch	Channel	v	Vertical
c	Contraction	viol	Violation
e	Fluid element	w	Wetted
e	Enlargement	w	Weight
ex	Exit	xs	Static and isentropic reaching x-section
exp	Expander	z	Axial direction
g	Gas		
h	Hydraulic		
i	Discretization step		
in	Inlet		
kin	Kinetic		
l	Liquid		
lb	Lower bound		
loss	Losses		
mech	Mechanic/Shhaft		
N	Nozzle		

1 Introduction

The world scenario recently experienced a strong increase in energy consumption demand, associated with a series of issues related to the exhaustion, environmental impact and cost of the resources, especially for fossil fuels. This framework encourages the search of alternative energy solutions for power generation, as well as the improvement of already existing conversion systems. Over the last years, research on energy systems has focused on small, distributed systems for cogeneration, which cover the requirements of heat and power generation both in domestic buildings and industrial facilities, with an emphasis on smart grid solutions which can effectively deal with problems of load/generation mismatch and integration of energy storage. When applied to intermediate and low-temperature resources, a modern popular technology is the Organic Rankine Cycle, whose applications are being extended to small size (5–50 kWe). This technology substitutes water with organic-based compounds as working fluid. The main advantage of these fluids is that they are suitable for low temperature applications, as they allow moderate saturation temperatures and pressures and high molecular mass. Indeed, several studies were performed on ORCs applied to low-medium temperature thermal resources. Such applications range from recovery of heat from gas turbine discharge, internal combustion engines or industrial waste heat, energy conversion from biomass, solar or geothermal resources represent another common field of application. Nonetheless, when micro applications are taken into account, one of the main issues with Organic Rankine Cycles is linked to the expander, as this component often involves high manufacturing costs and offers low reliability. The Tesla turbine, with its relatively simple structure, appears to be a potentially reliable and low-cost expander, which could find its market in the low-power range. Organic Rankine cycle is not the only application for a Tesla turbine because for example it can be useful in a refrigeration cycle because is less bulky than a turbine but more efficient than a lamination valve so the compressor work can be reduced.

1.1 Objective and structure

1.1.1 Objective

The first objectives of this study were a repeatability of test conducted with a prototype in Liège and then conducting a second experimental campaign modifying the prototype. Several issues didn't allow to conduct this experimental campaign, so the objectives were modified and explained below.

1. Development of a data reduction method that finds solutions which respect the energy balance with a very small error.
2. Development of a numerical 2D model which allows the prediction of the performance of a Tesla turbine for a two-phase application.

1.1.2 Structure

The thesis is comprised of five chapters, including the initial introduction chapter.

Chapter 2 is dedicated to the literature review, where the “state of the art” of the Tesla turbine researches is assessed. Furthermore, a brief introduction on ORC technologies is presented, with a particular focus on micro expanders. At the end of the chapter the principle of operation of Tesla turbines is reported with a description of the prototype taken into account.

Chapter 3 is dedicated to a data reduction method (“Reconciliation method”) considering results of an experimental campaign conducted in 2018. First of all, test bench and acquisition method are explained; then there’s a section about the Reconciliation method developed in Matlab and at the end the results.

Chapter 4 is dedicated to the numerical 2D model which allows the prediction of the performance of a Tesla turbine for a two-phase application. The model is developed in EES (Energy Equation solver) and at the end of the chapter the results leads to optimizing geometric parameters.

Chapter 5 is dedicated to the conclusions of this research and recommendations for future work.

2 Literature Review

2.1 Overview of Organic Rankine Cycle

In order to have of a clear understanding of the reasons of the rising of interest of the ORC technology, a comparison with traditional power generation systems both from a thermodynamic and a Turbomachinery points of views needs to be carried out. First of all, a distinction of power production technologies is given by the architecture of the cycle, “open” or “closed”. In open cycles the working fluid experiences material exchanges with the environment, both at inlet and outlet of the cycle; an example is the gas turbine cycle, utilizing air as working fluid. Closed cycles, on the other hand, are characterized by a working fluid that consecutively operates a cyclic series of thermodynamic transformations; an example is the Rankine (or the Hirn) cycle, which uses water (steam) as working fluid. Another important aspect to remark is the possible transformations that can take place in a power generation system with external heat sources (excluding therefore internal combustion engines), which are: nearly adiabatic transformation (typically, in pumps, compressors and turbines/expanders) and nearly isobaric transformations (typically, in heat exchangers). Cherishing the above-mentioned difference in cycle architectures and the possible thermodynamic transformations, the open-air cycle will be first analyzed through second law efficiency assessment. Assuming a fixed constant temperature for the heat source and a fixed ambient temperature of a simple open cycle, the cycle efficiency can be expressed as shown in Eq.(2.1)

$$\eta = \left(1 - \frac{T_0}{T_{max}}\right) - (T_0 \sum_i^N \frac{\Delta S_i}{Q_{in}})$$

(2.1)

$\eta = \left(1 - \frac{T_0}{T_{max}}\right)$ is known as the “Carnot” efficiency, which is the upper limit that any traditional thermodynamic cycle can achieve;

$(T_0 \sum_i^N \frac{\Delta S_i}{Q_{in}})$ is the sum of the losses related to each cause of irreversibility.

Particularly, the second term of Eq.(2.1) can be decomposed in 8 main losses, as suggested in [1] and shown in Fig. 2.1(corresponding color in bracket near losses bullet point):

- pressure losses (red);

- fluid-dynamic losses in compressor (green);
- heat transfer losses in the heat introduction process (purple);
- fluid-dynamic losses in expansion process (azure);
- losses due to mixing of hot air to atmosphere (orange);
- heat transfer losses in the heat introduction process (purple);
- fluid-dynamic losses in expansion process (azure);
- losses due to mixing of hot air to atmosphere (orange);
- heat losses to the environment (royal blue);
- mechanical/electrical losses (light red);
- heat transfer losses in the recuperator (if present, light green).

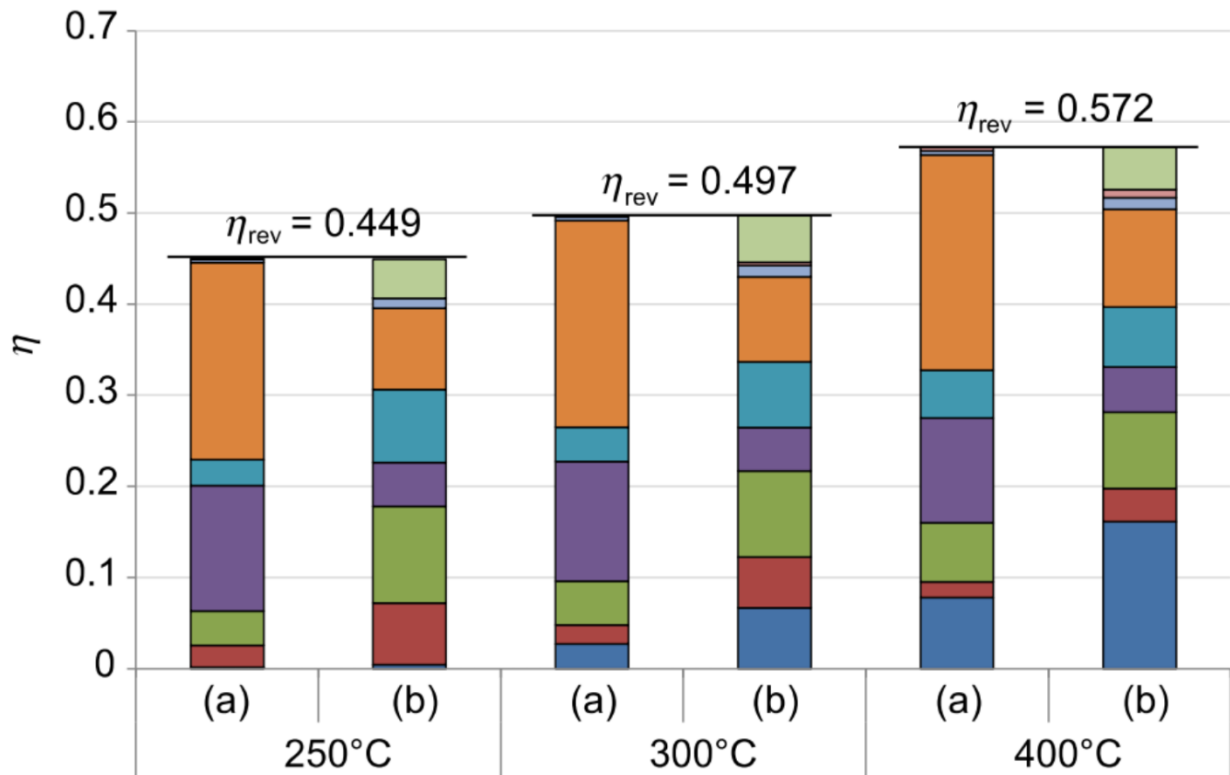


Fig. 2.1

As can be noted from Fig. 2.1, the second law efficiency for open cycle architecture decrease drastically for lower temperatures, due to the increasing of the various losses. Comparing gas cycles to closed-loop Organic Rankine cycles for temperature values below 400°C, the advantages of the ORC solution are quite relevant. First, a better coupling of both high and low temperature heat transfer processes can be realized more easily; in subcritical Rankine cycle, evaporation and condensation processes take place, allowing for large parts of transformations a constant temperature heat exchange. This feature is particularly appreciated for heat transfer with the environment, which often requires a relevant heat capacity, and it ensures a major lowering of the irreversibility in the process of heat transfer. Furthermore, pressurization of the cycle can be obtained using pumps (liquid conditions) instead of compressors (gas conditions), reducing greatly the amount of work required (and the irreversibility in the process). Taking as reference the analysis conducted in [1], where three different fluids (water, benzene and MDM) were utilized in order to estimate the efficiency of a Rankine cycle with an upper resource temperature of 240°C, it can be claimed that Rankine cycles can reach efficiency which are closer to the upper Carnot limit when compared to gas cycles. Particularly, as shown in Fig. 2.2, the reachable efficiencies by a

Rankine cycle are in the range of 70–85% of the maximum achievable efficiency (compared to the 30% in the case of the gas cycle). Particularly, it is seen, that even if the three fluids have very different molecular structures, the achievable cycle efficiency (when recuperated architecture is utilized) is very close between one and another. The assumed conditions for the analysis conducted in [1] are resumed in Tab 2.1.

Variable	Assumed value
Ambient Temperature	15°C
Condensation Temperature	30°C
Evaporation Temperature	240°C
Pump efficiency	0.85
Turbine efficiency	0.85
Pressure losses	10% of evaporation pressure
Thermal losses	1% of heat input
Mechanical/electrical efficiency	95%

Tab 2.1: Conditions assumed for the analysis conducted

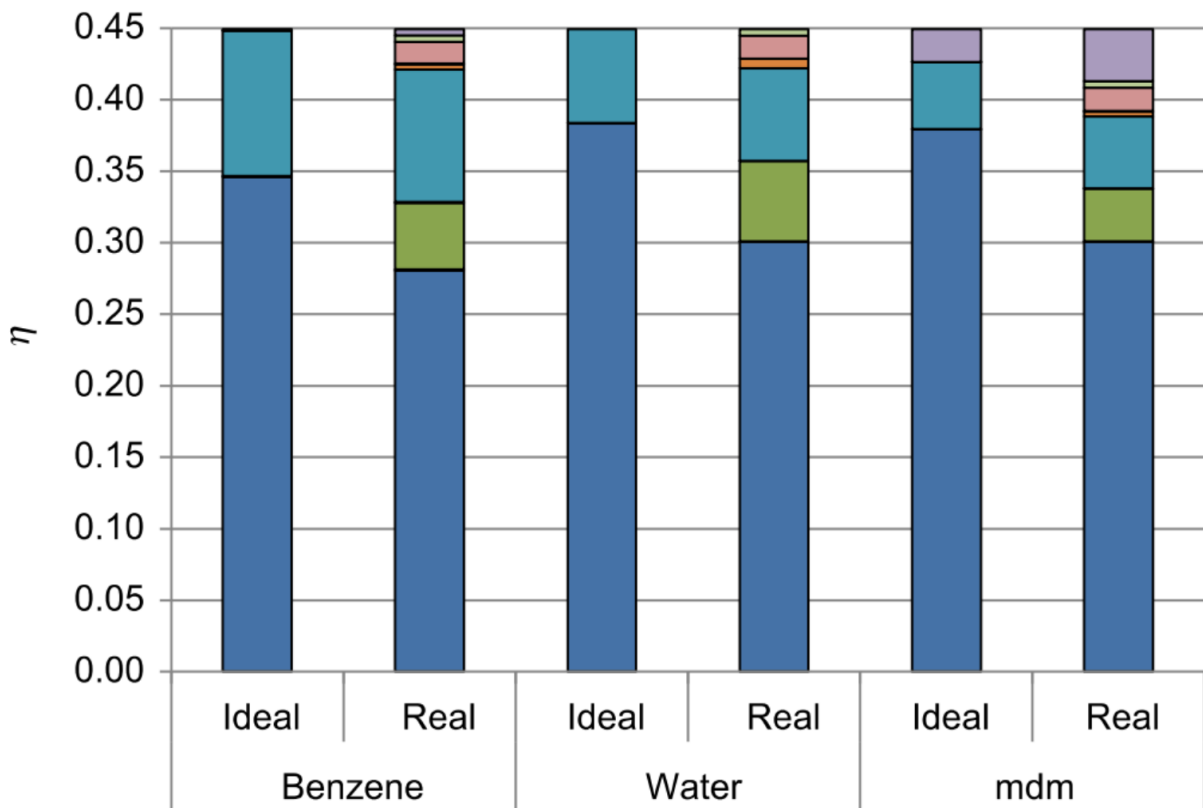


Fig. 2.2 :Second law efficiency (dark blue) for three different saturated Rankine (ideal and real) cycles with assumed condition resumed in Tab. 2.1 The cycle losses represented consider: fluid–dynamic losses in pump (red), fluid–dynamic losses in turbine (green), pressure losses (purple), heat transfer losses in the liquid preheating (azure), heat transfer losses in the evaporation process (orange), heat transfer losses in the heat rejection to environment (royal blue), mechanical/electrical losses (light red), heat losses to the environment (light green), heat transfer losses in the recuperator (light purple)

After the comparison between gas cycles and Rankine cycle for low temperature heat sources, the reasons why organic fluids are preferable to water for low-temperature energy resources are highlighted. The first issue when dealing with the steam Rankine cycle for low temperature application is the wet expansion process. Indeed, as displayed in Fig. 2.3, the expansion of a saturated cycle is within the liquid–vapor dome, on the other hand, for organic compounds, with

higher molecular complexity (increasing molecular complexity modify the inclination of the vapor curve, known also as backward vapor line) the expansion can be dry, which will guarantee that no blade erosion issue will present. Furthermore, in the steam Rankine cycle, in order to have high turbine performances, the expander design is very costly, as a correct design will involve multi-stage turbine, with variable speed shafts. Indeed, for low power ranges the construction of an efficient steam expander becomes very difficult, as the steam flow rate would be drastically small with conversely relatively a high expansion ratio. Also, the development of steam volumetric expanders is subject to many negative issues, especially regarding the complexity of the expander (appropriate lubrication system, high friction losses, difficulty to realize an adiabatic expander).

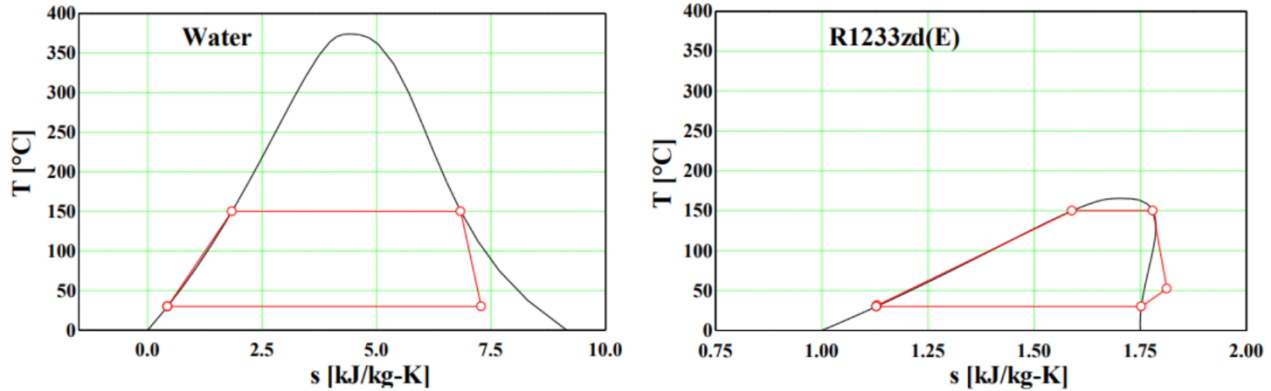


Fig. 2.3: Temperature – Entropy diagrams of saturated Rankine cycles for Water and R1233zd(E);
Evaporator temperature of 150°C, Condensing temperature of 30°C

Once the thermodynamic (when compared to gas cycle) and turbomachinery (when compared to steam Rankine cycle) advantages of ORC for low temperature heat resources have been assessed, a comprehensive review on the applications, working fluid selection and expanders utilized is required in order to fully grasp the strong and weak points of this technology, as well as its maturity level.

2.2 ORC State of the art

2.2.1 Overview of ORC market

The first concept of the ORC technology was developed by T. Howard in 1826 [2], developing a system to produce 18 kW of energy with ether as working fluid. After the first spark, ORC technology started being extensively investigated, but at first it was confined to niche markets, as the safety conditions of the power plants were not adequate. Therefore, it took a whole century before the first example of “modern” ORC was realized by D’Amelio at University of Naples [3], [4]. Specifically, the developed ORC utilized solar energy as heat source for single stage turbine running with ethyl chloride as working fluid. Finally, it is in the 1960s that ORC finally bloomed thanks to the research work of Tabor and Bronicki (founder of Ormat technologies) at the National Physical Laboratory in Israel and of Angelino, Macchi and Gaia (this last founder of Turboden Ltd.) at Politecnico di Milano. ORMAT was founded in 1964 and Turboden in 1970. These two companies are still today the biggest players in the ORC market. In more recent years, many new companies have been established; a list of the major manufacturers, as well as the total number of installed units and capacities is shown in Tab 2.2.

Manufacturer	ORC units	Total [MW]	Manufacturer	ORC units	Total [MW]
ABB	2	3.8	gt – Energy Tech	2	0.7
Adoratec	23	16.4	Johnson Control	1	1.8
BEP – E– rational	20	3.6	Kaishan	40	27.2
Canetix /CETY	50	6.3	Opcon	3	2.0
DurrCyplan	6	1.2	Orcan	16	0.3
Electratherm	55	3.14	ORMAT	1102	1701
Enerbasque	3	0.13	Rank	5	0.07
Enertime	2	1.6	TAS	17	143
Enex	1	9.3	TMEIC	1	1
Enogia	11	0.26	Triogen	37	5.2
Exergy	34	300	Turboden	267	363
General Electric	6	101	UTC Powr	10	2.8
GMK	18	5.3	Zuccato	21	1.7

Tab 2.2: List of manufacturers, data updated at 31st December 2016

In [3] an interesting study on the current ORC market was developed, assessing the total installed capacity (updated at 31st December 2016) at around 2701 MW for a total of 1754 ORC units. The many fields of applications were also considered and resumed as shown in Fig. 2.4. One of the main and unparalleled advantages of ORC technology is that it is adaptable to any heat resource, allowing its application in many fields: from heat recovery applications at gas turbine discharge [5], [6], [7], or in internal combustion engines [8] or industrial waste heat [9], [10], to energy conversion from renewables such as biomass [11], solar [12], [13], geothermal resources [14], [15], as well as to micro-scale CHP units [16], [17], [18], [19]. Furthermore, the ORC technology allows also the harnessing of ocean thermal power gradient (OTEC) [20].

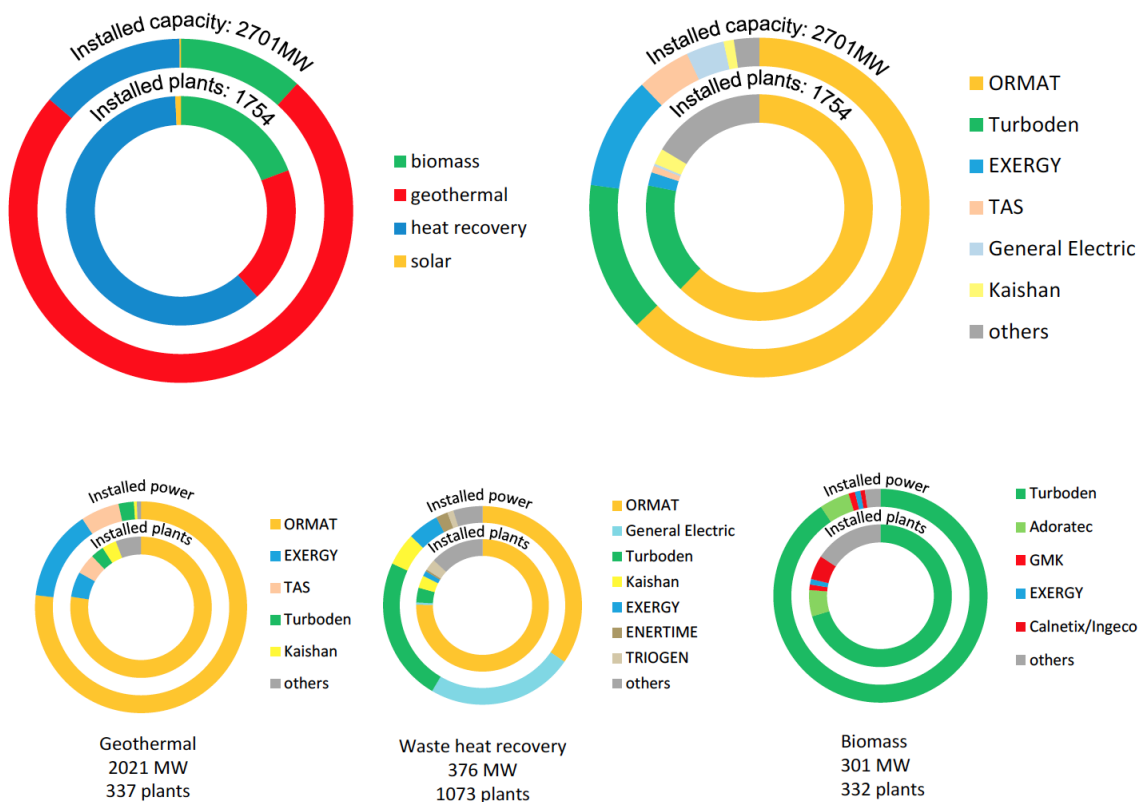


Fig. 2.4: Market share per application and per manufacturer

As can be noted from Fig. 2.4, Ormat is the leader in ORC technologies and the principal application to which this technology is associated is energy conversion in geothermal power plants (especially in the USA where the total installed capacity of geothermal ORC plants is about 750 MW).

Nonetheless, another application, which is emerging in the last few years, is related to industrial waste heat recovery. In this field, ORMAT is still the principal manufacturer, but the supremacy is not defined, as both General Electric and Turboden owns a considerable share of installed power. Actually, the main application in the heat recovery field is recuperation from Diesel engines or gas turbines exhaust gases, as shown in Fig. 2.5. It is to be remarked that there is still plenty of room for expansion in this sector, as witnessed by the low share in energy intensive industries such as metal, cement and glass sectors. Finally, the evolution of the total installed ORC capacity is being displayed in Fig. 2.6. Particularly, it is interesting to note how the global energy prices, represented by the crude oil prices directly influences the ORC market. Before XXI century, ORC technology was basically only applied to geothermal application, but as the crude oil prices started rising and environmental issues emerged, these new technologies started expanding in the other sectors, especially in the biomass heat recovery applications.

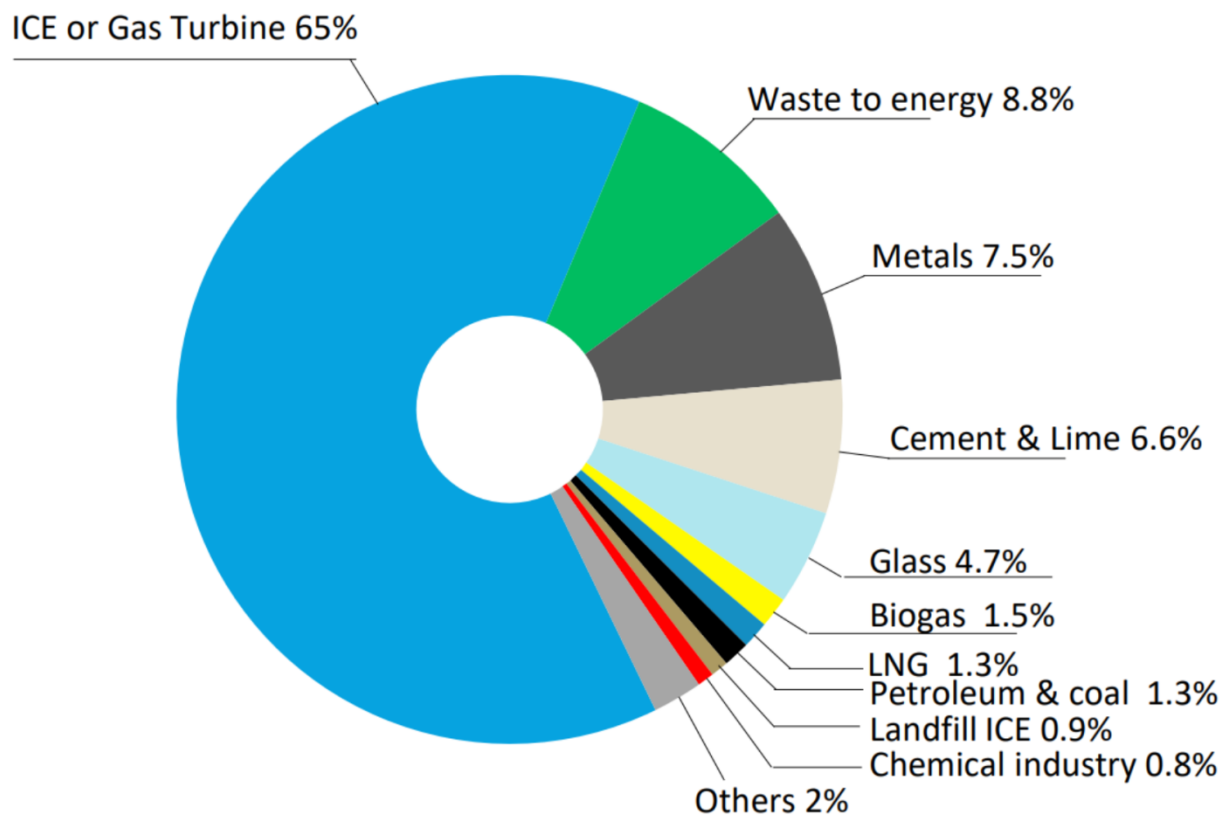


Fig. 2.5: Installed capacity share in heat recovery application

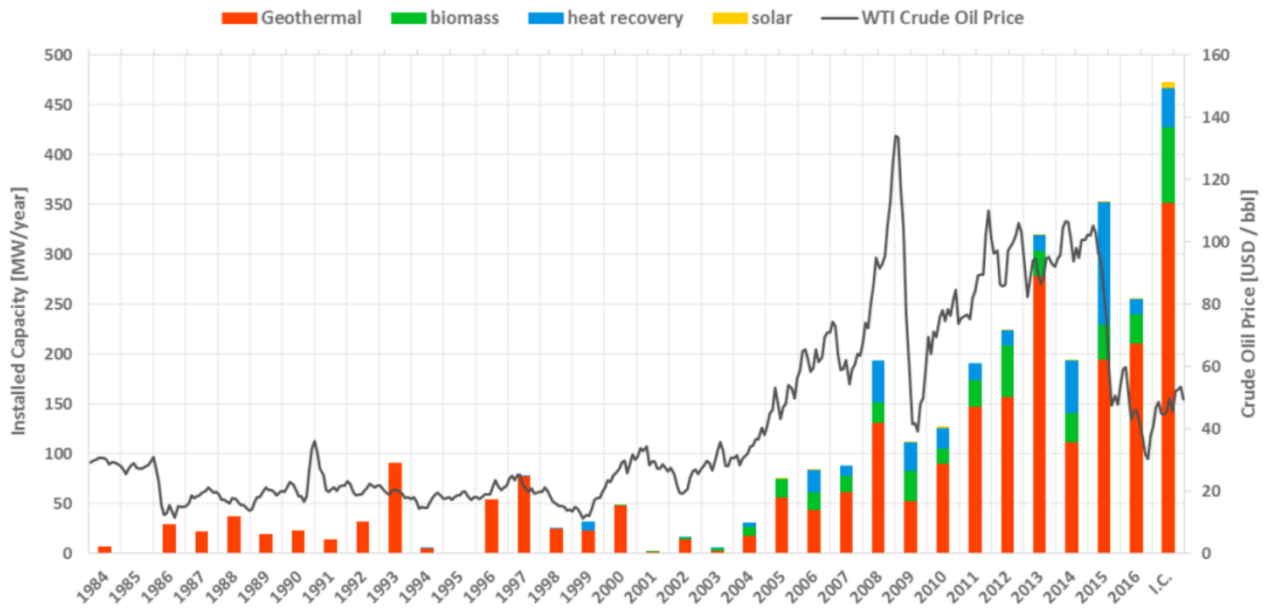


Fig. 2.6: Installed ORC capacity from 1984 up to 2017, with different application highlighted

2.2.2 ORC architectures

ORC technology presents several degrees of optimization in the design process. The main ones can be resumed to 5: operating parameter selection (mainly pressure), working fluid selection, component selection, cycle architecture and control strategy. Differently from steam Rankine cycle, ORC can easily incorporate components such as re-heaters or recuperators, as well as to develop supercritical cycle at relatively low heat sources temperature. These features allow a possible enhancement in cycle efficiency, as well as the feasibility of cost-effective solutions. The simplest structure of an ORC is often called basic ORC and is composed of 4 main components: two heat exchangers (an evaporator and a condenser), a pump and an expander. In order to increase the thermal efficiency of the simple basic cycle, various modifications have been proposed, from the simplest with a recuperator, to multi pressure configuration, flash and ejector layout. All of these cycles are explained in Fig. 2.7. The ORC with recuperator enhances thermal efficiency though the utilization of a recuperative heat exchanger at turbine exit. The exhaust gases at the turbine pre heat the fluid at evaporator inlet, allowing thus a reduction of the heat input to the ORC, while maintaining the same level of power output [21]. The multi pressure level configuration has been introduced in order to decrease the irreversibility in the heat transfer process at the evaporator. The match between the higher-pressure level and the heat source is improved and this allows an increase in thermal efficiency. It is to be remarked that an accurate optimization of the two-pressure level is fundamental in order to obtain the lowest level of irreversibility. The drawback of this configuration, which enables the global thermal efficiency of the power plant, is the increase in the complexity of the layout, and consequently of power plant costs [22], [23]. The ORC flash cycle is used when zeotropic mixtures are employed as working fluid. The advantage of zeotropic mixtures is that evaporation does not occur at fixed temperature, allowing hence a better heat transfer process. Nonetheless, as for the multi-pressure solution, even if there is an increase in thermal efficiency, there is also an increase in power plant complexity and costs [24]. Ejector type ORCs have been investigated with the aim of increasing the expansion ratio of the turbine, allowing therefore a higher power production. The simplest configuration is obtained introducing an ejector at turbine exhaust and a second stage evaporator. The second stage evaporator allows the vaporization of the primary fluid of the ejector, which consents the reduction of the pressure of the turbine discharge stream [25]. Other ejector ORC configurations have been assessed; introducing the ejector in parallel to the turbine, using a bleed of the turbine as the hot primary stream, or

utilizing the hot stream at turbine exit as the primary flow of the ejector in order to develop a combined ORC–refrigeration cycle. The disadvantages of the ejector ORC configuration are the presently low ejector efficiencies and the increase of complexity of the cycle when compared to simple and recuperative arrangements [26], [27], [28]. Not only ORC layout can be listed as possible architecture modification, but also advanced thermodynamic cycles need to be taken into account. Indeed, several solutions, which utilize basically the same components configuration, can take place, such as trilateral cycles, super critical cycles or trans–critical cycles. Trilateral cycles, or often– called triangular cycle, employ the same components of a basic ORC, with the exception of the expander, which is specially designed to work in two–phase conditions. The main advantage of a triangular cycle would be the possibility of optimal matching of evaporator temperature profiles. Nonetheless, actually, there are not efficient expanders which work in two–phase region [29]. Both trans–critical (TC) and super–critical (SC) cycles bypass the two–phase region when heated, allowing a good thermal match between working fluid and heat source. The difference between TC and SC cycles is that in the former one, condensation still takes place in the two–phase region. These two cycles configurations allow an increase in power production; however, the thermal efficiency is usually comparable or even a bit lower than other cycle configurations, due to the increase of heat demand [30]. Finally, Tab 2.3 resumes the possible cycle architecture, as well as the challenges related to each configuration. It seems clear that, as it often occurs in engineering design, there is not an optimal solution, but each configuration has advantages and disadvantages which should be carefully weighted and assessed depending on the specific application.

Cycle	Modifications	Challenges
Recuperative	Extra heat exchanger	Only beneficial if lower cooling limit of flue gasses
Flash	Added Separator, throttling valve, mixer, extra heat exchanger	Performance comparable to basic ORC; many extra components
Multi pressure	Multiple pumps and heat exchangers	Many extra components needed
Trilateral	Two phase expander	Availability of high efficiency two– phase expanders
Trans/Super critical	Super critical fluids	High pressure; working fluid
Ejector	Added evaporator, ejector	Ejector efficiency

Tab 2.3: Possible ORC architecture

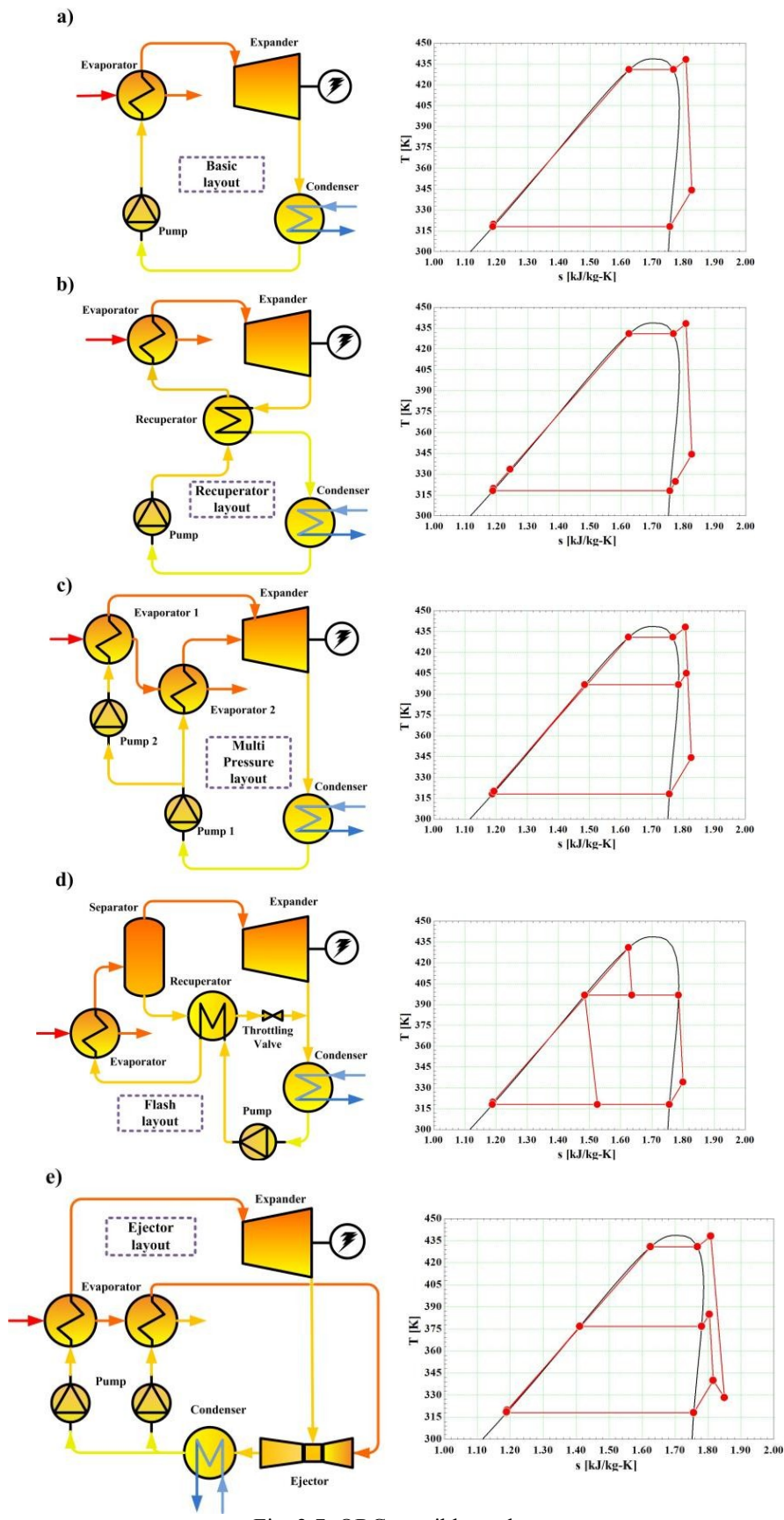


Fig. 2.7: ORC possible cycles

2.2.3 Working fluid selection

As previously stated, the thermodynamic cycle of an organic Rankine cycle exploits the same concept of a steam Rankine cycle, nonetheless, the utilization of organic fluids adds a further degree of freedom for the system design. Indeed, lifting the limitation of water or air as working fluids, it is possible to select the most appropriate fluid, which guarantees the optimal compromise between thermodynamic efficiency and technical system configuration, as well as plant costs. An example of the increased flexibility given by the fluid selection is given by the possibility of exploiting supercritical cycle configuration at low temperature of the heat source. Furthermore, there is an increased level of versatility in the selection of pressure and density levels within the system, which are almost independent from the upper cycle temperature. Organic fluids have a lower boiling point than water and higher molecular complexity, which are properties that make ORCs suitable for small–medium size power plants (1– 5000 kW) and for heat recovery applications. Nevertheless, organic fluids need to comply with many constraints, which may be very tight depending of the field of operation. Indeed, optimal organic fluids should be [31]:

- Non-toxic, inflammable, non-corrosive, cost-effective;
- Detain low (or better zero) global warming potential (GWP) and ozone depletion potential (ODP);
- Thermally stable and compatible to sealing material;
- Good lubricant;
- Proper heat transfer properties;

The possibility to choose the most suitable working fluid depending on the application guarantees (compared to gas cycle and steam Rankine cycles) :

- increased component efficiencies
- usually no vacuum condenser
- higher cycle performance

These favorable features gave rise to numerous research studies on the assessment of the optimal working fluid selection [31], [32], [33], [34]. Organic working fluids can be categorized not only by their molecular structure, but also by the slope of the saturation vapor curve (right side), which is a pivotal feature of these working fluids. There are three types of working fluid: a wet working fluid is called one, which possess a negative slope vapor saturation curve ($\frac{ds}{dT} < 0$); a dry working fluid conversely, is one which is characterized by a positive slope vapor saturation curve ($\frac{ds}{dT} > 0$); finally, an isentropic working fluid is the one which has an almost infinite slope. Fig. 2.10 displays some of the most common organic working fluids saturation curves. Particularly, it is possible to distinguish wet fluid (such as Water, Ammonia or R134a), from dry fluids (such as n-pentane, n-hexane or MM) and isentropic fluids (such as R245fa or R1233zd(E)). From the analysis of Fig. 2.8 it is possible to easily understand the advantage of dry and isentropic fluids. Particularly, wet fluids require super heating in order to avoid wet expansion, conversely to isentropic and dry fluids, which can therefore be optimized through the utilization of a saturated cycle configuration.

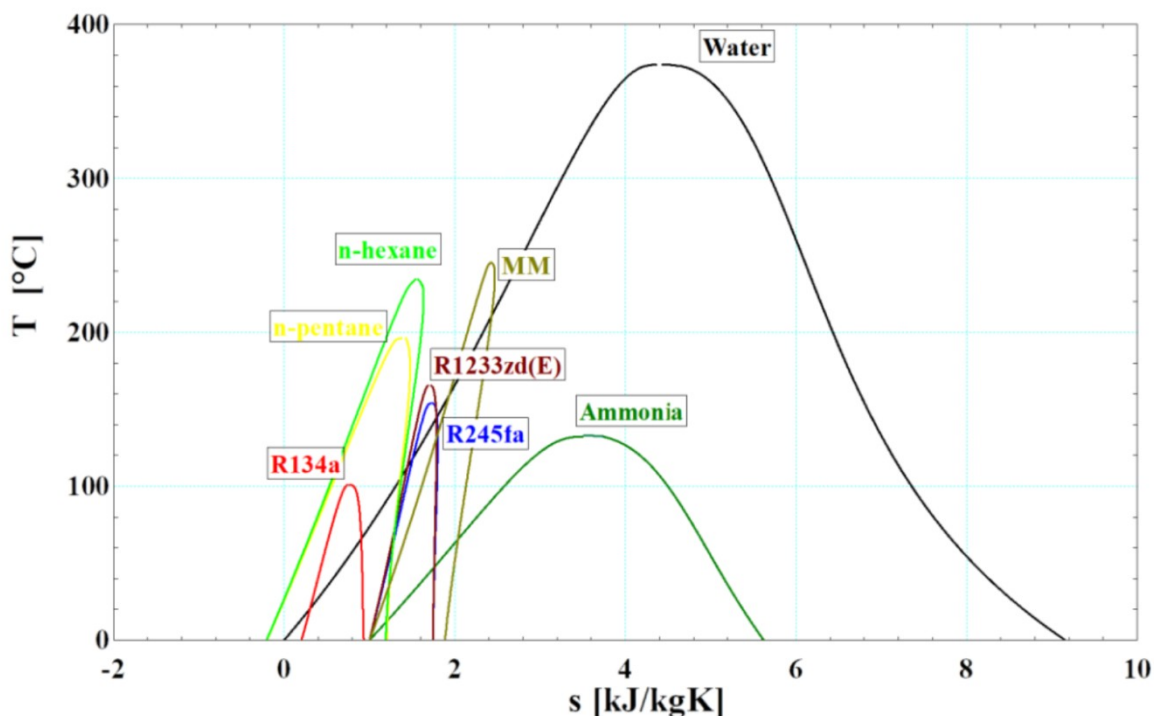


Fig. 2.8 Saturation curves of some common organic working fluid compared to water

The slope of the saturation curve is not the only thermodynamic parameter to be taken into account when selecting the optimal working fluid for an ORC. Tab 2.4 resumes the principal thermodynamic and physical properties, which need to be considered, while designing an organic Rankine cycle power plant for a specific application. Another important aspect that needs to be taken into account when selecting the working fluid for a specific application is that it has to be easily obtainable and have reasonable cost. Good availability and low cost fluids are those already used in refrigeration and chemical industries. Keeping in mind that the assessment of the proper working fluid for a specific application needs to be considered in the design process of an ORC, an interesting classification of optimal working fluids to be used as function of the heat resource temperature level has been carried out in [35], and reported in Fig. 2.9.

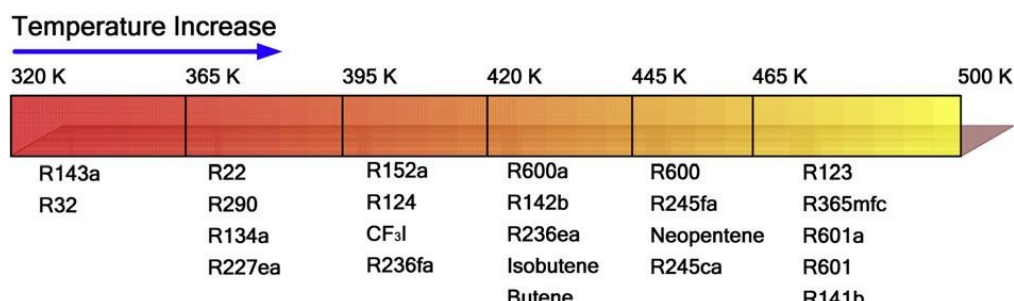


Fig. 2.9 Optimal working fluids as function of heat source temperature

Property	Effect
Vaporization latent heat	At fixed conditions, at a higher latent heat corresponds a higher specific work output; conversely, a lower latent heat allows a better thermal match between working fluid and heat source, as most of the vaporization process occurs at variable temperature.
Density	High vapour density is fundamental if compact, cost effective expander has to be designed. Low vapour density means higher volume flow rate and therefore higher expander dimensions.
Specific heat	Low liquid specific heat allows lower specific work required by the pump.
Critical temperature	High critical temperature allows higher thermal efficiency. The negative side is low pressure at condenser. Furthermore, reduced density, related to working at densities much lower than the critical one, leads to higher expander dimensions.
Boiling Temperature	High boiling temperature leads to higher thermal efficiency, if fluids of the same “family” are compared.
Molecular Mass	High molecular mass allows higher power production at reduced rotational speed, which leads also to a positive effect on turbine efficiency; nonetheless, high molecular mass necessitate of high heat transfer area.
Molecular complexity	Molecular complexity is directly linked to the slope of the vapour saturation curve. Low molecular complexity is linked to wet fluids, while higher molecular complexity is characteristic of dry fluids; high molecular complexity allows higher efficiency at reduced turbine size, moreover it favours the efficiency of the regenerative cycle configuration.
Viscosity	Low viscosity in both liquid and vapour phases allows high heat transfer coefficients and low friction losses in pipes
Thermal conductivity	High thermal conductivity allows better heat transfer
Evaporating pressure	Higher evaporating pressure leads to higher costs and complexity of the layout of the power plant.
Condensing pressure	Condensing pressure should be higher than atmospheric in order to avoid air infiltration into the system.
High temperature stability	Maximum heat source temperature limited by the chemical stability of the working fluid, which tends to deteriorate at high temperatures
High safety level	Low toxicity and flammability required
Environmentally Green	Low ODP and GWP

Tab 2.4 Principal thermodynamic and physical properties of an organic fluid

2.2.4 Expander assessment

The utilization of an ORC is a sound solution when the system is composed by efficient, reliable and low-cost components. A critical component for ORCs is the expander, as it often does not combine low cost and reliability. As the ORC power and hot temperature resources vary strongly depending on the application, the variety of expanders, which can be considered, is also wide. Turbines (axial or radial) as well as volumetric expanders (scroll, screw, vane or piston) are employed depending on hot source and power range. Axial turbines are often used for plants with power production between 500 kW and few MWs [36], while radial turbines are better suited for the lower power ranges (50–500 kW), due to their low degree of reaction and therefore their capability of dealing with large enthalpy drops at low peripheral speeds, allowing the adoption of a single stage design [37], [38], [39]. Finally, for very small and micro power range applications (500 W to about 50 kW), volumetric expanders, like scrolls, screws, vane or piston, are usually utilized, although their efficiency is limited by leakages, friction and heat transfer losses [40], [41], [42]. Several studies have been performed on the assessment of expander selection, depending both on power and volumetric expansion ratio [43] or application [44]. As can be noted both from Fig. 2.10 and Fig. 2.11, at higher power ranges the predominant technology is the axial turbine, while for the small-micro power range volumetric expanders dominate. For intermediate power ranges (20–200 kW) the specific application and boundary conditions are the determining factor for expander selection.

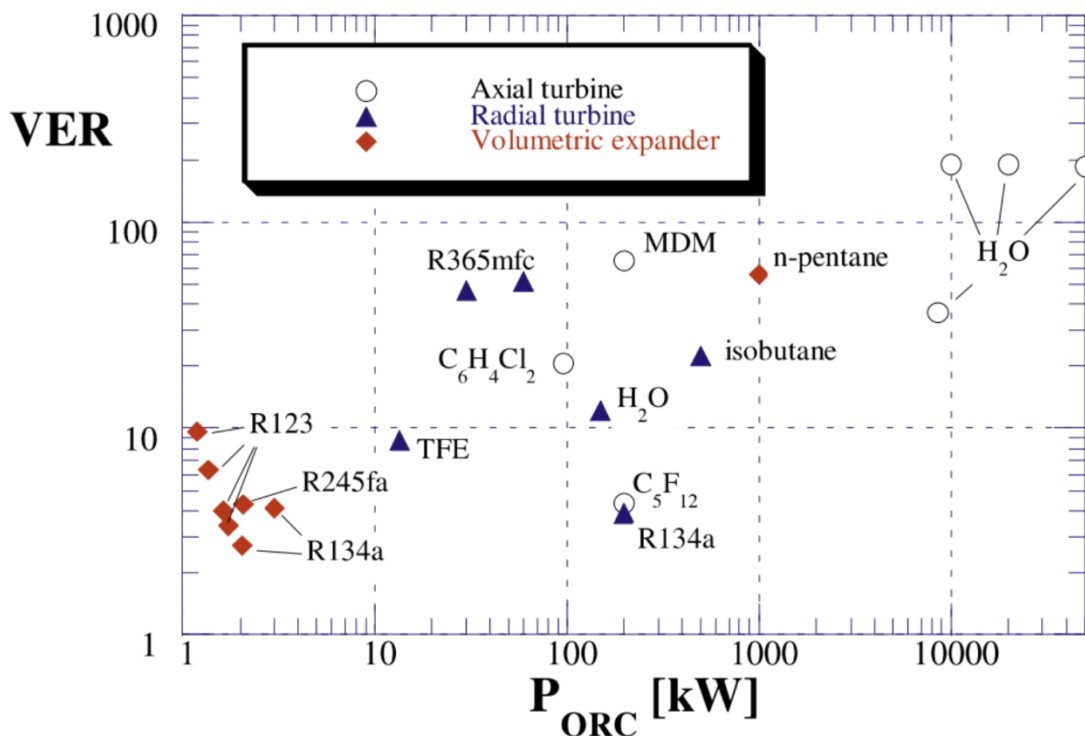


Fig. 2.10 Expander technologies comparison as function of power and volumetric expansion ratio (VER) [43]

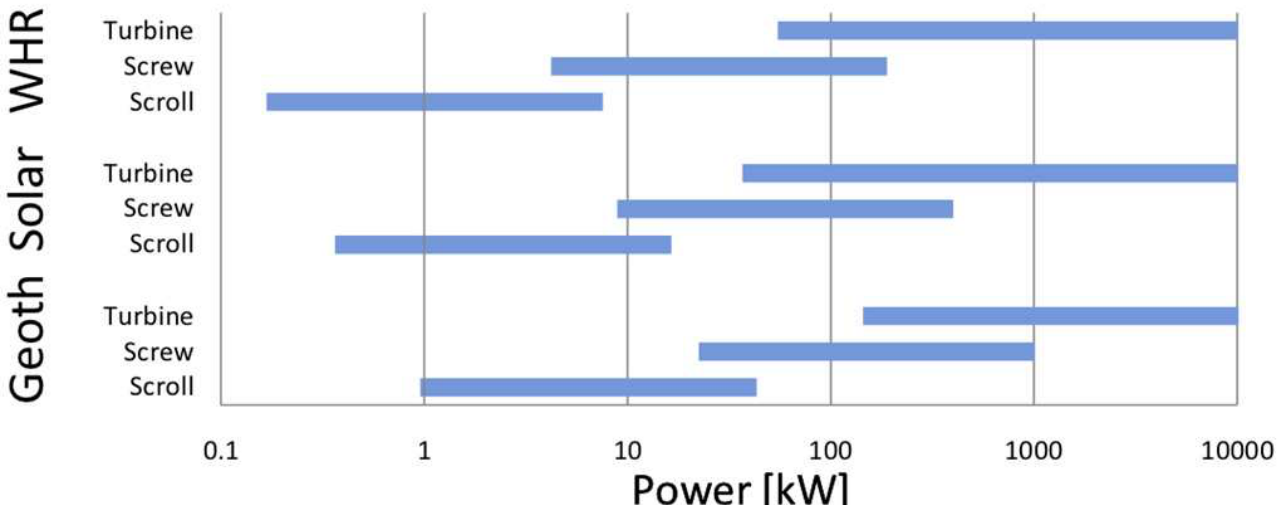


Fig. 2.11 Expander technologies comparison as function of power and application [44]

ORC axial turbines have essentially the same design as steam turbines. Nonetheless, due to the strong difference in thermo physical properties, some peculiar features need to be taken into account: 1. High molar mass implies low sound velocity, which means that when designing the stator, a particular attention has to be taken in order to limit the exit nozzle Mach number to reduce shock losses; 2. Organic fluids realize smaller enthalpy drops than steam, this affects in a different way all kind of turbine losses; 3. High density and small specific volume allow a compact design of the expander; 4. When utilizing organic fluids that are flammable or explosive, special care needs to be taken so that no leakages to air are present. Considering the above-mentioned features, a one-stage axial turbine is often utilized for high mass flow rate systems, while for lower mass flow rates radial turbines are preferred. The main advantages of radial turbines for low mass flow rate applications can be resumed as follows:

1. High efficiency levels even at off-design conditions (obtained by means of variable-geometry inlet guide vanes);
2. The downscaling of radial turbines is favored when compared to axial turbines due to the lower sensitivity to geometric inaccuracies of the blade profile;
3. Radial turbines are simpler to manufacture than axial turbines [32];
4. Higher peripheral speeds than axial turbine are possible, which guarantee a higher enthalpy drop per stage;

Axial and radial turbines are actually not appropriate for micro and small power generation units, mainly due to the very high rotational speed, which dramatically increase when the turbine power output is lowered. Therefore, for low power generation positive displacement expanders are predominant. These technologies will be examined in Section 2.2.5, as they can be considered as “direct competitors” of the Tesla turbine.

2.2.5 Micro expanders

As previously stated for small-micro power generation, volumetric expanders are actually the only alternative. The principle of operation of positive displacement expander is the decrease in pressure through an increase in volume. Commonly, the expander is composed by a stator and one or more rotors directly linked to the expander shaft. While the shaft rotates, the geometry of the rotor defines a series of closed working chambers, where the fluid is enclosed. These chambers increase in volume, reducing thus the pressure of the fluid, which transfers energy through shaft momentum exchange (resulting from the pressure developed on moving surfaces). The major difference

between volumetric expanders lies fundamentally in the mechanism that determines the variation of the volume of the working chambers, as well as the timing of the thermodynamic processes [45]. The principal positive displacement expanders are: reciprocating piston, screw, scroll and vane. These expanders hold different characteristics, which distinguish one from another. The first feature is the type of motion of the rotor. As shown in Fig. 2.12, three main motion categories exist: reciprocating, orbital and rotary [45]. Each expander belongs to one of these classes. Apart from the Roots expander, all other volumetric expanders possess a built-in volume ratio where the working fluid expands. Another difference between the expanders is represented by the presence (reciprocating piston) or not (scroll, screw, vane, roots) of valves. The absence of valves enhances the reliability of the expander.

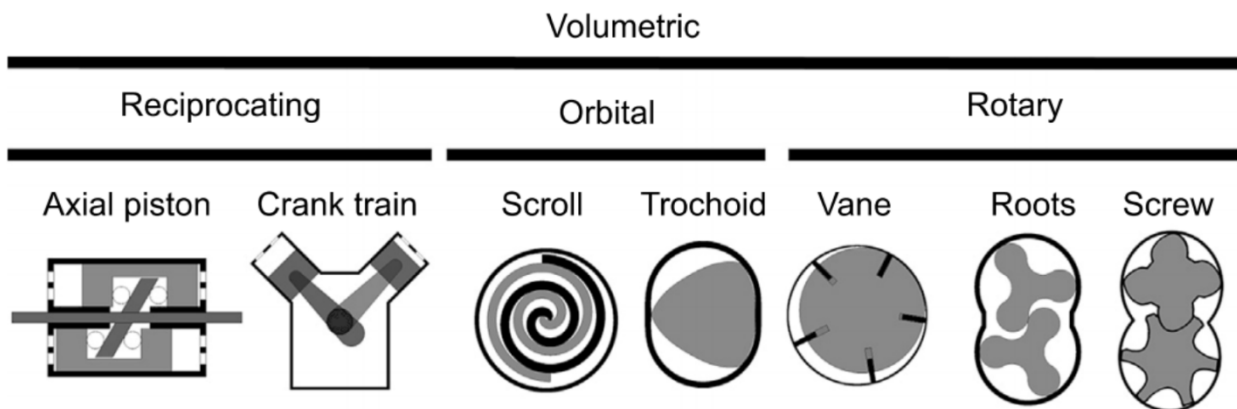


Fig. 2.12 Volumetric expander categories as function of motion type

Scroll expanders are composed by two off-axis spiral-shaped profiles one of them is fixed while the other one is turning, delineating a spiral trajectory. The fluid enters from an opening, which is placed at the centre of the fixed profile, and after expanding through the expansion chambers developed by the rolling of the profile, it exits radially at the discharge chamber. As scroll compressors are very common in refrigeration and air conditioning applications, this expander is often obtained from a compressor just by reversing the direction of rotation and the inlet and outlet of the fluid. Fig. 2.13 displays the fluid expansion process inside the assessed technology.

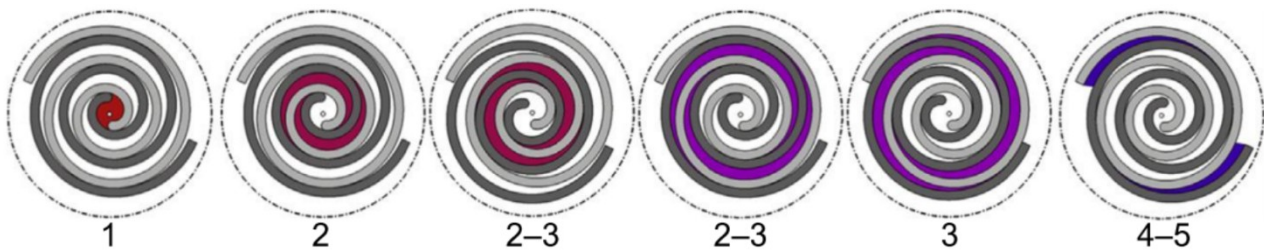


Fig. 2.13 Working fluid evolutions inside a scroll expander

As typical for volumetric expanders, scroll technologies operate on a fixed volumetric ratio, typically between 1.5 and 5 [46][50]. Moreover, the optimal sizing for an expander is indeed different from that of a compressor, so that using an existing compressor just reversing the direction of shaft rotation results in general in a poor efficiency. Two kinds of losses arise if the operating system volume ratio does not match the expander design volume ratio; which are under-expansion and over-expansion [31]. These losses can hinder the efficiency of the expander, limiting the expansion ratio. Other assessed losses involve friction losses, supply pressure drop, internal leakages and heat transfer [41], [47]. Scroll expanders can be further categorized in two: compliant and cinematically rigid. Compliant scroll tolerates a further movement in a provided

direction, which let them be adapt for transient operation or for two-phase flow conditions. A very attractive feature of scroll expanders is that they are very reliable as the total number of moving components is quite low. Furthermore, according to [46], scroll expanders can reach quite high efficiency ($>70\%$), at optimal pressure ratio and rotational speed.

Screw expanders can be categorized in two main types, single screw and twin-screw expanders, as shown in Fig. 2.14. Twin-screw expanders are more common in organic Rankine cycle applications, but the research in single screw is increasing in recent years, due to the favourable feature of having a better balance than twin-screw, which allows achieving an augmented bearing lifespan. The fluid enters from one side of the screw and exit on the opposite side, passing through a sequence of supply, expansion and discharge chambers, which are determined by the turning of the screw(s). The rotational speed that can be achieved with screw expanders is quite high, which implies the necessity of the utilization of gearboxes and control speed equipment. Screw expanders can be lubricated or oil-free. Oil-free expanders have the advantage of being mechanically simple machines and therefore allow simple manufacturing process; conversely, they hold a main disadvantage, that is, higher internal leakage losses. Nonetheless, screw expanders present high efficiency values (up to 80%) with a power range between 1 and 200 kW [48]. A further favourable feature of these expanders is their good ability to tolerate two-phase flows. As scroll expanders, also screw expanders can be easily obtained from a reversed compressor, just changing the direction of rotation. The maximum built in volume ratio of screw expander is about 8.

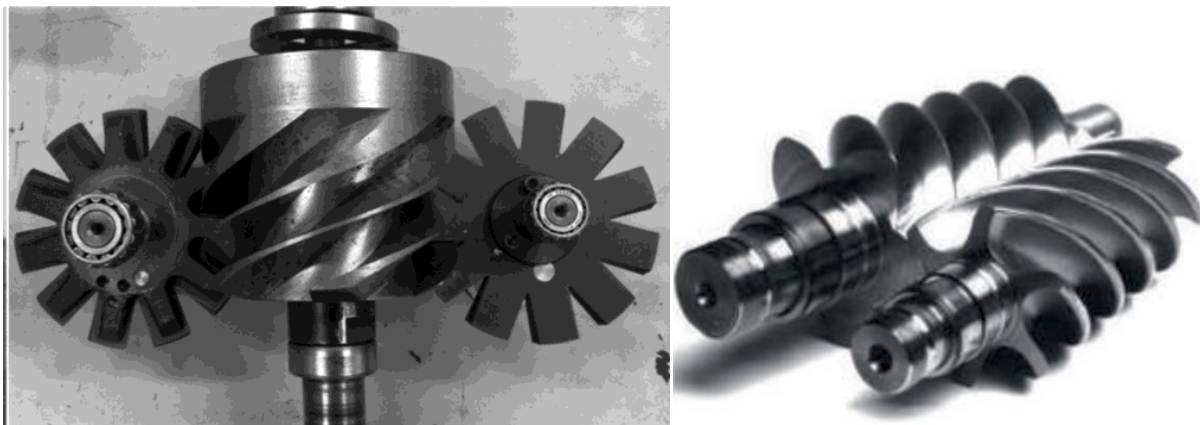


Fig. 2.14 Single and twin screw expander [48], [49]

The Roots expander is similar in principle to a screw expander with a 2D geometry, but it is not as common. Research studies on this kind of expander are quite few. The typical built-in volume ratio is close to one and the power range is typically between 1 and 30 kW. The advantage of this expander is that it can handle easily two-phase flow conditions. Reciprocating piston expanders for organic Rankine cycles are derived from the well-known design concept developed in various areas, such as automotive, energy or petrochemical industries. The most used design of volumetric expander relies on the crank mechanism, but other mechanism can be utilized, such as free pistons [50] or slash-plate [51]. The main advantage of piston expander is that they are suitable for applications where high temperature and high-pressure ratio are required. The built-in volume ratio of a piston expander can be as high as 15. The efficiency value is around 70% and they are suitable for low displacement and low power applications. The piston expander is the only one between volumetric machines for micro generation in organic Rankine Cycle that requires the utilization of valves. This feature increases the complexity of the machine, lowering its reliability. Furthermore, there are also some other drawbacks, such as lubrication issues and high manufacturing costs. The Rotary vane expander is characterized by a rotary motion of a vaned cylindrical rotor within a housing, which acts as stator. The geometry of the expander is appreciably simple, which guarantees low manufacturing costs. The main advantages of the vane expander are the flat

efficiency curve throughout an extended range of operating conditions, the low operating speed, the possibility of accepting two-phase flows and the high expansion ratios achievable (up to 10). Conversely, as most volumetric machine, the vane expander is limited in temperature. Indeed, high inlet expander temperatures are not possible, as they would cause an increase in friction losses in the vanes due to thermal expansion of the rotor, which finally could end up being locked. When going through the selection of an expander for micro organic Rankine cycles, many parameters need to be assessed, such as efficiency, pressure ratio, ability to tolerate two phase conditions, rotational speed, reliability and cost. Which is the fundamental feature for expander selection would be determined by the specific application, but some guidelines can be outlined. Particularly, the comparison between various types of micro expanders for ORC applications is resumed in Tab 2.5. As previously discussed, in the very small power range, radial turbines are not suitable, and actually volumetric type machines are the only alternative. Among volumetric machines, scroll and rotary vane expanders are more suitable for very small-scale applications, whereas screw and reciprocating piston expanders belong to a higher power output range. Therefore, in this context, the Tesla turbine may represent a direct competitor to scroll and rotary vane expanders, as, if properly designed, it holds the same characteristics of moderate rotational speed (if relatively high rotor diameter is utilized), low manufacturing cost and suitability to very different fluids and applications. Furthermore, conversely to most of volumetric expanders, it does not require lubrication, which may be very important in several applications.

Type	Power range [kW]	Rotational speed [rpm]	Cost	Characteristics
Scroll expander	1–10	<10,000	Low	+ High efficiency, low cost – Lubrication requirement
Screw expander	10–200	<10,000	Medium	+Flat efficiency curve at off-design –Difficult to manufacture, lubrication
Reciprocating piston expander	20–100	<12,000	Medium	+Mature technology, high pressure ratio – Heavy weight, complex
Rotary vane expander	1–5	<10,000	Low	+Low cost and low noise –Small power range, lubrication
Radial inflow turbine	50–500	5,000–80,000	High	+Light weight, mature technology –High cost, low efficiency in off-design
Tesla turbine	0.5–10	<10,000	Low	+Low cost, low noise, moderate efficiency, reliable – Few prototype tested (very low TRL)

Tab 2.5 Comparison of micro expanders for ORC applications

2.3 The Tesla turbine

2.3.1 Principle of operation

A competitive technology to the actual available micro-expanders is the Tesla turbine, which is a viscous bladeless turbine. This concept was first developed by Nikola Tesla at the beginning of the 20th century, but it went through a long period of indifference due to the run towards large size centralized power plants. Only recently it found a renewed appeal, as its features make it suitable for utilization in small and micro size systems, like ORC applications, where low cost components become very attractive for the exploitation of residual pressure drop. The first description of the turbine (also called friction or disk turbine) was given in the patent submitted by Tesla [52] (Fig. 2.15). This type of radial expander is characterized by the absence of rotor blades, which are replaced by multiple parallel flat disks; a little gap separates the rotor disks from the related stator parts, which consist of one or more tangential nozzles. The working fluid accelerates, expands through the nozzles and enters, almost tangentially, in the gaps between the disks, where it depicts a spiral centripetal path. The working fluid moves from the inlet to the outlet radius due to the difference in pressure determined by friction and by the exchange of momentum, and exits from openings made on the disks at the inner radius. Tesla turbines seem to have several advantages when compared to conventional expanders for low power generation, as their relatively simple structure allows a straight manufacturing process, as well as low cost, reliability, modularity, and versatility. On the other hand, Tesla turbine presents values of efficiency lower than those of conventional turbines. The most critical aspects are the design of the nozzle and of the jet velocity profile.

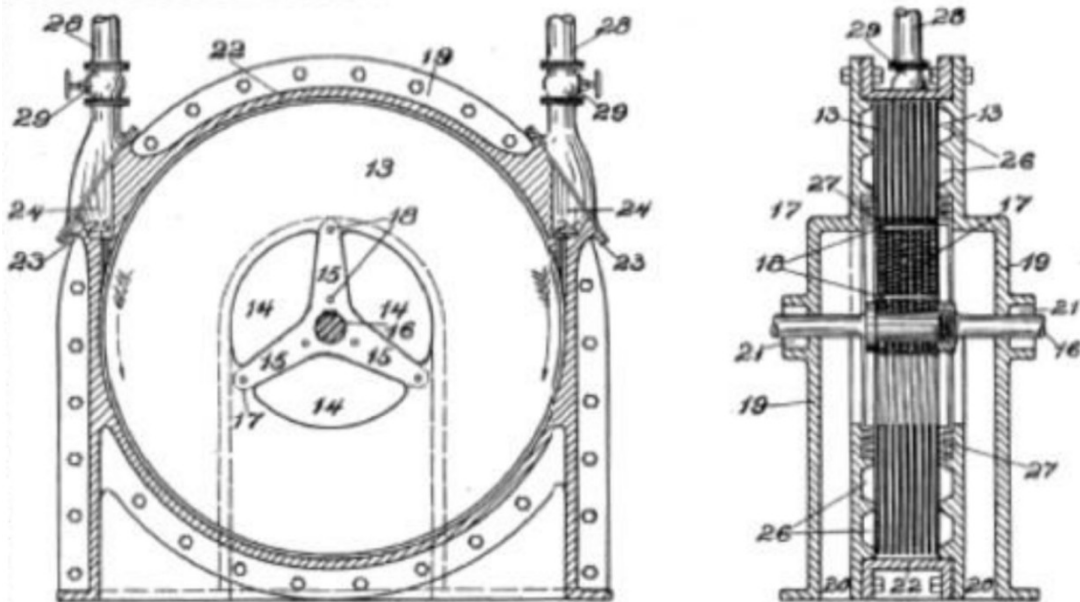


Fig. 2.15 Figs. from Tesla patent, 1913

2.3.2 Typical configurations

As discussed in Section 2.3.1, the first concept of the Tesla turbine was developed by Tesla in 1913 [52]. Conversely, to traditional turbomachines, which exploit the pressure difference that is produced when a fluid flows around a row of blades; the Tesla turbine generates power through the frictional interaction between the evolving fluid and the bladeless rotor. This peculiar rotor, characterized by the absence of blades, is the main feature of the Tesla turbine. Indeed, due to the configuration of the rotor, as well as to the principle of operation, the Tesla turbine is also called bladeless turbine, viscous turbine, boundary layer turbine or friction turbine. Differently from

conventional turbines, the rotor is composed by a series of parallel flat disks with a very small gap between them. The admission of the flow in the rotor occurs through one or more nozzles, which allows the fluid to enter from the external radius of the disks and to exit from the openings made on the disks at the inner radius. Inside the rotor, the fluid depicts a spiral centrifugal path, due to the interaction between the viscous forces and exchange of momentum. Typical configurations of the Tesla turbine consider only the rotor as part of the turbine, and often, nozzles are just converging pipes positioned tangentially to the rotor outer radius, as displayed in Fig. 2.16.

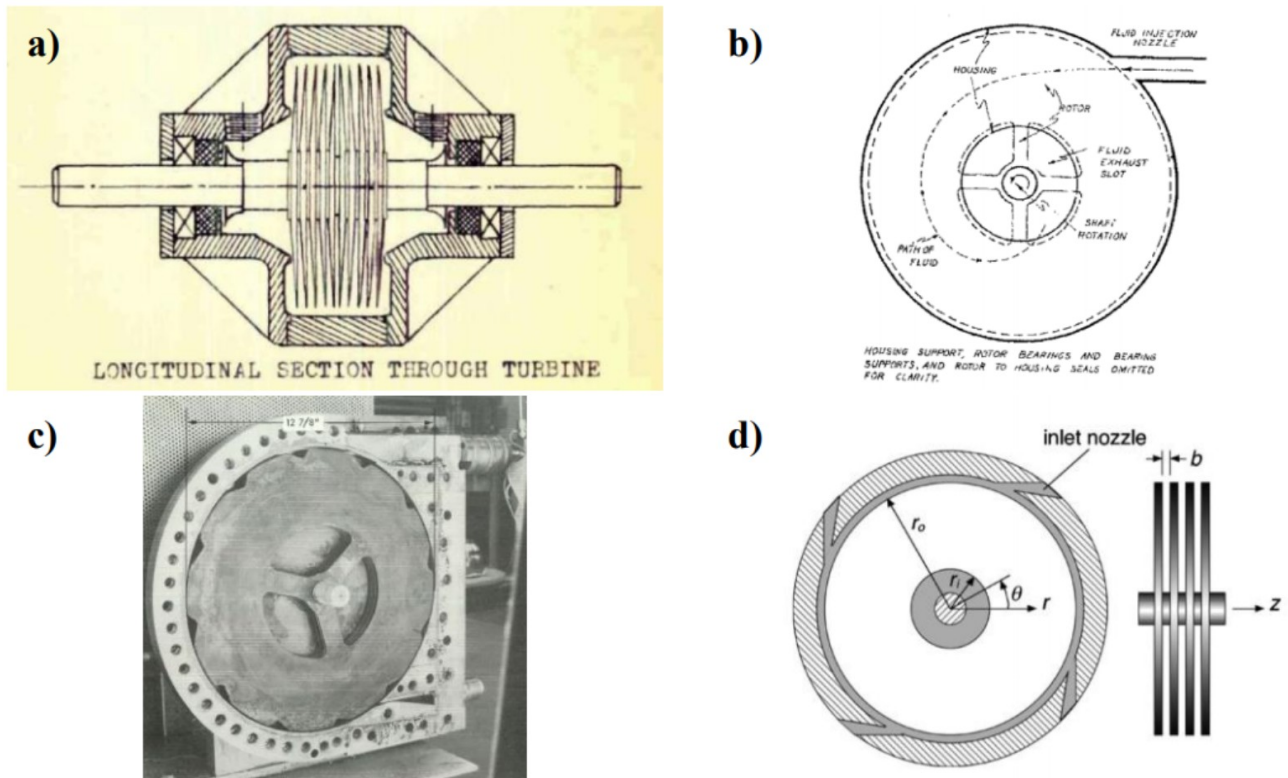


Fig. 2.16 Typical configurations of Tesla turbine

Conversely to the typical configurations, the Tesla turbine described and analyzed in this work consists of several components: an external toroidal plenum chamber, a stator with fixed nozzles and a bladeless rotor composed by parallel thin disks fixed to the rotating shaft; Fig. 2.17 displays the schematic of the ORC prototype.

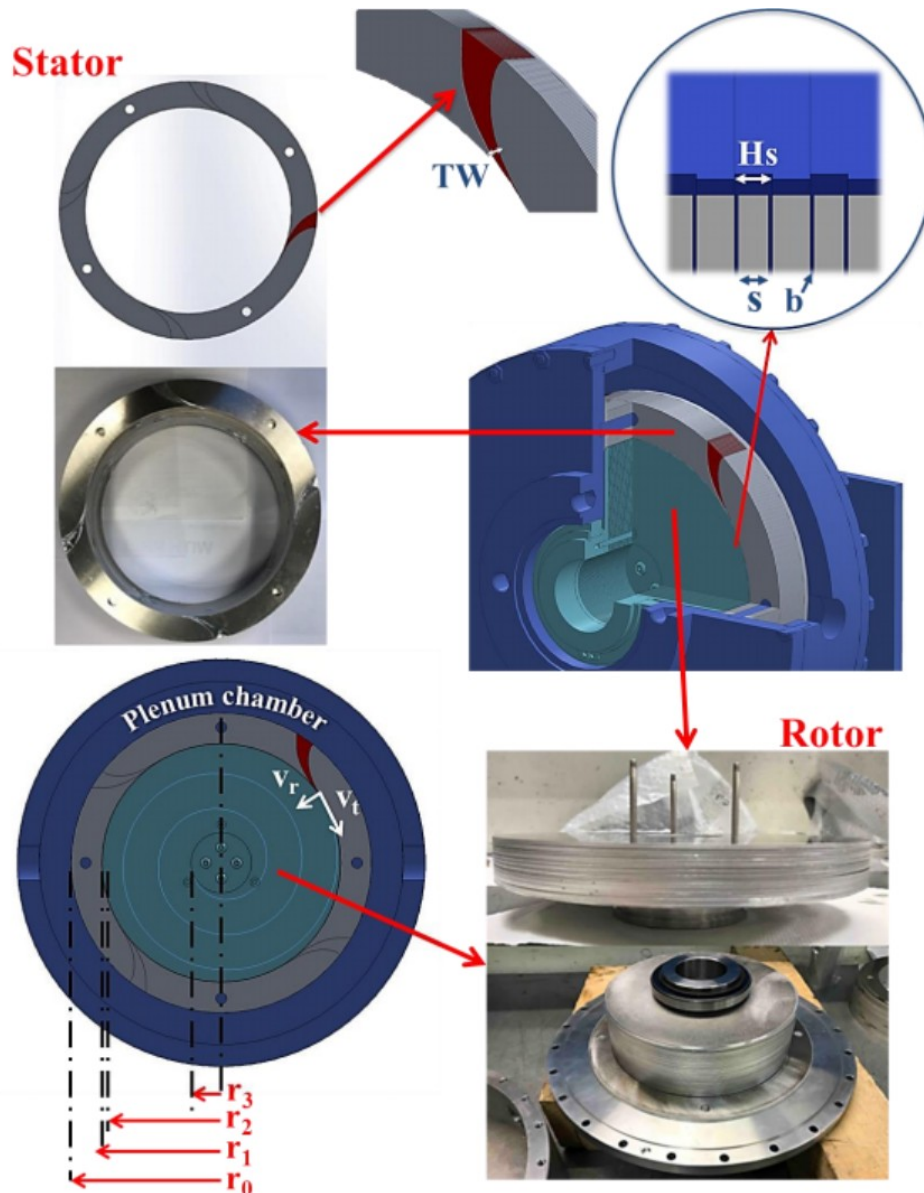


Fig. 2.17 Schematic of Tesla turbine

2.3.3 The ORC prototype

A design and optimization project conducted by Lorenzo Talluri and University of Florence [53] allowed to realize 2 Tesla prototypes: one taking into account air as working fluid and one taking into account ORC. In order to reach the final prototypes geometry, various factors were taken into account. First thermodynamic optimization was carried out, but without forgetting to perform a mechanical analysis of the optimal thermodynamic configuration, choosing therefore the right compromise and also keeping in mind manufacturing process and test benches limitations.

This work is totally focused to ORC so in the following tables they are described the main geometric parameters of ORC prototype. The same prototype is going to be taken into account in

the experimental campaign section. The turbine is made by stator, rotor and also a plenum chamber which is basically the turbine entrance. The turbine entry is made by 2 1-inch pipes in order to obtain a uniform distribution inside the plenum chamber.

Stator external diameter [m]	Stator internal diameter [m]	Chord length [m]	Number of Nozzles
0,272	0,217	0,059	4
Stator inlet angle [°]	Stator outlet angle [°]	Nozzle throat width [m]	Nozzle throat height [m]
0	85	0,001	0,001

Tab 2.6 Stator geometry

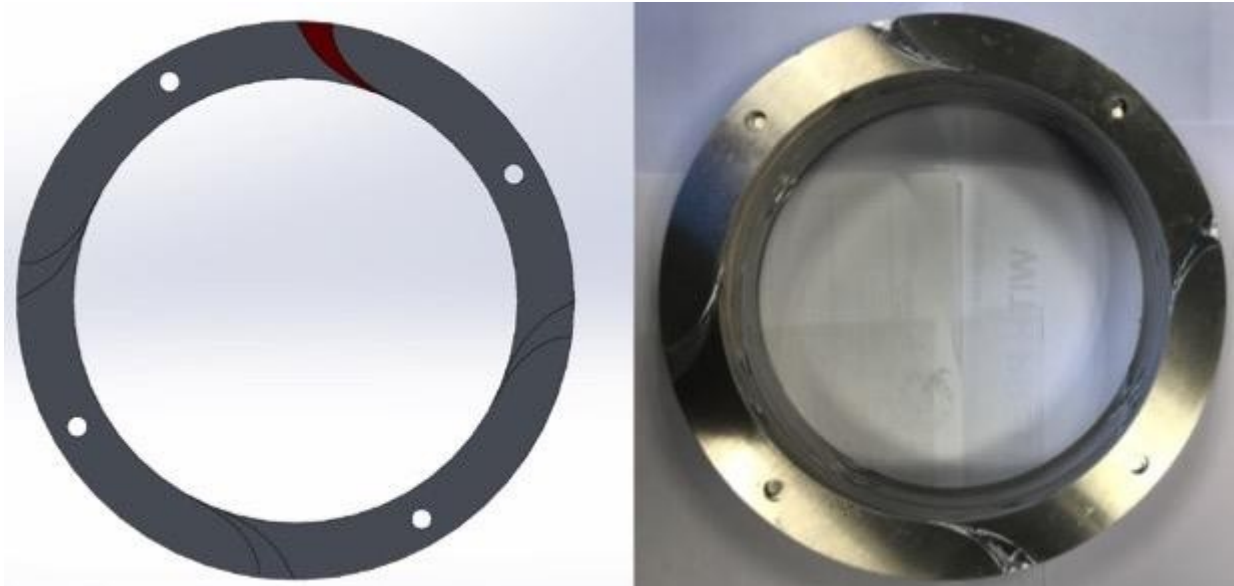


Fig. 2.18 Stator

The number of stator pack are in a way to have 2 rotor channel width for each pack, so they are half of them.

Rotor external diameter [m]	Rotor internal diameter [m]	Channel width [m]	Number of channels
0,216	0,055	0,0001	60

Tab 2.7 Rotor geometry

Rotor external diameter has stator internal diameter as boundary condition, the value of prototype leads to a GAP between stator and rotor of 1 mm which is enough small to reduce Gap loss. The disks which made channels aren't of the same thickness, but they are half of 1 mm and half of 0.8 mm.

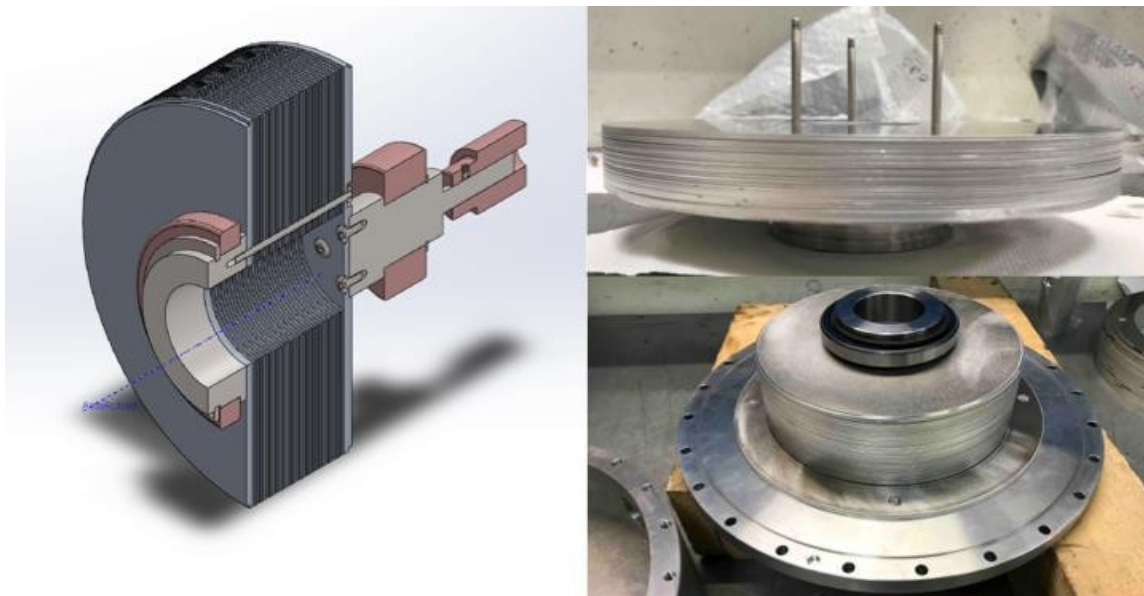


Fig. 2.19 Rotor

The turbine entry is made by 2 1-inch pipes in order to obtain a uniform distribution inside the plenum chamber.

Carter external diameter [m]	Carter internal diameter [m]	Radial minimum thickness [m]	Height of plenum chamber
0,37	0,34	0,02	0,03

Tab 2.8 Carter geometry

In Fig. 2.20 there's the final prototype and in the last image the turbine is on the test bench where it's shown the double entrance which allows to obtain a uniform flow distribution.

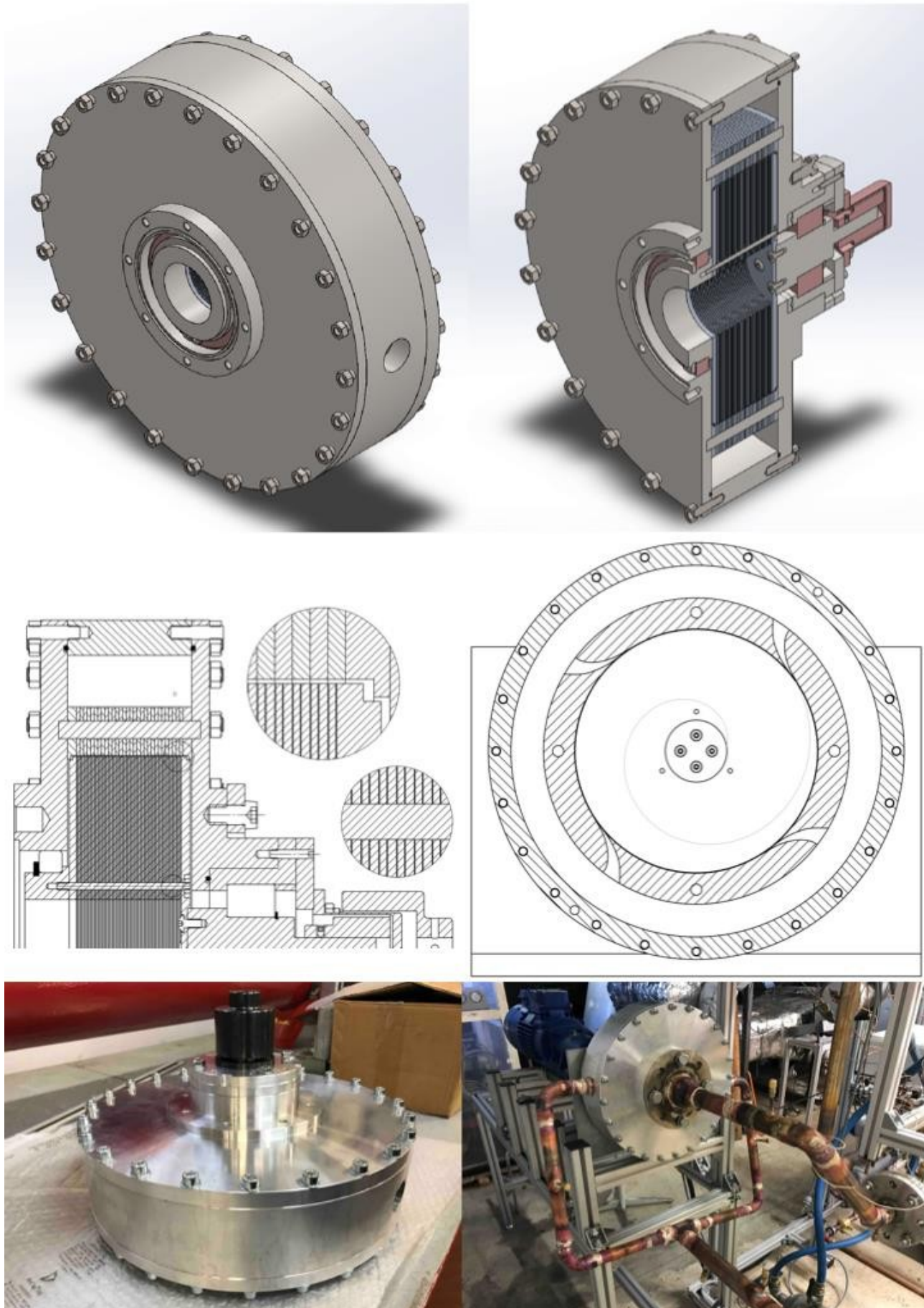


Fig. 2.20 Complete prototype and assembly in the University of Liège's test bench

3 The experimental campaign

ORC prototype was tested at the test bench of Université de Liège in 2018. However, the torque meter used had a huge range (0-100 Nm) compared to the typical torque generated by Tesla. It was decided to repeat this tests with a smaller range torque meter (0-10 Nm) but other issues described in section 3.2 didn't allow to run test. Anyway, in the following sections there's a description about test bench's assessment and reduction of data method. The method to reduce data was performed in University of Liège and it's called "Reconciliation method", its reliability was performed using old data because of the absence of new data.

3.1 Test bench

The schematic of test bench of Université de Liège is displayed in Fig. 3.1. It is basically a recuperative organic Rankine cycle, utilizing R1233zd(E) as working fluid. It was constructed using standard mass-produced components from the HVAC industry, as well as from some specific industrial prototypes, such as the evaporator. The test bench consists of an evaporator, a condenser, a brazed plate recuperator (which however was by-passed during these tests), a pump and a liquid receiver. The pump is a Wanner Hydra-Cell piston pump, which is controlled via a frequency inverter. The maximum volume flow rate and outlet discharge pressure are 30,6 l/min (at 1450 rpm) and 103 bar (at 750 rpm), respectively. The heat source is an industrial heater, which allowed a maximum heat input of about 150 kW.

The thermodynamic conditions upstream and downstream the Tesla turbine were measured by installing T-type thermocouples (copper and constantan wires, very stable measuring range between -200°C and 200°C , with a maximum error of $\pm 0,5\text{ K}$) and piezoresistive pressure transducers (Keller) which have different ranges. The mass flow rate was measured by using a precision Coriolis Krohne Optimass 1400Cr flow meter.

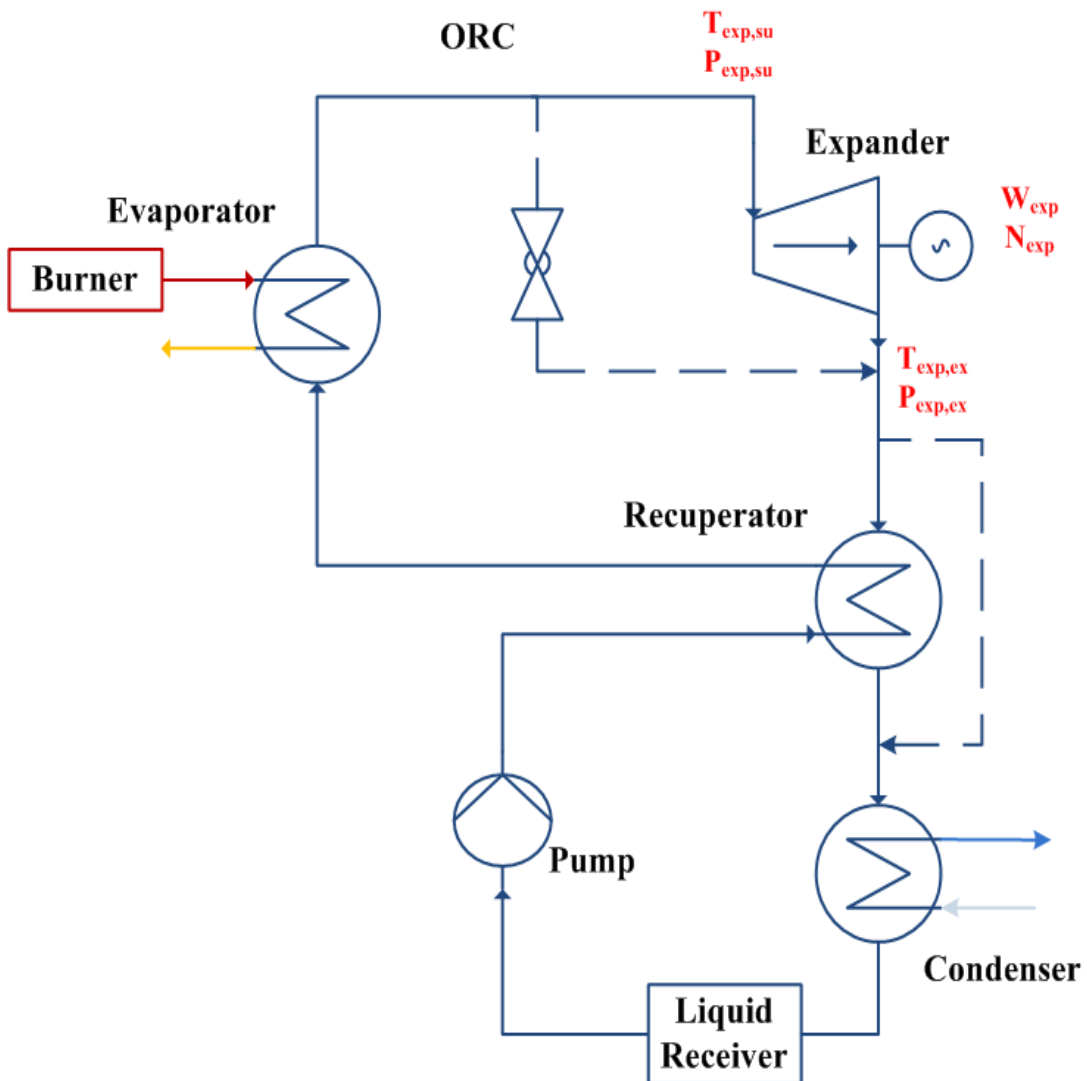


Fig. 3.1 Schematic test bench

The turbine was connected to an electric motor (Perske D 6800 Mannheim 1) that controlled the rotational speed during the tests through a frequency inverter (ABB ACS355). The torque and, consequently, the power produced by the turbine was measured by a torque meter (Messtechnik DRBK, nominal torque 10 Nm, 0,5% FS) connected between the turbine and the motor through flexible couplings.

Misure	Units	Range	% FS
Temperature	K	73-473	0,5
	bar	0-35	0,25
	bar	0-6	0,25
Torq	Nm	0-10	0,2
Flow rate	kg/s	0-1	2 E-3

Tab 3.1 Measurements ranges and accuracy of the sensors

3.2 Turbine maintenance and issues

A maintenance of the turbine was necessary because time spent in a warehouse and probably the high temperatures of its previous tests have badly conditioned some parts of the turbine.

First of all, it was necessary to change every seal because they were completely broken as we can be noted in Fig. 3.2



Fig. 3.2 Turbine's seals after tests

Another problem was the silicone put to facilitate the passage of the flow rate through nozzles. The stator is made by many plates, if there is no silicone the flow rate could pass through the gap between each plate instead of nozzles.



Fig. 3.3 Silicone in the stator

As we can see in Fig. 3.3, most of silicone had come off and this made a gap between plates.

In this case the maintenance followed these steps showed in Fig. 3.4:

- Cleaning the stator taking off silicone
- Compacting stator's plates with screws
- Putting new silicone
- When silicone is dried, removing screws and putting axes



Fig. 3.4 Stator's maintenance

One last critical issue was the screws which connect the rotor to the shaft, highlighted with a red circle in Fig. 3.5.

When Tesla has been opened screws were unscrewed and one of them was completely taken off. So they have been screwed again but when we started to run tests, the torque meter had a huge oscillation. This could be led to a misalignment issue of the mechanic connection between Tesla and shaft.

But when we stop to run tests, the screws were unscrewed again so the misalignment was caused by it.

This issue can advice to use an anti-unscrewing device to support high temperatures and rotational speed

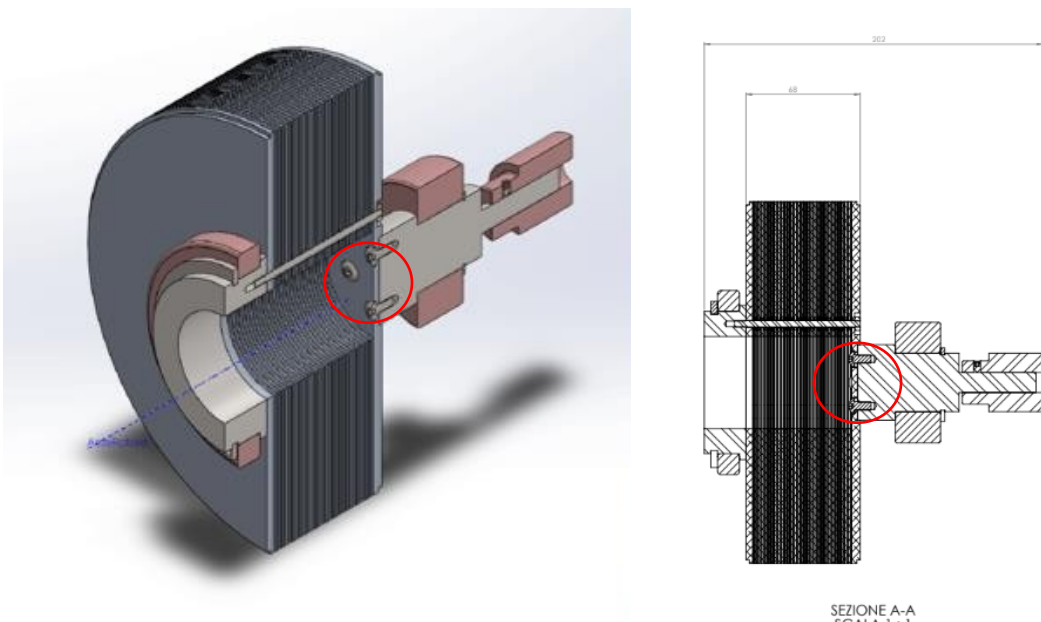


Fig. 3.5 Screws which connected rotor and shaft were unscrewed

3.3 Labview

All signals were acquired by a National Instruments® platform and processed by a software specifically developed in LabView® environment.

LabVIEW(Laboratory Virtual Instrument Engineering Workbench) is a visual programming language: it is a system-design platform and development environment that was aimed at enabling all forms of system to be developed.

LabVIEW uses a graphic interface that enables different elements to be joined together to provide the required flow, it is essentially an environment that enables programming in G, a graphical programming language created by National Instruments.

Within LabVIEW there are several elements and concepts that are key to the format and operation of the environment. These include:

- *LabVIEW environment*: The LabVIEW environment consists of LabVIEW VI manager (project explorer), the programming tools, debugging features, templates and ready built sample examples, and an easy interface to the hardware drivers.
- *LabVIEW VIs*: The LabVIEW VI is a “Virtual Instrument” that enables a user interface to be built and it contains the programming code.

The main elements to make a data logging are “Project explorer” and “Virtual instrument”.

“Project explorer” is the starting point for all applications. It is where all code modules, libraries and data files are stored for easy management and use

“Virtual instrument” provides a visual method of creating the algorithm and it can be used on its own or within a larger overall program, it consists in two main elements

- *VI Front Panel*: is what the user of the completed application will see. It enables them to interact with the VI, inputting controls and also seeing results. It can be likened to the front panel of a test instrument or other piece of equipment
- *VI block diagram*: is where the functionality of the VI is programmed in G. The block diagram defines the functionality while also providing a visual representation of it.

Labview can process signals acquired by a National Instruments platform linked to computer , depending on the measuring instrument, the signal can arrive in different ways:

- AI (voltage analogic input)
- TC (thermocouples)
- TTL (pulse measure/control on/off)
- AO (voltage analogic control/output)
- CI (current input)

For each kind of signal, a different card(called Slot) is connected to the National Instrument platform; for example AI signals have a specific card, thermocouples another type ecc..



Fig. 3.6 Slot for each kind of signal

Putting the right properties and scale for each signal, according data sheets of each sensor, is possible to log measured data in Labview, as we can see in Fig. 3.7 and Fig. 3.8.

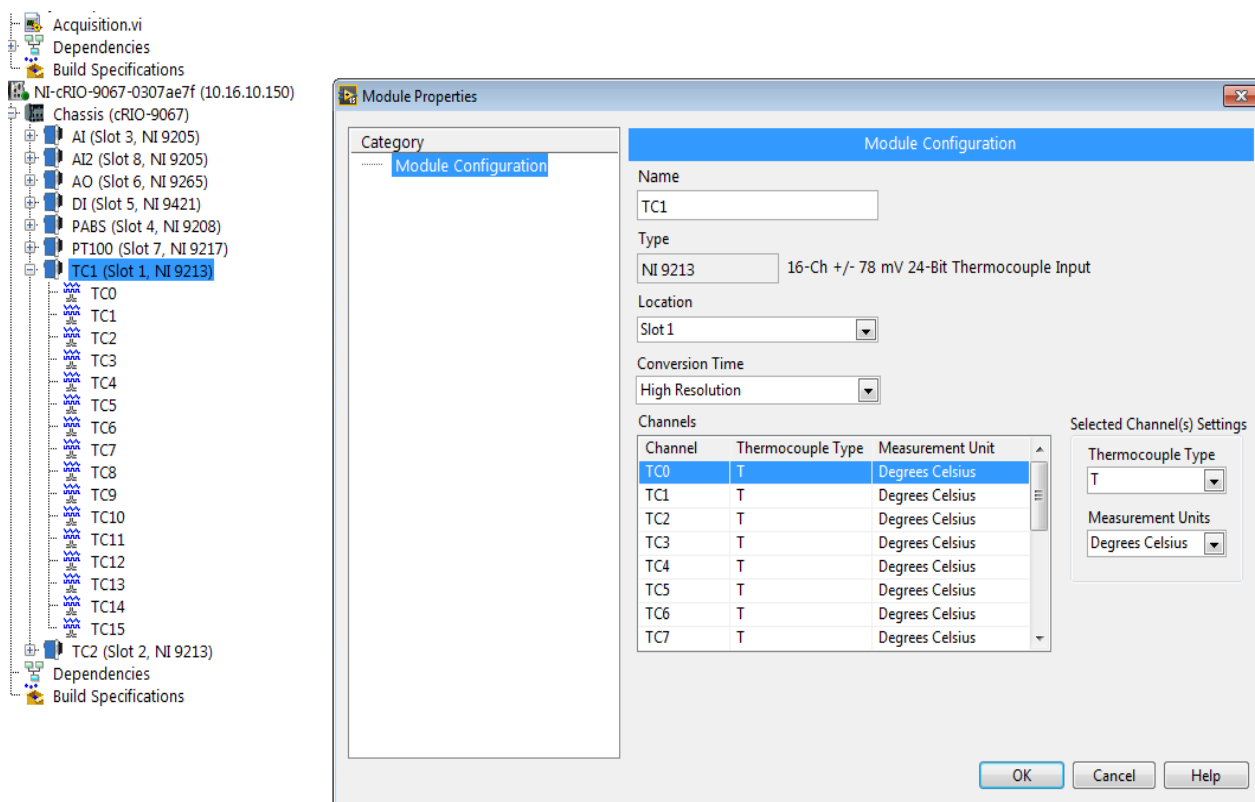


Fig. 3.7 Labview display to set Thermocouples scale

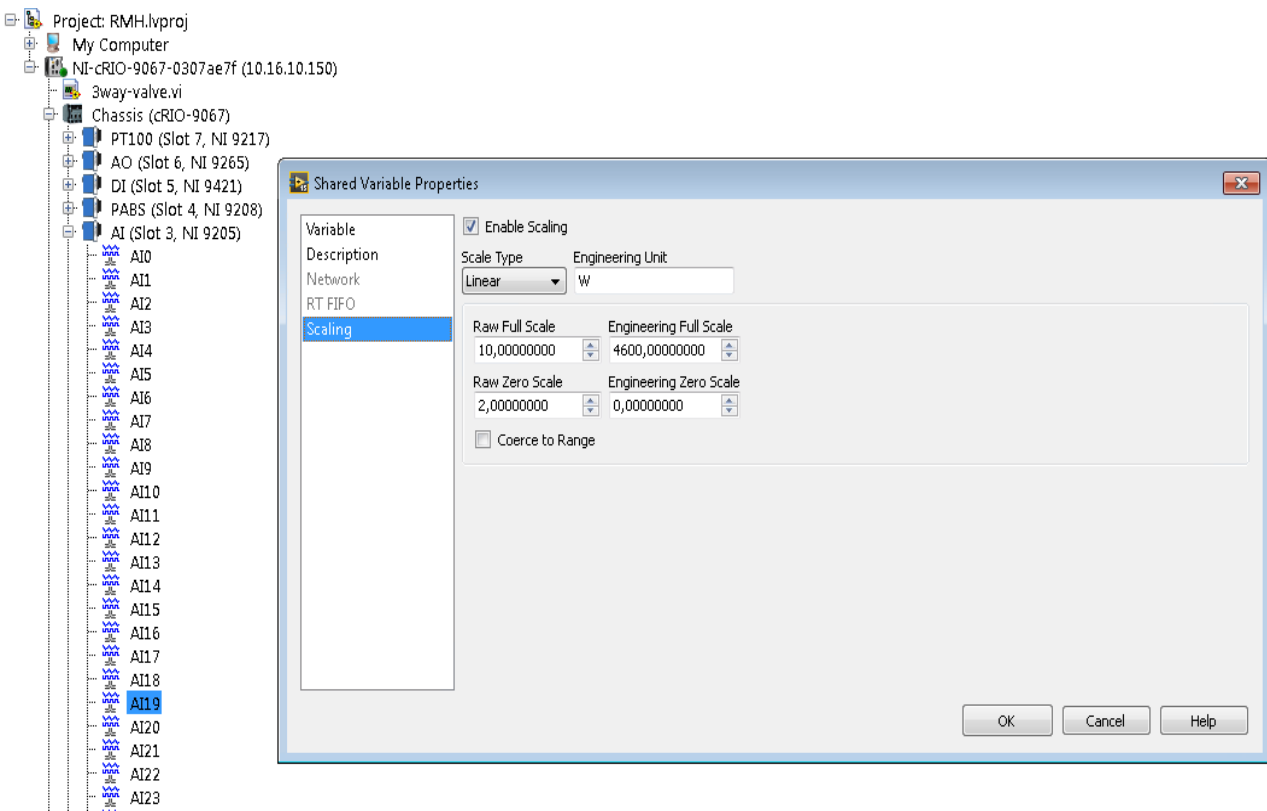


Fig. 3.8 Labview display to set analog inputs scale

3.3.1 Labview code University of Liege

University of Liège made an acquisition project in Labview that is basically the same for each test bench in the Lab, the project used for Tesla test bench is called “Falcon”.

First of all, input signals of the same type are merged in the same array, and each array creates a VI:

- Merge_pressure.vi(voltage input)
- Merge_thermocouples.vi (Fig. 3.9)
- Merge_AnalogInput.vi: this array collects flow rate, torque and other analog input measurements

In the project there are others subVI that are used to find Thermodynamics properties:

- CoolProp.vi: this is the G-version of an open-source database of fluid and humid air properties, formulated based on the most accurate formulations in open literature
- Thermo_prop.vi: made by CollProp too
- Energy balance.vi
- Ts_diagram.vi.

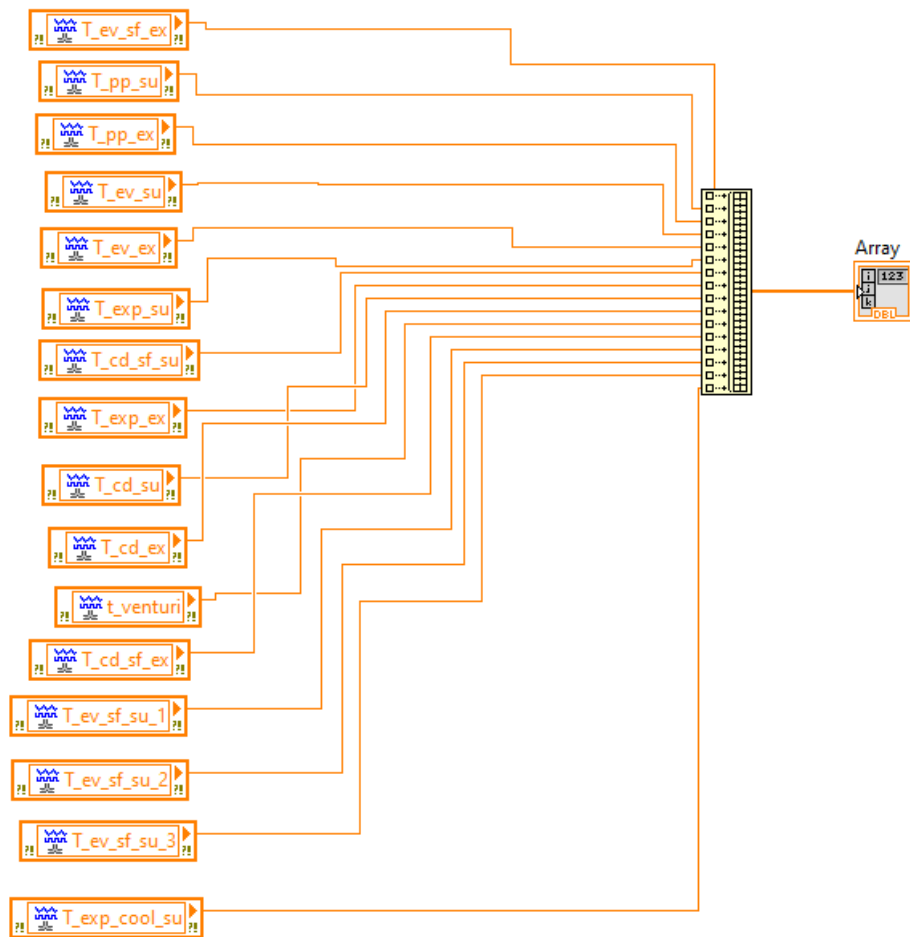


Fig. 3.9 Merge Thermocouples

The main VI are:

- Acquisition.vi has a front panel (Fig. 3.10) which has a block when data are acquired from modules (Merge.vi, ctrl) to make just one array, this array is linked to Display.vi and is used in another block when data are logged in a TDMS file. Each block has clock settings to choose the frequency used reading and logging data. The vector of variables names (pink) writes on the top of the columns where data are logged at each time-step, so it has to match the acquisition array order.

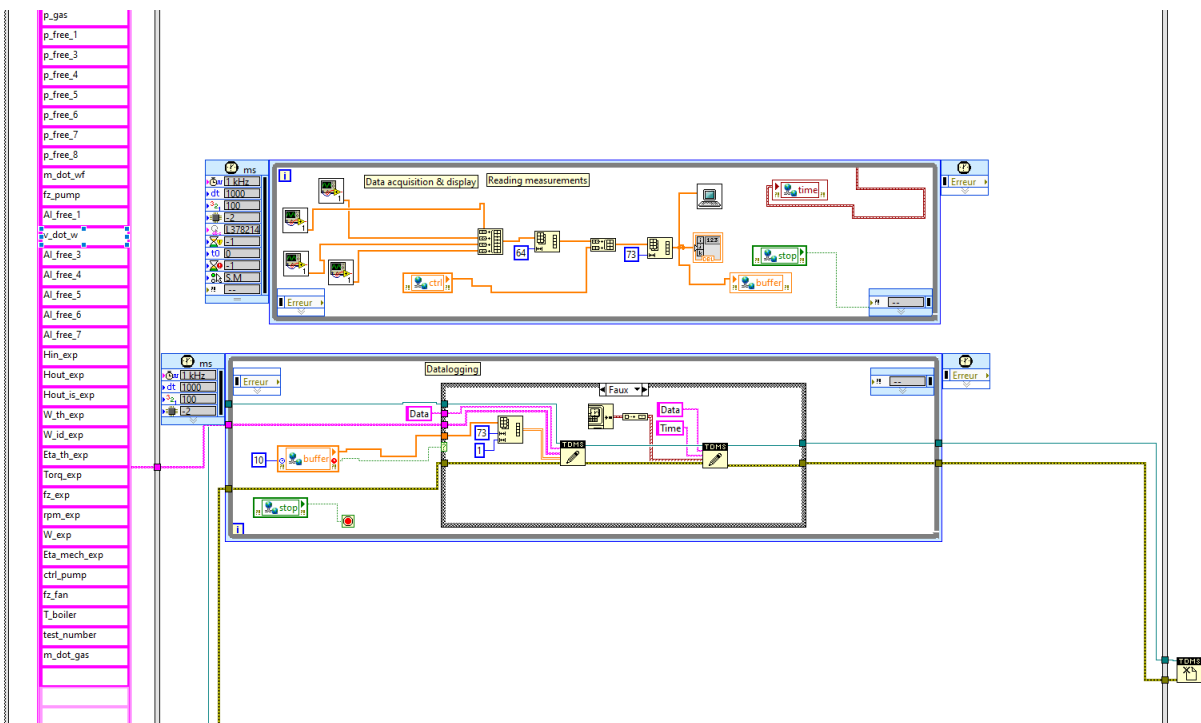


Fig. 3.10 Block diagram of Acquisition.vi

- `Display.vi` is important for its block diagram and its front panel too. In the block diagram (Fig. 3.12) all of the graphs and values checked in the front panel are made. Another important element made in the block diagram is the array called “ctrl”, made by analog outputs and other variables like “test number”, thanks to analog outputs is possible to control turbine’s and pump’s frequency directly from Labview, the array “ctrl” is a part of the Acquisition array as we can see in Fig. 3.10, so it’s logged in TDMS file. In the front panel we can check input values and change the output values of “ctrl” (Fig. 3.11), so each test is conducted checking this panel.

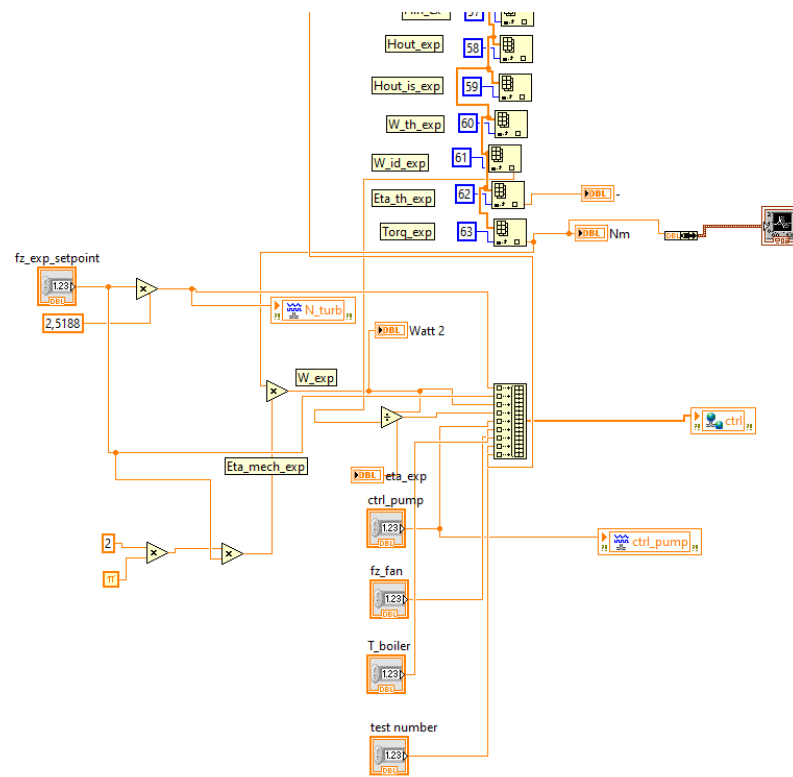


Fig. 3.11 Front panel of Display.vi

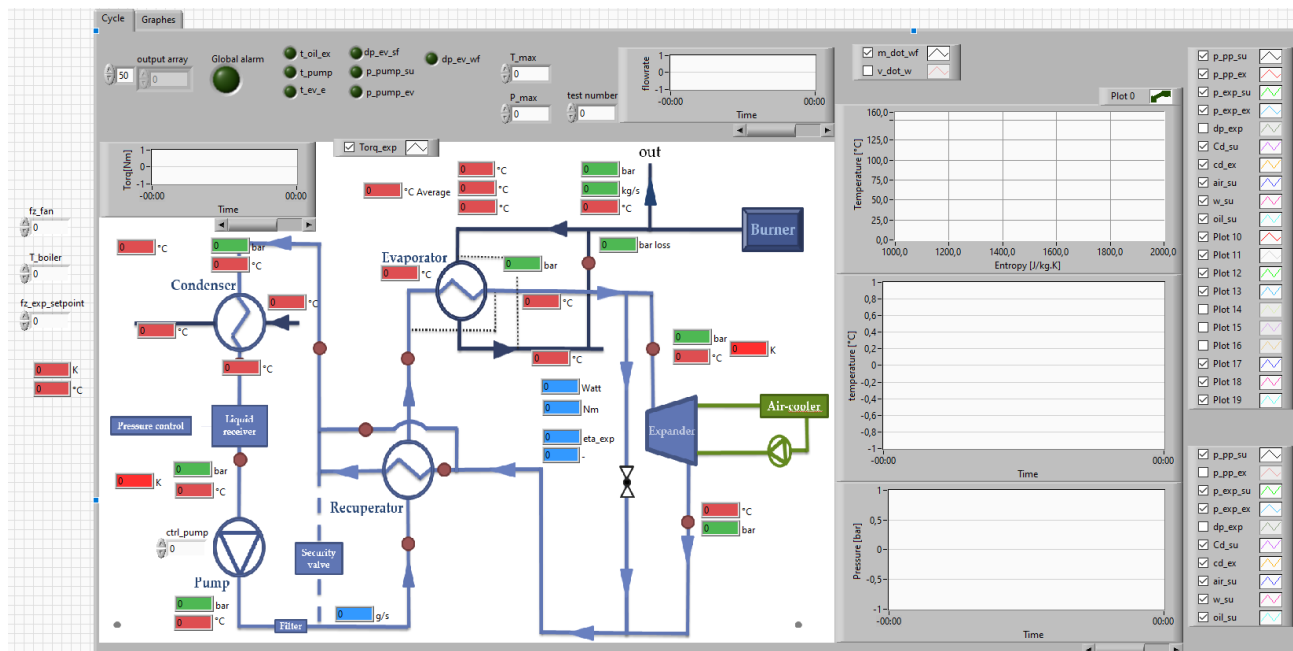


Fig. 3.12 Block diagram of Display.vi

3.3.2 Conduction of tests

The test bench of Université de Liège allowed for the adjustment of:

- The pump mass flow rate (through a frequency inverter), which therefore permitted the imposition of the mass flow rate of the test bench
- The heat input (changing the heater settings of temperature and air mass flow rate), which allowed the regulation of super heating level;
- The heat output (changing condenser water mass flow rate), which provided a control on the lower pressure of the test bench;
- The rotational speed of the turbine (through a frequency inverter), which allowed to change the pressure drop in the turbine.

Tests should have been conducted checking Display.vi, and of course data in steady state conditions logged in TDMS file must be easily recognized. For this reason, the variable “test number” is very important: it’s set equal to zero while the display’s graphs don’t show steady state conditions; when they show them, we change the value of “test number” (1 if it’s the first test, 2 if it’s the second ecc.). So when we want to change a test bench boundary condition is very important to firstly set “test number” equal to zero.

3.4 Global methodology to handle experimental data

3.4.1 Introduction

Measurements are always affected by random errors plus gross errors (error that cannot be explained with statistical distribution). Gross errors are outliers (process leaks and malfunction) or bias (systematical offset). These errors can lead to wrong analysis and understanding of the processes. Furthermore, the quality of the calibration of models is better when the errors are low. The use of reconciled values instead of raw data improves the accuracy of the prediction of the models. This is helpful in the context of this experimental campaign.

3.4.2 Reconciliation Method

This section presents the application of a mathematical tool called the reconciliation method (RM). The latter is recommended to obtain reliable information about the studied process, but gross errors have to be identified and eliminated before the procedure. This technique has been used since 1961 in chemical engineering [54]. In 1980, the reconciliation method was applied to adjust material balancing of mineral processed data - the process of separating commercially valuable minerals from their ores [55]. Later, Weiss and Romagnoli used this tool to better determine regeneration cycle time of a reactor in an industrial case study [56]. Heyen and Kalitventzeff developed a RM optimization to reduce energy use in production plants [57]. Placido and Loureiro studied the placement of new instruments in order to improve the estimation accuracy in ammonia plant units [58]. Schladt and Hu developed a rigorous model to estimate concentrations in a distillation column through the reconciliation method [59]. In 2008, Lid and Skogestad used the RM method to assess the optimal operation of a catalytic naphtha reformer [60]. Despite the proven performance of the method, few authors have used it in refrigeration systems. In 2007, Bruno et al., applied the method to a Hybrid solar/gas Single/Double effect absorption chiller [61]. In 2013, Martinez-Maradiaga et al. used the method for absorption refrigeration system to obtain performance calculations that are

in agreement with the laws of conservation [62]. In 2015, an optimization of redundant measurements location for thermal capacity of power unit steam boiler using data reconciliation method was performed [63]. Finally, a data reconciliation-based framework for integrated sensor and equipment performance monitoring in power plants is provided by [64].

Some authors have predicted unmeasured values (flowrate, oil fraction etc.) simply by minimizing the sum of the residue of each component [65]. A more complete and accurate method taking into account measurements redundancy and accuracy of sensors exists: the reconciliation method corrects each measurement as little as possible, taking its precision into account (assuming a Gaussian distribution around the measured value), in order to satisfy all constraints and to evaluate the most probable physical state conservation [62]. Redundancy is obtained by having two sensors measuring the same variable and/or variable that can be obtained through balance equations (heat balance, residue, mass balance, thermodynamic state of equilibrium etc). This redundancy allows correcting measurements while non-redundant measurements will remain uncorrected. The RM method does not correct data to better fit a model but simply imposes constraints (physical laws) to improve the dataset intrinsic quality.

Reconciliation method should be used for multiple reasons. First, without this method, it is impossible to close energy and mass balances exactly, which is needed for predictive models. Also, it allows determining some unknowns that are not or that cannot be measured precisely (oil fraction, refrigerant mass flow rate etc.). Moreover, it fully exploits the collected measurements with redundancy. Finally, it allows to know which sensor should be checked or replaced if necessary.

Mathematically, the minimization of Eq. (3.1) allows to evaluate corrected (or reconciled) values (u_i) (and eventually additional unknowns) based on the measured values (c_i) and on their standard deviation (σ_i) while satisfying a certain number of constraints.

$$\varphi(u_i) = \sum_{i=1}^n \frac{(u_i - c_i)^2}{\sigma_i^2} \quad (3.1)$$

3.4.3 Methodology

A step by step global methodology can be drawn to handle experimental data efficiently (Fig. 3.13). First, the measurements have to be validated: energy and mass balances have to be satisfied taking into account the propagation of errors due to measurement devices. This step ensures the quality of the data but is also necessary to apply correct physical constraints in the reconciliation method. Following this, the elimination of irrelevant points (outliers) is mandatory to eliminate gross error (which is mandatory for the reconciliation method). The Gaussian process is an efficient tool to perform this task. Finally, the reconciliation method can be applied and validated through the weights and confidence level.

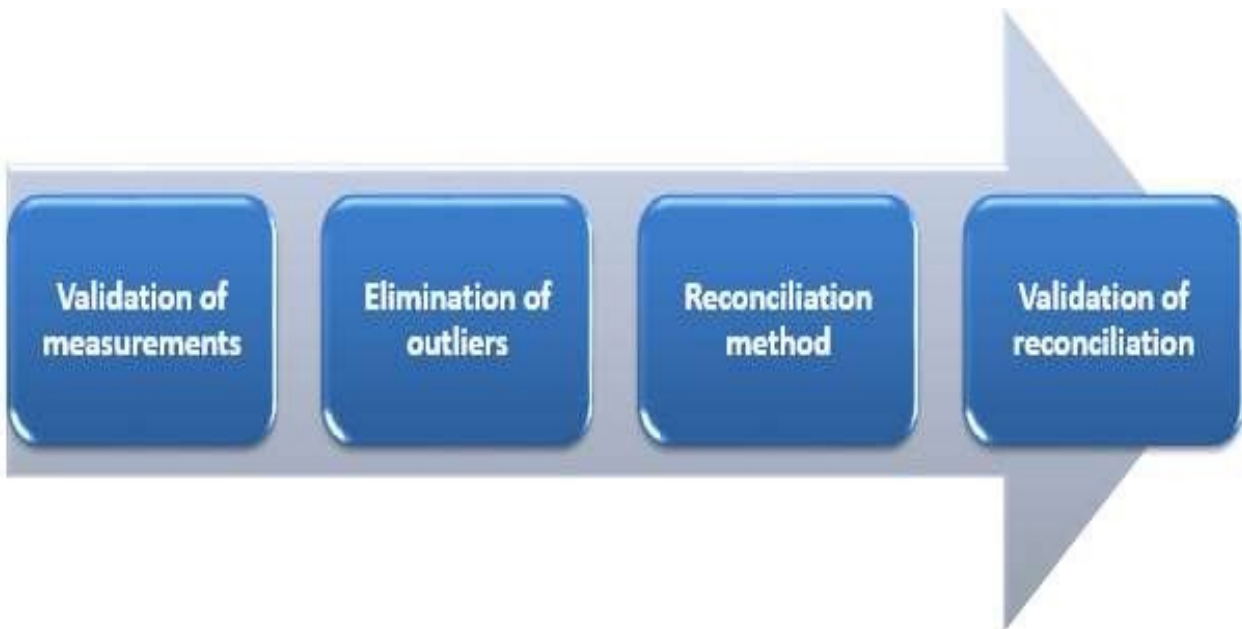


Fig. 3.13 Methology of Reconciliation method

Link Labview-Matlab

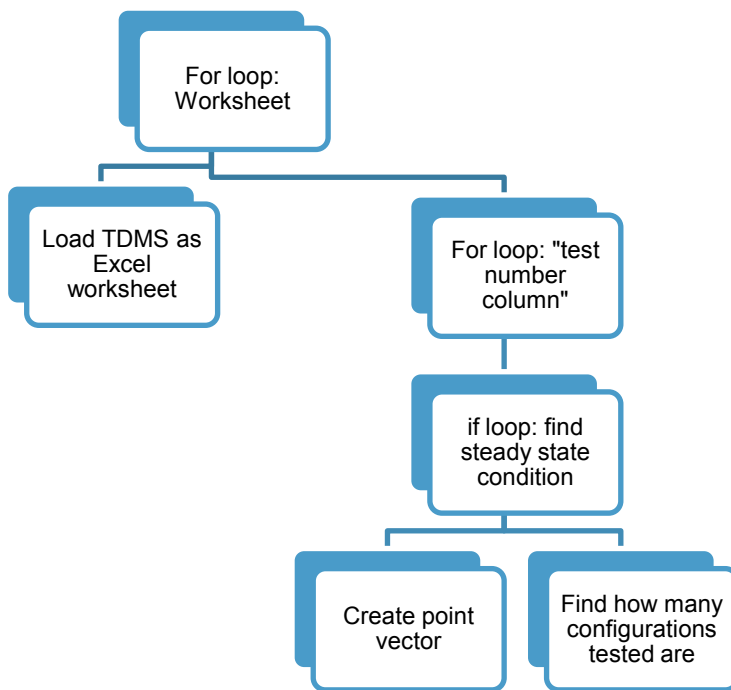


Fig. 3.14 Schematic view of the link to load data from Labview to Matlab

First of all, all of the data loaded into the TDMS file in Labview has to be loaded in Matlab.

The TDMS file can be opened as a .xlsx file, so to load it in Matlab the function xlsread has been used.

Then, the code creates the “point vector” that is made by steady state conditions, the number of configurations tested is the number of the last point vector’s row.

	BD	BE	BF	BG	BH	BI	BJ	BK	BL	BM	BN	BO
1	AI_free_6	AI_free_7	AI_free_8	AI_free_9	AI_free_10	AI_free_11	AI_free_12	AI_free_13	AI_free_14	ctrl_pump	test_number	t_boiler
1856	060602661	-0,23560303	-0,22936367	-0,22870689	-0,24020046	-0,22640818	-0,22345269	-0,22805012	-0,22443785	28,35	52	350
1857	051079418	-0,23987207	-0,23428948	-0,23461787	-0,24611144	-0,23231916	-0,23002044	-0,23461787	-0,23002044	28,35	52	350
1858	060931048	-0,22082559	-0,21819849	-0,22049720	-0,23264754	-0,22016881	-0,22049720	-0,22607979	-0,22345269	28,35	52	350
1859	051736193	-0,23757336	-0,23231916	-0,23231916	-0,24315595	-0,23034883	-0,22837850	-0,23396110	-0,23002044	28,35	52	350
1860	061916212	-0,23954369	-0,23363271	-0,23428948	-0,24348434	-0,22969206	-0,22607979	-0,23100561	-0,22739334	28,35	52	350
1861	044840051	-0,23921530	-0,23363271	-0,23231916	-0,24282756	-0,22805012	-0,22575140	-0,23002044	-0,22607979	28,35	52	350
1862	047795541	-0,23987207	-0,23363271	-0,23396110	-0,24446950	-0,23166238	-0,22870689	-0,23396110	-0,22969206	28,35	52	350
1863	052064581	-0,23691658	-0,23133399	-0,23166238	-0,24184240	-0,22805012	-0,22575140	-0,23034883	-0,22640818	28,35	0	350
1864	047138765	-0,24446950	-0,23757336	-0,23593142	-0,24545466	-0,23133399	-0,22870689	-0,23363271	-0,22870689	28,35	0	350
1865	061259436	-0,23461787	-0,22903528	-0,22870689	-0,23954369	-0,22509463	-0,22246753	-0,22673657	-0,22345269	28,35	0	350

Fig. 3.15 Data logged in TDMS and opened with Excel

As we saw in the section 3.3.2, when there’s a steady state condition the Labview variable “Test number” is different from zero and correspond to the number of configuration tested, so Matlab code has to load this variable when it is different from zero and just one time per configuration. Fig. 3.15 shows an example of TDMS file about 52th configuration tested, the first goal of the code is building the “point vector” just through the column “test_number”; this is made by an “if loop” inside a “for loop”:

```

sheet=4; %% number of Excel worksheets analyzed%%
count=0;
for f=1:sheet
    Matrix=xlsread('Data_TALLURI.xlsx',f);
    Number=Matrix(:,66);
    Y=3000;
    for y=1:length(Number)
        if Number(y)~=Y && Number(y)>0
            Y=Number(y);
            count=count+1;
            Point_vector(count,1)=Y;
        end
    end
    N=count;
    Flow=zeros(N,1); %% Performance indicator
    T_exp_su=zeros(N,1);
    T_exp_ex=zeros(N,1);
    SH=zeros(N,1);

```

```
P_exp_su=zeros(N,1);
P_exp_ex=zeros(N,1);
H_exp_su=zeros(N,1);
H_exp_ex=zeros(N,1);

.......
```

In the for loop “Worksheet”, xlsread loads data from each excel worksheet (when we stop tests in Labview, a new start needs a new TDMS file, so there's a file every day or middle day), the 66th column is “test number”. A second “for loop” allows to every test number's element to go inside an “if loop” which increases a counter and builds “point vector” if “test number” is higher than zero and different from the value of the previous row. Once “point vector” is built, it's possible initializing other vectors which are going to be filled at the end of the code with the results.

```
V=0;
for s=1:sheet %% Reading each worksheet%%
fprintf('Worksheet number %d\n',s);
Dati=xlsread('Data_TALLURI.xlsx',s);
test_number=Dati(:,66);
Index=3000;
N_index=0;
for test=1:length(test_number) %% search data in steady state condition ...
for n=1:N_index ...
V=V+N_index;
end
```

Fig. 3.16 Compact view of the main section of the code where the RM is applied

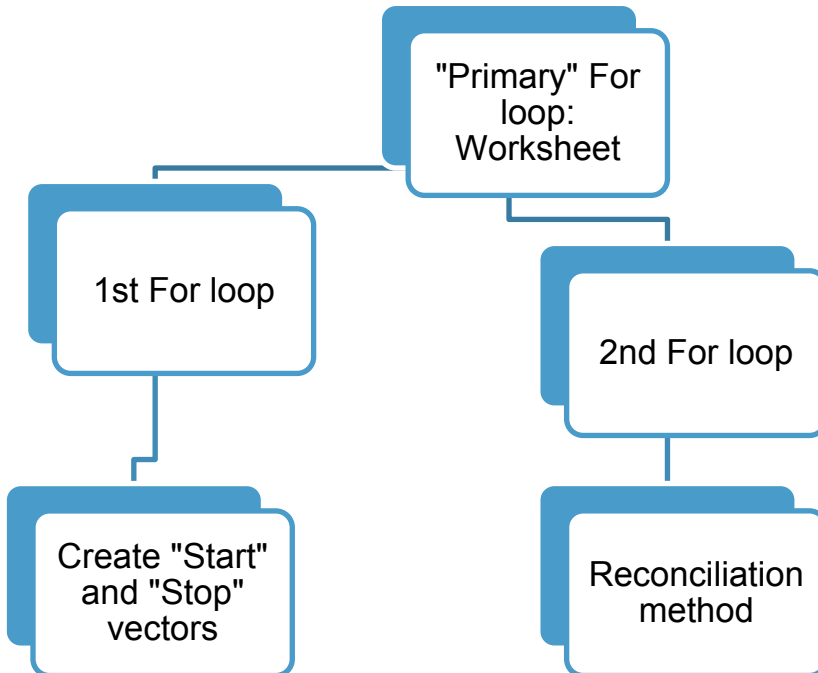


Fig. 3.17 Schematic view of the main section of the code where the RM is applied

To begin the calculation and apply the reconciliation method, another “for loop” is necessary as we can see in Fig. 3.16 and Fig. 3.17.

Inside this loop there are other 2 “for loop”:

- the first to create (using 2 “if loop”) the “start_vector” and the “stop_vector” which are the upper and the lower bound of a steady state condition; this loop increases also a counter (N_index) for every steady condition tested, N_index is summed to another counter “V” at the end of the primary “for loop”
- the second to create vectors loading variables from start to stop, so all of the vectors are going to represent a steady state condition

```

for s=1:sheet %% Reading each worksheet%%
fprintf('Worksheet number %d\n',s);
Dati=xlsread('Data_TALLURI.xlsx',s);
test_number=Dati(:,66);
Index=3000;
N_index=0;
for test=1:length(test_number) %% search data in steady state condition
    if test_number(test)~=Index && test_number(test)>0 %% during the tests, points with the same test_number value(different from zero)
        correspond to points with the same boundaries
        Index=test_number(test); %% if test_number=0 means we weren't in steady state conditions
        N_index=N_index+1;
        Start_vector(N_index)=test; %% each value of the vector is the Start index for a condition
    end
    if test_number(test)==Index && test_number(test+1)==0
        Stop_vector(N_index)=test; %% each value of the vector is the Stop index for a condition
    end
end
for n=1:N_index
    Start=Start_vector(n);
    Stop=Stop_vector(n);
    M=Dati(Start:Stop,49)/1000; %% kg/s
    Pin=Dati(Start:Stop,35)*100000; %%Pa because CoolProp use Pascal
    Pout=Dati(Start:Stop,36)*100000;
    .....

```

Now data are ready to be handle and the following chapters are going to explain every step of the reconciliation method and how it has been made in the Matlab code.

All of the method is obviously made in the second “for loop”, because the previous steps ables to work with data belonging to a steady state configuration.

Validation of measurements

This first step enables to check quality of data because every measured value has to respect physical laws like energy and mass balance. However, this redundancy needs that every element of a balance is measured, and this is easier for example in a heat exchanger or when it's possible measuring mass flow rate 2 or more times during the cycle. This step is also more appropriate when an all cycle is studied and not just a component of it.

So, having the goal to study just the expander and having not enough sensors to perform this step, it wasn't considered.

Elimination of outliers

This step ensures to eliminate of the irrelevant measurements (outliers). An example is given in Fig. 3.18 where the criterion is based on a 1.96 standard deviation. Points 7 and 90 are therefore considered as outliers in this case.

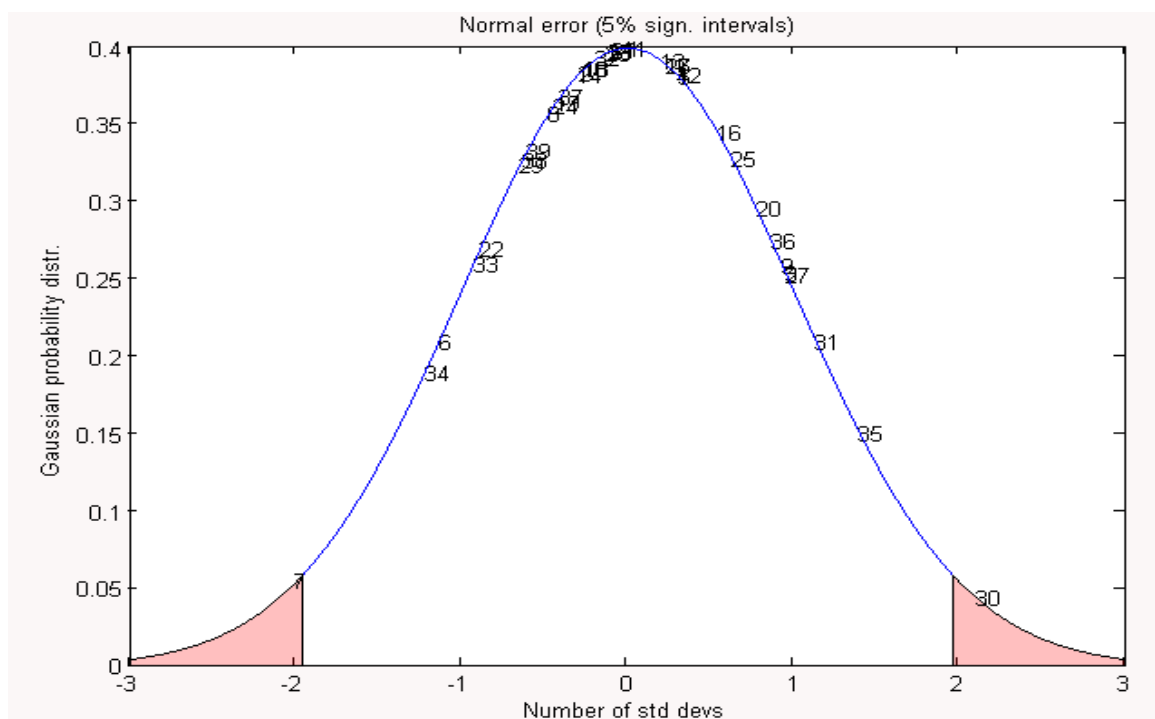


Fig. 3.18 Elimination of outliers

In the conducted experimental campaign, the elimination of outliers was performed for measured data and variables depended by them.

The standard deviation used for a variable was the maximum between 2 kinds of standard deviation:

- The one calculated with the Matlab function
- The one taking into account sensor's data sheet

Here below there's an example of the Matlab calculation for a variable's standard deviation.

```
%%standard deviation
std_M(n+V)=std(M);
if std_M(n+V)>Delta_M
    Delta_M=std_M(n+V);
end
```

The value “Delta_M” generated by the “if loop” will be the standard deviation used. Once this step is done, it’s possible to eliminate the outliers:

```
%%elimination of outliers
out_m=0;
for o_m=1:length(M)
    if M(o_m)>M_mean+Delta_M || M(o_m)<M_mean-Delta_M
        M(o_m)=0;
        out_m=out_m+1;
    end
end
N_M_in=length(M)-out_m;
M_in=zeros(N_M_in,1);
in_M=0;
for z_m=1:length(M)
    if M(z_m)~=0
        in_M=in_M+1;
        M_in(in_M)=M(z_m);
    end
end
```

Inside the vector “M” there are all of the flow rate measured during a test, this step builds a new vector called “M_in” where there aren’t outliers.

In the Matlab code, this is made for the following variables:

- Flow rate (kg/s)
- T_exp_su (°C)
- T_exp_ex (°C)
- P_exp_su (Pa)
- P_exp_ex (Pa)
- Torq (N*M)
- H_exp_su(kJ/kg): using CoolProp in Matlab that ables to calculate enthalpy having temperature, pressure and fluid as input
- H_exp_ex(kJ/kg): using CoolProp in Matlab that ables to calculate enthalpy having temperature, pressure and fluid as input

3.4.4 Reconciliation method-Application

The valuation of eq. (3.1) was performed for every variable and all summation was added together. The RM method has characterized by 2 constraints:

- Each variable has to be included between its mean value and standard deviation
- Energy balance has to be validated

The Matlab function that allows to minimize a function with linear or nonlinear constraints is called “fmincon”.

fmincon finds a constrained minimum of a scalar function of several variables starting at an initial estimate. This is generally referred to as constrained nonlinear optimization or nonlinear programming.

`x = fmincon(fun,x0,A,b,Aeq,beq,lb,ub,nonlcon,options)` starts at `x0` and finds a minimum `x` to the function described in `fun`, `x0` can be a scalar, vector or matrix.

- `A` and `b` define linear inequalities: $A \cdot x \leq b$
- `Aeq` and `beq` define linear equalities: $Aeq \cdot x = beq$
- `lb`, `ub` are the upper and lower bounds on the design variables, `x`, so the solution is always in the range $lb \leq x \leq ub$
- `nonlcon` define nonlinear constraints: needs a function that returns a value `c` if there's a linear inequalities or returns a value `ceq` if there's a linear equalities.
- `options` allows to set optimization parameters using the function `optimset`

In the Matlab code, it has been used an extended version of fmincon to have more outputs:

```
[x,fval,exitflag,output]=fmincon(obj,x0,A,b,Aeq,beq,lb,ub,nonlcon,options)
```

This version gives us other outputs like the value of the function (`fval`), the exit condition of fmincon (`exitflag`) and a structure (`output`) with informations about the optimization.

```
%%Reconciliation method-Find the minimum%%
x0=[Torq_mean;M_mean;Pin_mean;Pout_mean;Tin_mean;Tout_mean;Tamb_mean;Bloss;...]; %%First guess values%%
lb=[Torq_mean-Delta_Torq;M_mean-Delta_M;Pin_mean-Delta_Pin;...];
ub=[Torq_mean+Delta_Torq;M_mean+Delta_M;Pin_mean+Delta_Pin;...];
obj=@(x)SumRes_Bloss(Torq_in,M_in,Pin_in,..,x,..,length(Torq_in),length(M_in),....);
nonlcon=@bound_Bloss;
A=[];

```

```

b=[];
Aeq=[];
beq=[];
Tol_bound =0.1; %%tolerance for constraints%%
Max_Iter=1000;
options=optimset('Algorithm','interiorpoint','TolCon',Tol_bound,'MaxIter',Max_Iter);
[x,fval,exitflag,output]=fmincon(obj,x0,A,b,Aeq,beq,lb,ub,nonlcon,options);

```

The initial guess values are mean values of vectors, lower(lb) and upper(ub) bounds use the same Delta used to eliminate outliers.

The function to minimize is SumRes_Bloss and it represents the equation (3.1), in the Matlab code it takes into account vectors without outliers so in the summation the number of index changes from variable to variable: the number of elements in “M_in” is different from the number of elements in “Torq_in”.

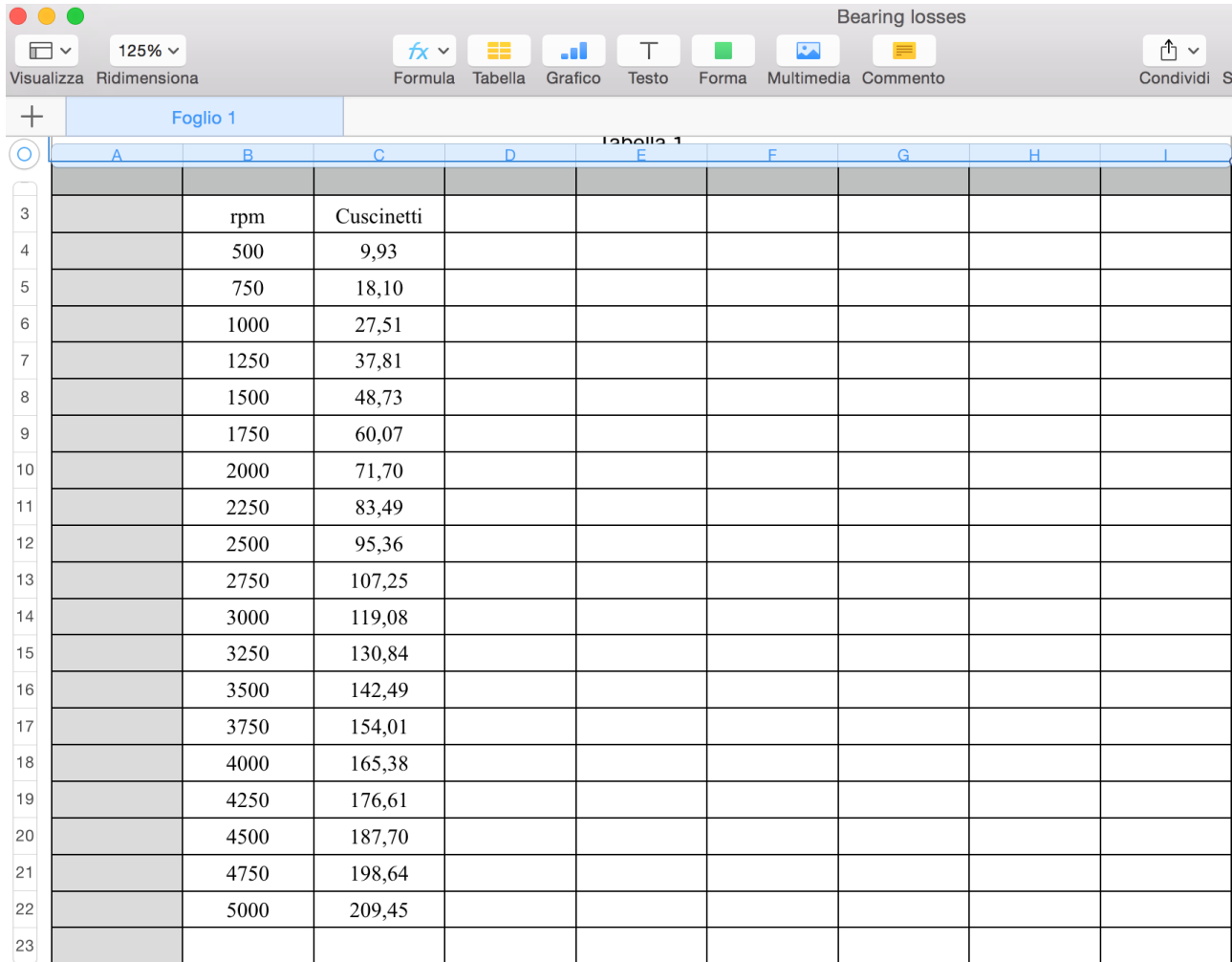
```

function
V=SumRes_Bloss(Torq,M,Pin,Pout,Tin,Tout,Tamb,Hin,Hout,Delta_Torq,Delta_M,Delta_Pin,Delta_Pout,Delta_Tin,Delta_Tout,Delta_Tamb,Delta_Hin,Delta_Hout,x,N_Torq,N_M,N_Pin,N_Pout,N_Tin,N_Tout,N_Tamb,N_Hin,N_Hout)
Torq_tot=0;
M_tot=0;
Pin_tot=0;
Pout_tot=0;
Tin_tot=0;
Tout_tot=0;
Hin_tot=0;
Hout_tot=0;
Tamb_tot=0;
for to=1:N_Torq
    Torq_tot=Torq_tot+(((Torq(to)-x(1))^(2))/((Delta_Torq)^2));
end
for m=1:N_M
    M_tot=M_tot+(((M(m)-x(2))^(2))/((Delta_M)^2));
end
for pin=1:N_Pin
    Pin_tot=Pin_tot+(((Pin(pin)-x(3))^(2))/((Delta_Pin)^2));
end
for pout=1:N_Pout
    Pout_tot=Pout_tot+(((Pout(pout)-x(4))^(2))/((Delta_Pout)^2));
end
.....
V=Torq_tot+M_tot+Pin_tot+Pout_tot+Tin_tot+Tout_tot+Tamb_tot+Hin_tot+Hout_tot;

```

Variables have also to respect constraints, the only constraint used is the energy balance:

$$W = m * (h_{in} - h_{out}) - B_{loss}$$



The screenshot shows an Excel spreadsheet window titled "Bearing losses". The ribbon menu includes "Visualizza", "Ridimensiona", "Formula", "Tabella", "Grafico", "Testo", "Forma", "Multimedia", "Commento", "Condividi", and "S...". The main sheet is titled "Foglio 1" and contains a table with two columns: "rpm" and "Cuscinetti". The data starts at row 3 and continues down to row 23. The "Cuscinetti" column lists values such as 9,93, 18,10, 27,51, 37,81, 48,73, 60,07, 71,70, 83,49, 95,36, 107,25, 119,08, 130,84, 142,49, 154,01, 165,38, 176,61, 187,70, 198,64, and 209,45.

3		rpm	Cuscinetti						
4		500	9,93						
5		750	18,10						
6		1000	27,51						
7		1250	37,81						
8		1500	48,73						
9		1750	60,07						
10		2000	71,70						
11		2250	83,49						
12		2500	95,36						
13		2750	107,25						
14		3000	119,08						
15		3250	130,84						
16		3500	142,49						
17		3750	154,01						
18		4000	165,38						
19		4250	176,61						
20		4500	187,70						
21		4750	198,64						
22		5000	209,45						
23									

Fig. 3.19 Bearing Losses

(3.2)

Where B_{loss} is the sum of bearing losses and friction losses due to the contact of the electromagnetic coupling.

Bearing losses were calculated using bearing data sheet (in the excel file called "Bearing losses"), where there's a loss for each rpm as we can see in Fig. 3.19.

Friction losses were calculated with the following formula

$$P_{loss} = \omega \cdot M_r$$

(3.3)

Where M_r is the frictional torque, which is the friction force time the radius of electromagnetic coupling, with a coefficient $f = 0.15$ for steel over steel materials.

```
%%Bearing losses%%
Corr=xlsread('Bearing losses.xlsx');
r=0,0175;
F=250;
f=0,15;
rpm_bloss=Corr(:,1);
cost=Corr(:,2);
Bloss=0;
for j=1:length(cost)
    if rpm_bloss(j)==rpm_mean
        Bloss=cost(j)+r*f*F*rad_s_mean;
    end
end
```

The function that defines a nonlinear equality as a constraint for fmincon is called “bound_Bloss”, the torque ($x(1)$) is summed to 0,33 because the torque meter used during these tests had a systematic offset of 0,33.

```
function [c,ceq]=bound_Bloss(x)
c=[];
rad_s=x(12)*2*pi/60;
W=rad_s*(x(1)+0,33);
ceq=W-x(2)*(x(10)-x(11))+x(8);
```

In the end, the function optimset defines options about optimization as the tolerance accepted for the bound, optimization algorithm and maximum iteration’s number.

Validation of Reconciliation

Finally, to check the confidence of the corrected values, residues should be verified *a posteriori* and the weighted deviation (w_i) should be evaluated (Eq.(3.4)) to give the confidence level of the correction.

$$w_i = \frac{|u_i - c_i|}{\sigma_i} \quad (3.4)$$

```
Flow_weight(n+V)=abs(Flow(n+V)-Flow_mean(n+V))/Delta_M;
```

This is an example to evaluate the weight of the reconciled flowrate’s value.

Output

Matlab code ends printing and graphing optimization's results. Vectors called "performance indicators" are filled with results, the index of each row is (n+V) where "V" is the counter of the primary "for loop" explained in chapter "Link Labview-Matlab" and "n" is the steady state configuration's index belonging to the second "for loop".

```
.....
Flow(n+V)=x(2);
Flow_mean(n+V)=M_mean;
Flow_weight(n+V)=abs(Flow(n+V)-Flow_mean(n+V))/Delta_M;
Delta_Flow(n+V)=Delta_M;
.....
fprintf('fval=%8.4f\n',fval);
output
fprintf('Variables Values\nP=%5.3f Watt\nHin=%6.3f\nHout=%6.3f\nHout_i_s=%6.3f\nDelta_H=%6.3f\nm=%8.6f kg/s\nSH=%f\nPin=%6.3f
Pa\nPout=%6.3fPa\nTin=%6.2f K\nTout=%6.2f
K\nrpm=%6.3f\nBearinglosses=%6.3f\nBeta=%f\nEta_th=%f\nEta_th_mean=%f\nEta_mech=%f\n',Pot(n+V),x(10),x(11),Hout_is,DH,x(2),S
H(n+V),x(3),x(4),x(5),x(6),x(12),x(8),Beta(n+V),Eta_th(n+V),Eta_th_mean(n+V),Eta_mech(n+V))
end
V=V+N_index;
end
```

This last "end" is of the primary "for loop" (Fig. 3.16), so for every index the code prints a message like the following:

Local minimum found that satisfies the constraints.

Optimization completed because the objective function is non-decreasing in feasible directions, to within the default value of the optimality tolerance, and constraints are satisfied to within the selected value of the constraint tolerance.

<stopping criteria details>

fval=859.8413

output =

struct with fields:

```
iterations: 35
funcCount: 490
constrviolation: 9.3223e-12
stepsize: 1.4445e-04
algorithm: 'interior-point'
firstorderopt: 0.0048
cgiterations: 5
```

message: 'Local minimum found that satisfies the constraints.>>>Optimization completed because the objective function is non-decreasing in.....'

Variables Values

$P=334,033 \text{ Watt}$
 $Hin=492395,074$
 $Hout=490422,379$
 $Hout_i_s=480601,255$
 $\Delta H=1972,695$
 $m=0,363487 \text{ kg/s}$
 $SH=4,679494$
 $Pin=616523,365 \text{ Pa}$
 $Pout=337929,191 \text{ Pa}$
 $Tin=355,20 \text{ K}$
 $Tout=347,02 \text{ K}$
 $rpm=3500,000$
 $Bearinglosses=383,016$
 $Beta=1,824416$
 $Eta_th=0,465844$
 $Eta_th_mean=0,548195$
 $Eta_mech=0,077919$

So we can have information about the optimization and every reconciled value. The code, once the primary “for loop” is closed, graphs results and creates some table which are loaded in another Excel file.

The last table(Table_good) is made by another for loop that creates a table just with data that respect energy balance with a low tolerance and haven't a mean weight too high.

The mean weight is the ratio between weights and the number of variables to which the method has been applied.

```

n_row=0;
for g=1:length(Point)
    if constr_viol(g)<0.1 && weights_mean(g)<0,3 && Bearing_Loss(g)~=0
        n_row=n_row+1;
        Table_good(n_row,:)=Table(g,:);
    end
end

writetable(Table,'Results_TALLURI_OnlyBloss.xlsx','Sheet',1);
writetable(Table_mean,'Results_TALLURI_OnlyBloss.xlsx','Sheet',2);
writetable(Table_weights,'Results_TALLURI_OnlyBloss.xlsx','Sheet',3);
writetable(Table_valutation,'Results_TALLURI_OnlyBloss.xlsx','Sheet',4);
writetable(Table_good,'Results_TALLURI_OnlyBloss.xlsx','Sheet',5);

figure;
scatter(Beta,Flow);
hold on

```

```

scatter(Beta_mean,Flow_mean);
title('Beta-Flow');
....
```

3.5 Experimental Results

This section is about experimental results and Reconciliation method's verification, so first of all this section shows Reconciliation method's effects and then discusses about experimental results.

3.5.1 Reconciliation method's effects

The method, as it's shown in section 3.4, enables to perform data which respect the energy balance minimizing a function that allows an equal distribution of errors.

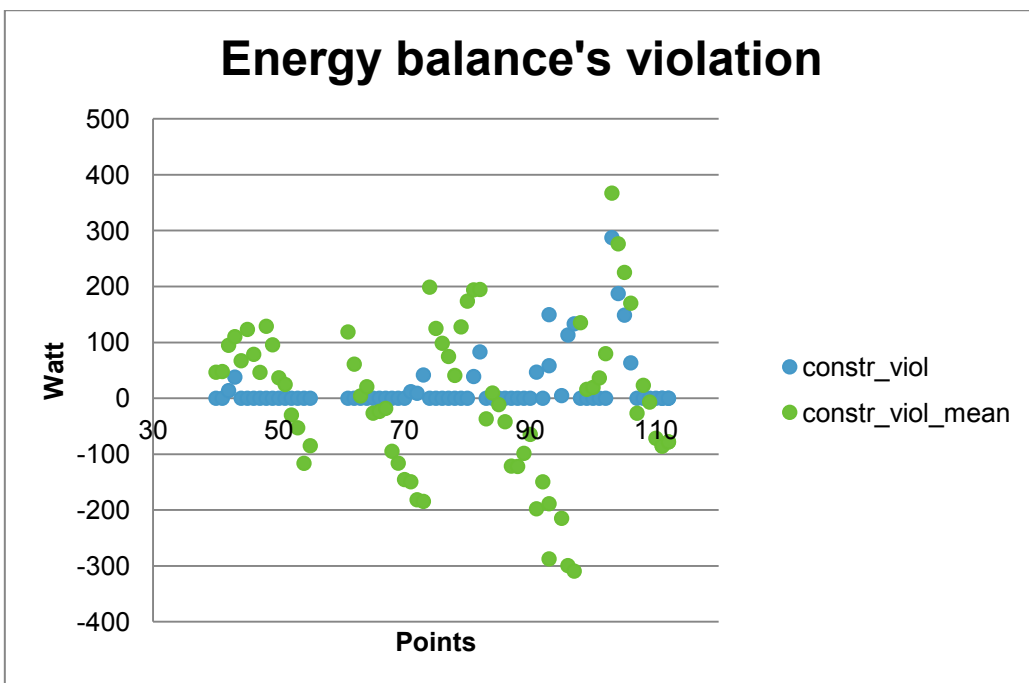


Fig. 3.20 Energy balance's violation for Reconciled and mean data

In Fig. 3.20 there's the energy balance of Reconciled values (blue) and of mean values(green); this graph is very important because enables to take off data that don't respect energy balance. Differences between Reconciled and mean values are very high for most of the points and Reconciled values performs a better solution of Energy balance. In many points there's a big difference between Reconciled energy balance and mean energy balance, it means that using mean values can cause high errors.

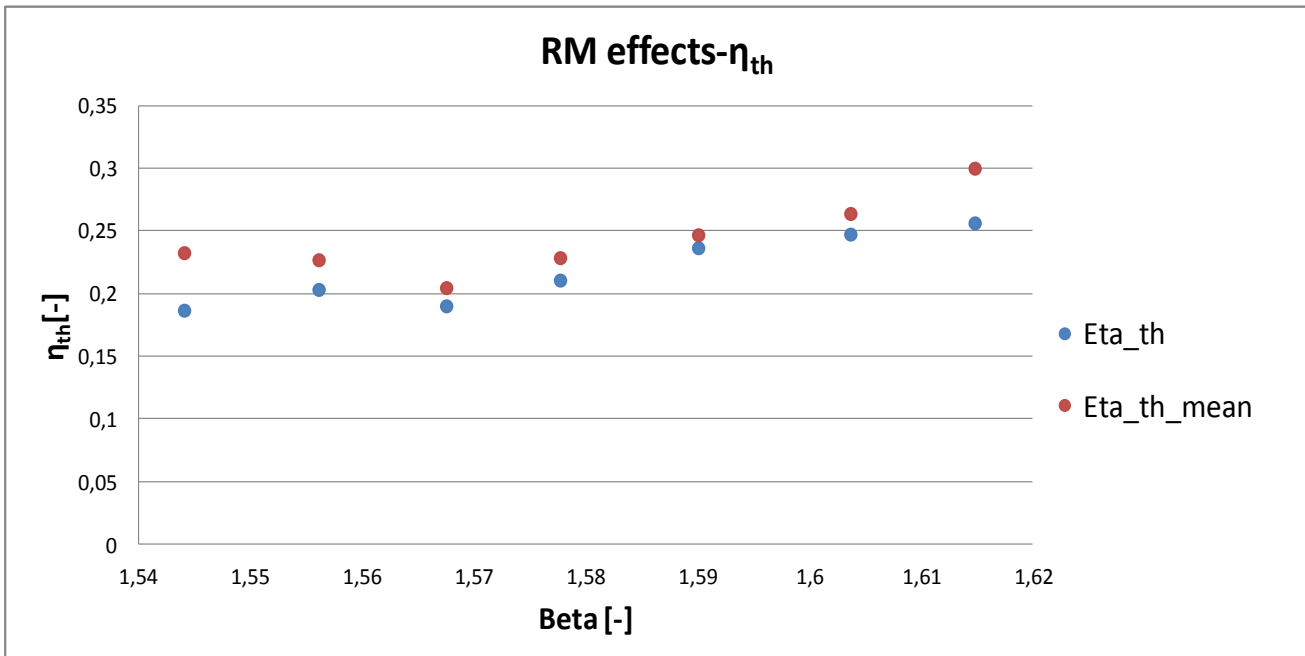


Fig. 3.21 Reconciliation method's effect for efficiency

In Fig. 3.21 there's an example of thermodynamic efficiency calculated with reconciled values (Eta_{th}) and with mean values ($\text{Eta}_{\text{th_mean}}$) in function of pressure ratio taking into account the same flow rate ($m=0,25 \text{ kg/s}$).

In some points Eta_{th} is different from $\text{Eta}_{\text{th_mean}}$ of 0,5 that it's not an irrelevant error especially if it's about efficiency.

Every Reconciled point in Fig. 3.21 belongs to a perfect energy balance's solution, but big differences between reconciled and mean values cannot be explained just with a better solution of energy balance because the weights have a key role too.

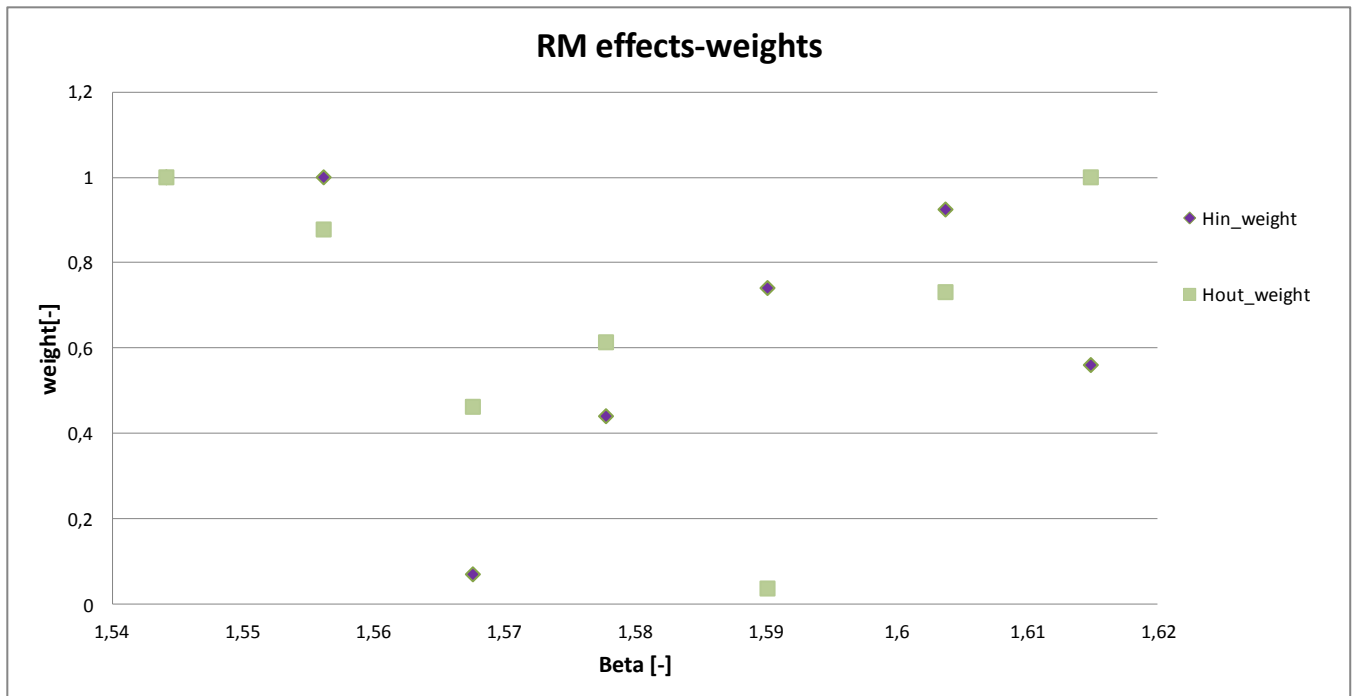


Fig. 3.22 Inlet and Outlet Enthalpy's weights

Thermodynamic efficiency depended by inlet and outlet enthalpy, in Fig. 3.22 there are inlet and outlet enthalpy about the same configurations of Fig. 3.21.

We can see that where enthalpy's weight is very high, there's a big gap between reconciled and mean thermodynamic efficiency. A weight equal to 1(eq.(3.4)) means that it has been taken into account the farthest data from the mean value, an oscillation that enables to respect energy balance but too high.

Indeed, considering Fig. 3.18, having a weight equal to 1 means that data are on the border between white and red area, so on the border between the acceptable and the unacceptable area by the instrument's standard deviation.

This type of data, while respecting the energy balance with a small error (in Fig. 3.23 they are between a weight of 0,3 and 0,4), can be eliminated since they are very close to the error.

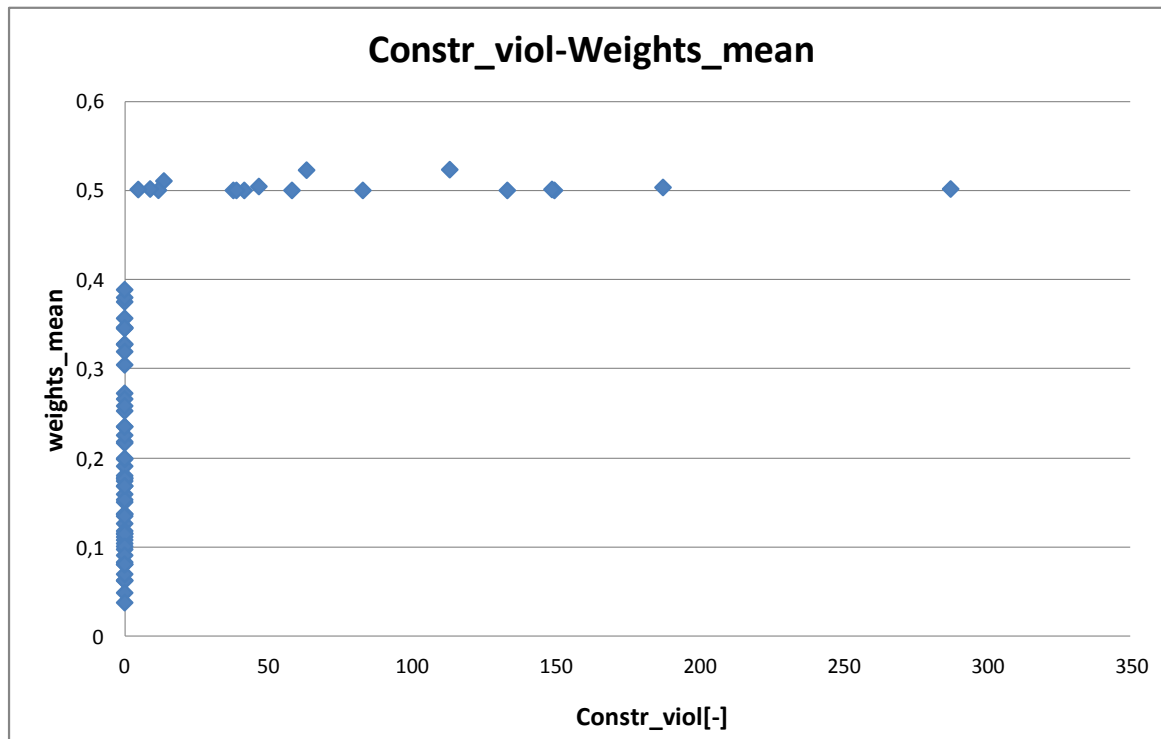


Fig. 3.23 Comparison between constraints violation and weights

In Fig. 3.23, weights_mean is the ratio between weights and the number of variables to which the method has been applied and it's above 0,5 when constraints violation are high. Between 0,3 and 0,4 constraints are respected but it has been decided not taking into account data with a mean weight like this because of the high oscillation.

3.5.2 Reconciled results

The experimental campaign was conducted exploring different refrigerant mass flow rates (0,25 – 0,36 kg/s), varying the rotational speed of the expander (1000 – 5000 rpm), as well as total inlet pressure (4,7 – 6,7 bar) and super heating levels (3,2 – 46 °C).

In order to have confident temperature measurements, the turbine and the inlet and outlet pipes were insulated.

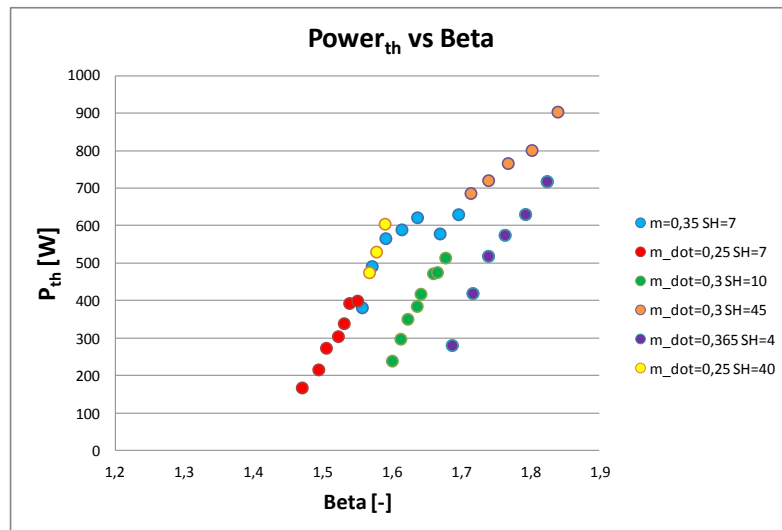


Fig. 3.24 Thermodynamic power and pressure ratio for different flow rates and superheating levels

The maximum achieved experimental thermodynamic power was 906 W, with a mass flow rate of 0,299 kg/s, 44 °C super heating level and 5000 rpm (Fig. 3.25). The highest power conditions were indeed obtained for high super heating levels, followed by high mass flow rate conditions. Furthermore, as expected, thermodynamic power increases as the expansion ratio augments. Fig. 3.24 displays the behavior of thermodynamic power as function of the expansion ratio.

It is very interesting to notice that the same expansion ratio can be reached either with a high super heating level or with a higher mass flow rate, but the power production is higher in the former case. Indeed, if we take as an example, an expansion ratio of about 1,8, it can be seen from Fig. 3.24 that the turbine produces nearly 18% more power with a mass flow rate of 0,299 kg/s and a super heating level of 45°C compared to the case with 0,365 kg/s of mass flow rate around 4°C super heating level. This is due to the better match between rotational speed and tangential velocity, allowing therefore a better power conversion.

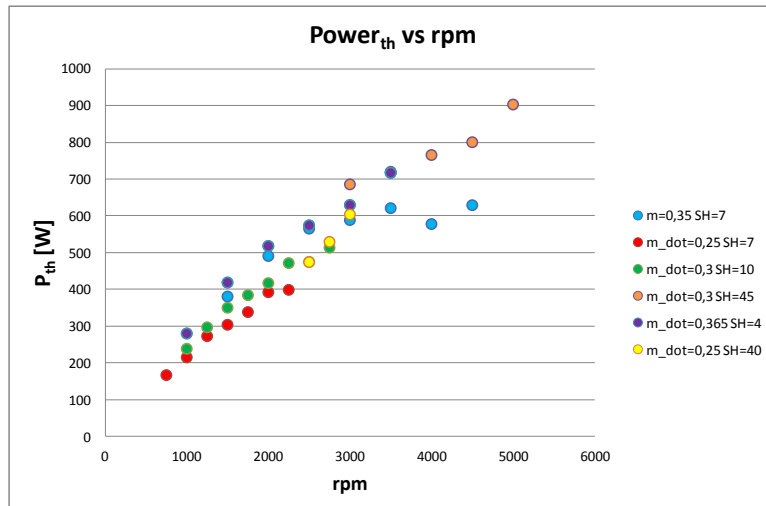


Fig. 3.25 Thermodynamic power and rpm for different flow rates and superheating levels

Thermodynamic power production monotonically increases with rotational speed, it can be noticed another time that at the same rpm (3000) a lower flow rate(0,3 kg/s) with a high superheating level provides a higher power production compared to a higher mass flow rate with a low superheating level.

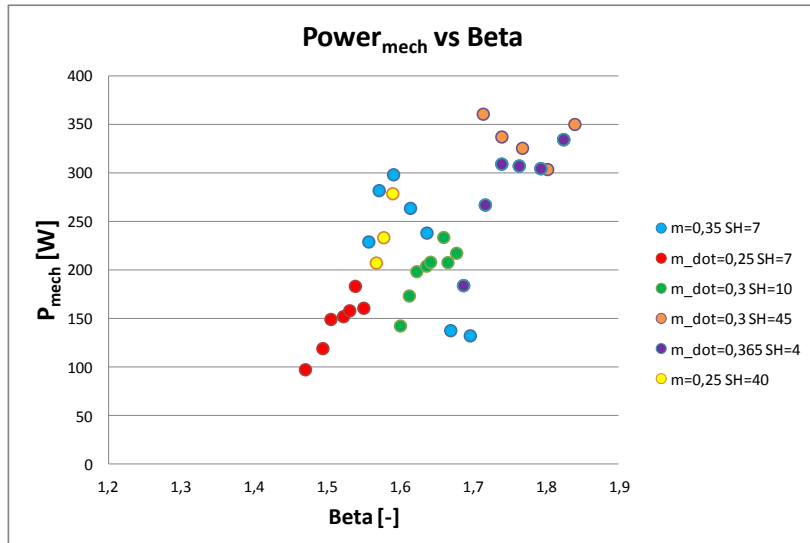


Fig. 3.26 Shaft power and pressure ratio for different flow rates and superheating levels

Differently from experimental thermodynamic power, the maximum achieved shaft power output was 371 W and it was reached with a mass flow rate of 0,3 kg/s, a super heating level of 45 °C and a rotational speed of 4000 rpm.

As can be easily noticed comparing Fig. 3.24 and Fig. 3.26, the shaft power output shows a different behavior compared to the thermodynamic one. Particularly, the behavior of the thermodynamic power output is monotonically increasing with expansion ratio (and rotational speed), while the shaft power output presents a maximization point.

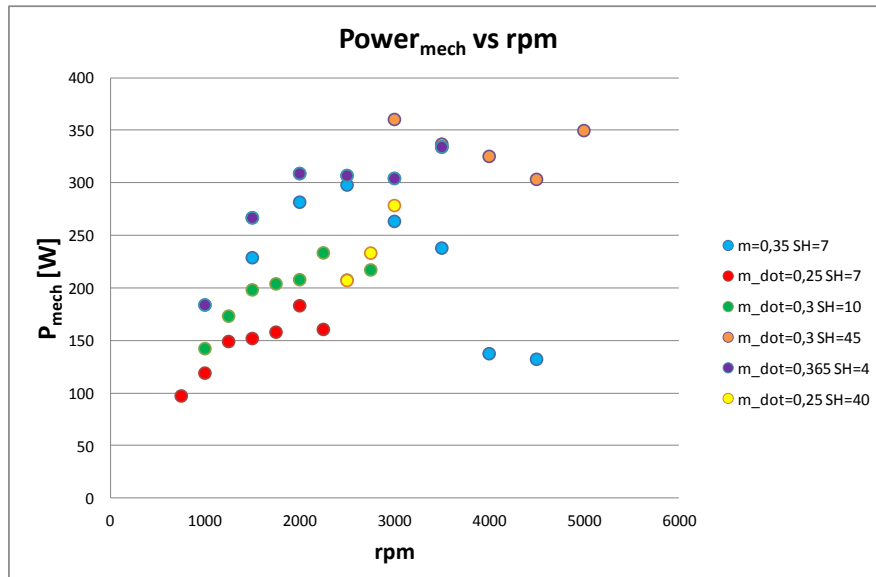


Fig. 3.27 Shaft power and rpm for different flow rates and superheating levels

The trend of shaft power can be better understood when analyzing Fig. 3.27. Indeed, in Fig. 3.27 the shaft power is displayed as a function of rotational speed. Expansion ratio increases when augmenting the rotational speed of the turbine, but it also directly raises the mechanical losses due to the bearings, as well as the friction losses due to the electromagnetic coupling.

On average, a 50% organic efficiency was achieved that is a really low value, mostly attributable to the improper alignment of the magnetic coupling, which is responsible for a really high increase of the mechanical losses, due to the friction.

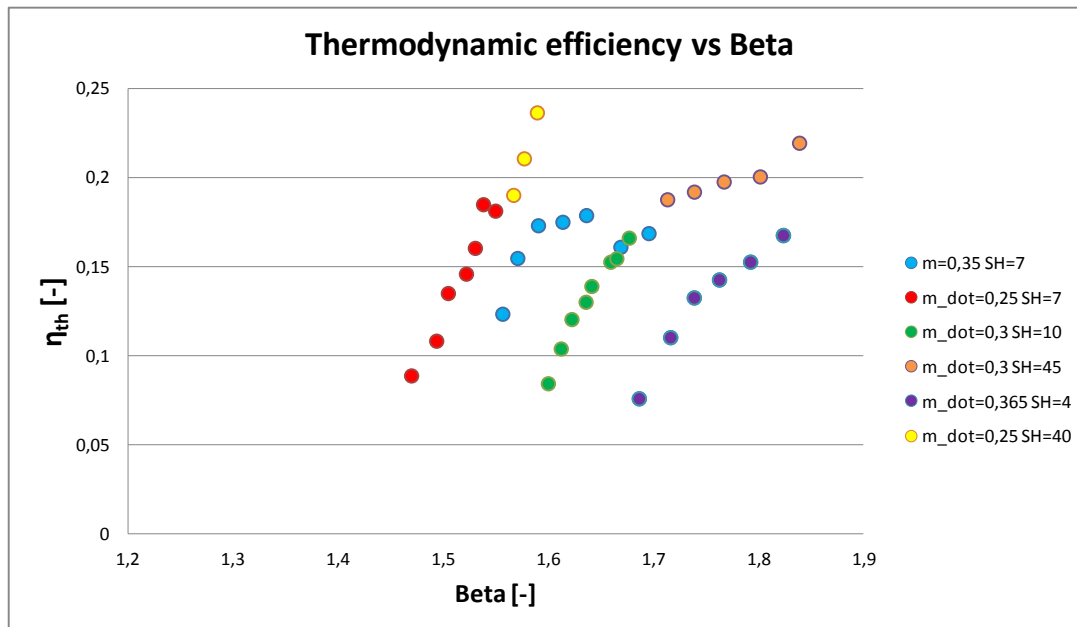


Fig. 3.28 Thermodynamic efficiency and pressure ratio for different flow rates and superheating levels

The maximum achieved experimental thermodynamic total to total efficiency was 24% with a mass flow rate of 0,25 kg/s, a super heating level of 40 °C and a rotational speed of 3000 rpm.

Highest efficiency values are directly related to the thermodynamic power production; nonetheless, as expected for a Tesla turbine, higher efficiencies are achieved at low mass flow rates. Indeed, Fig. 3.24 and Fig. 3.28 are examined together. It clearly appears that there is a direct relationship between power production and efficiency. However, the low mass flow rates conditions achieve higher efficiencies compared to the high mass flow rates. On the whole, an average 17% thermodynamic efficiency was obtained for this expander, with higher values for low mass flow rate conditions.

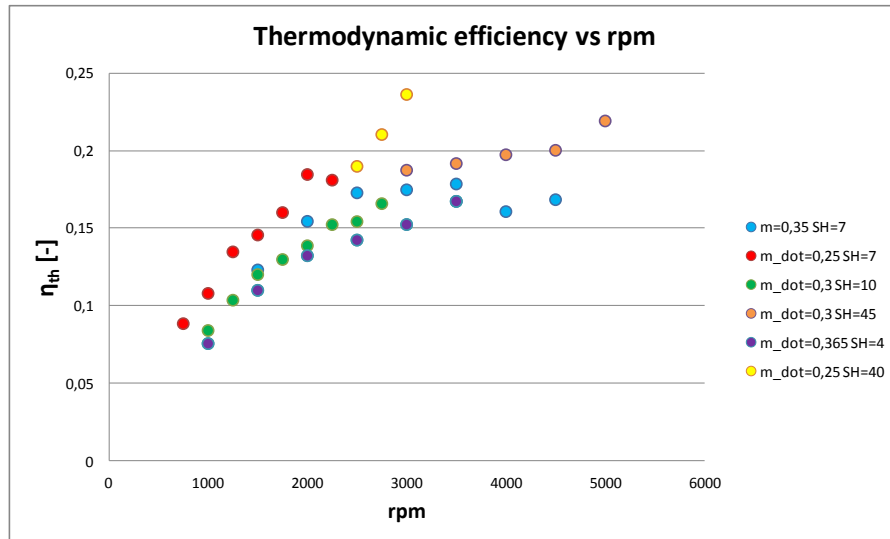


Fig. 3.29 Thermodynamic efficiency and rpm for different flow rates and superheating levels

The shaft efficiency (Fig. 3.30), on the other hand, is directly related to the obtained shaft power. Therefore, the highest efficiency condition is achieved at the maximum power output condition, which is at a mass flow rate of 0,25 kg/s, a super heating level of 40°C and a rotational speed of 3000 rpm; and the achieved value of efficiency is of 11%.

Nonetheless, there is still an influence of the mass flow rate; at low mass flow rates, the efficiency still is still relatively high, even at lower power production.

On the whole, an average shaft efficiency of 8,2% was obtained for this expander, with higher values at low mass flow rate conditions and higher power production conditions

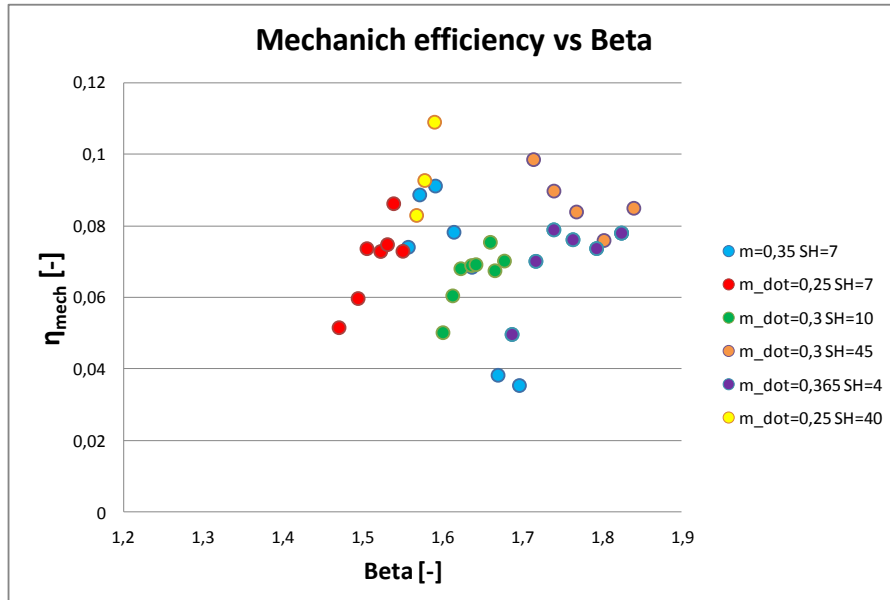


Fig. 3.30 Shaft efficiency and pressure ratio for different flow rates and superheating levels

As can be noted from the very big difference between thermodynamic and shaft efficiency, as well as from the values of organic efficiency, the mechanical power losses of the turbine are quite high.

Mechanical losses grow with rotational speed and can cause a drastically decrease, a condition with mass flow rate of 0,35 kg/s and superheating level of 7°C is an example.

The maximum is more or less in the same position of thermodynamic efficiency but after it, the decrease is more accentuated because mechanical losses are summed to organic losses.

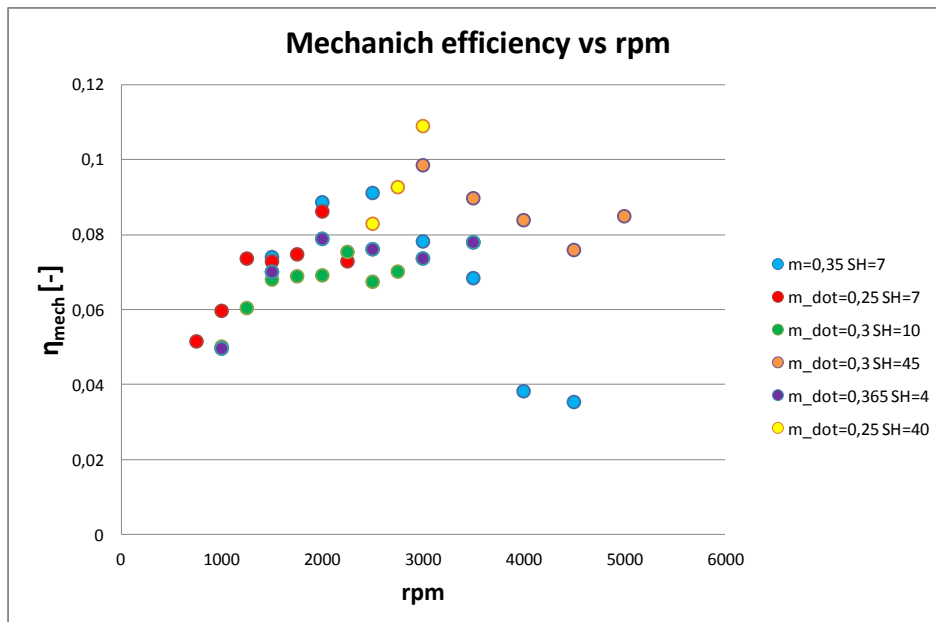


Fig. 3.31 Shaft efficiency and rpm for different flow rates and superheating levels

3.6 Future prototype development

The experimental campaign conducted in 2018 which is described in the previous section showed a very low efficiency.

Not only mechanical but also fluid dynamic losses need to be taken into account, especially flow blockage due to the throttling effects of disks edges, windage between end disks and the case and pumping losses.

This is physically due to the not proper sealing of the flow between rotor and casing: this effect is enhanced at relatively high expansion ratios (e.g. 2 ÷ 4), as happens in case of ORC Tesla expanders, whereas it is more or less negligible in case of modest expansion ratios, as in the case of working with air where the expander manages only few kPa pressure drops. As shown in Fig. 3.32, the size of the gap between end rotors and casing and the width between the disks channels are of

the same order of magnitude (tenths of millimeter), thus giving no preferential path to the flow.

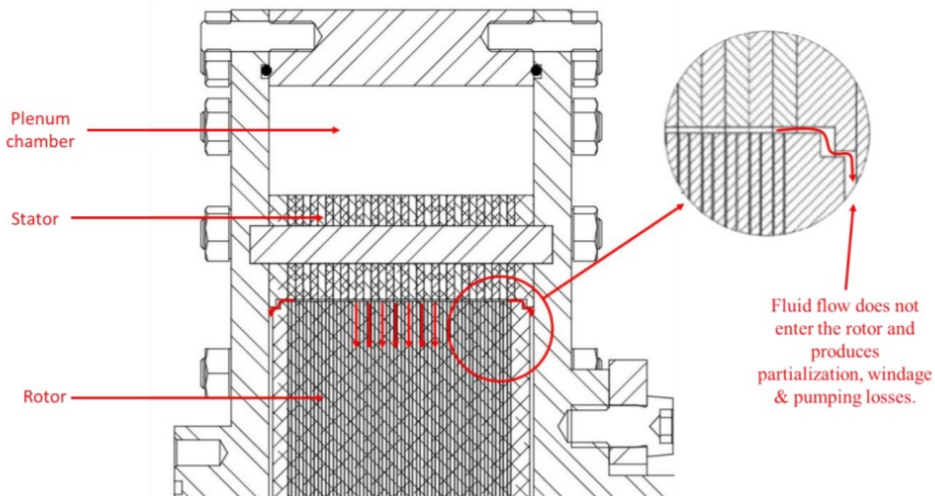


Fig. 3.32 Flow blockage

Consequently, a second phase of the experimental campaign was planned after the repeatability of old data.

In this second phase should have been tested the same prototype taking off the thinner disks(0,8 mm), to perform an easier entrance for the flow in the rotor in order to reduce blocking, windage and pumping losses.

After this verification, this “new” prototype will be tested with a two-phase flow; so this research continues to describe possible two phase Tesla application and also a thermo fluid dynamic model for two-phase application developed in EES.

4 Two-phase model

4.1 Possible applications

Two-phase turbines provide a way to operate in the wet region of water and steam mixtures or of organic fluids. In addition, two-phase, two-component mixtures such as steam and oil or steam and molten salts can, in principle, be used as working fluids in unusual cycles. Possible applications of two-phase turbines are in geothermal power, waste-heat recovery, refrigerant expansion, solar conversion, transportation turbine engines, and engine bottoming cycles. Potential advantages over conventional vapor cycles in these applications are more effective use of the energy in such hot liquids as geothermal fluids, better matching to sensible-heat sources, lower shaft speeds, and the flexibility of operating without the restriction of dry-vapor expansion.

One of the most promising applications of two-phase turbines is in closed-cycle engines using organic working fluids. The advantages over Rankine vapor cycles are better matching to the cooling curve of sensible-heat sources and elimination of the boiler. Possible applications are geothermal closed-cycle (binary) power plants, engine exhaust heat recovery, industrial waste-heat

recovery, and bottoming cycles for steam and gas turbine plants. Fig. 4.2 shows the equipment arrangement in an organic-fluid two-phase turbine engine. The fluid to be cooled (the "source fluid"), such as geothermal hot water or engine exhaust, flows through the heat exchanger from A to B and is cooled by counterflow heat transfer to the organic working fluid.

The working fluid is heated to saturation temperature. The saturated liquid, with possibly a small amount of vapor, flows to a two-phase nozzle. The liquid expands, partially vaporizes, and accelerates in the nozzle. The two-phase mixture drives the turbine rotor. The vapor is condensed, and the condensate is pumped back to the heater by a pump on the turbine shaft. The cycle is shown on a T-S diagram in Fig. 4.3. The state points are numbered to correspond with Fig. 4.2. The two-phase nozzle expansion takes the fluid from a saturated liquid at 150 °C (point 1) to a two-phase flow of 0,6 quality at 40 °C (point 2). The flow is decelerated in the rotor, condensed to point 4, and pumped back to nozzle inlet pressure at point 5.

The liquid is then reheated by the source fluid to point 1.

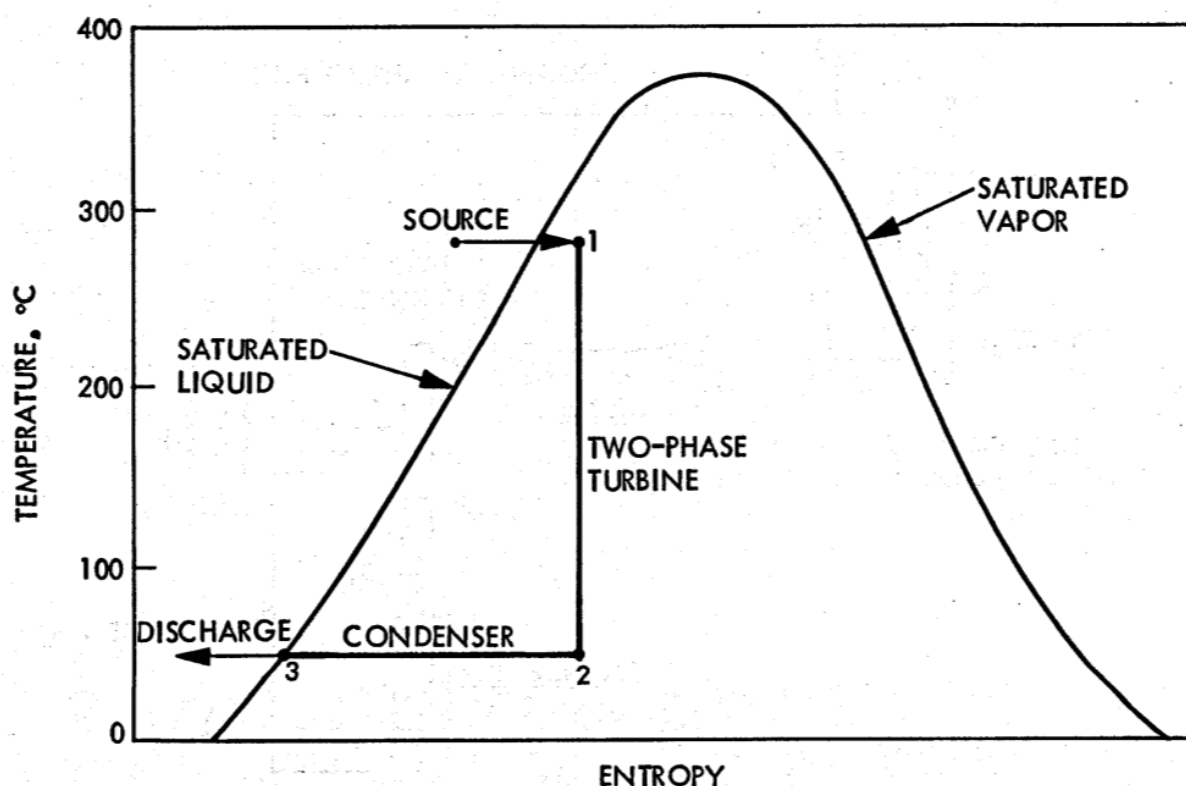


Fig. 4.1 Steam water cycle

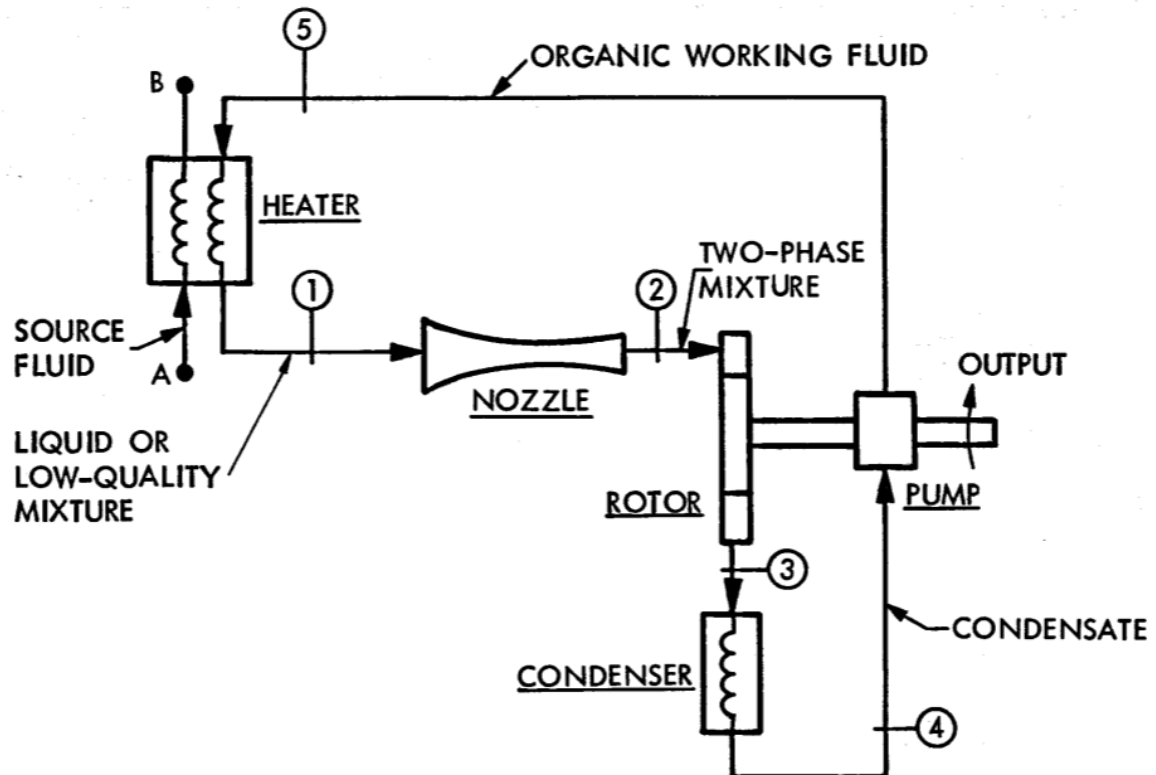


Fig. 4.2 Cycle's equipment [66]

The feature of this cycle that makes it ideal for recovery of energy from a sensible-heat source is the straight-line heating of the working fluid from point 5 to point 1 over the full temperature range of the cycle. The heating curve of the working fluid matches the cooling curve of the source fluid. The temperature difference between the source fluid and the working fluid can be kept small at all points in the heat exchanger. By contrast, the heating curve of a Rankine cycle, in which the working fluid must be boiled to dry vapor, is a poor match to the source-fluid cooling curve. Large differences are necessary between the source-fluid temperature and working-fluid temperature over portions of the heat exchanger, and it may not be possible to cool the source fluid all the way to ambient temperature; both effects reduce the available work.

The appropriate efficiency for comparison of waste-heat cycles is the "utilization efficiency," defined as the ratio of power output to heat available. The heat available is the heat that could be extracted by cooling the source fluid all the way to the low-temperature limit set by ambient temperature or other external limitations. If T_C is this low temperature cooling limit, then the available heat is

$$Q_A = \dot{m}c_p(T_A - T_C) \quad (4.1)$$

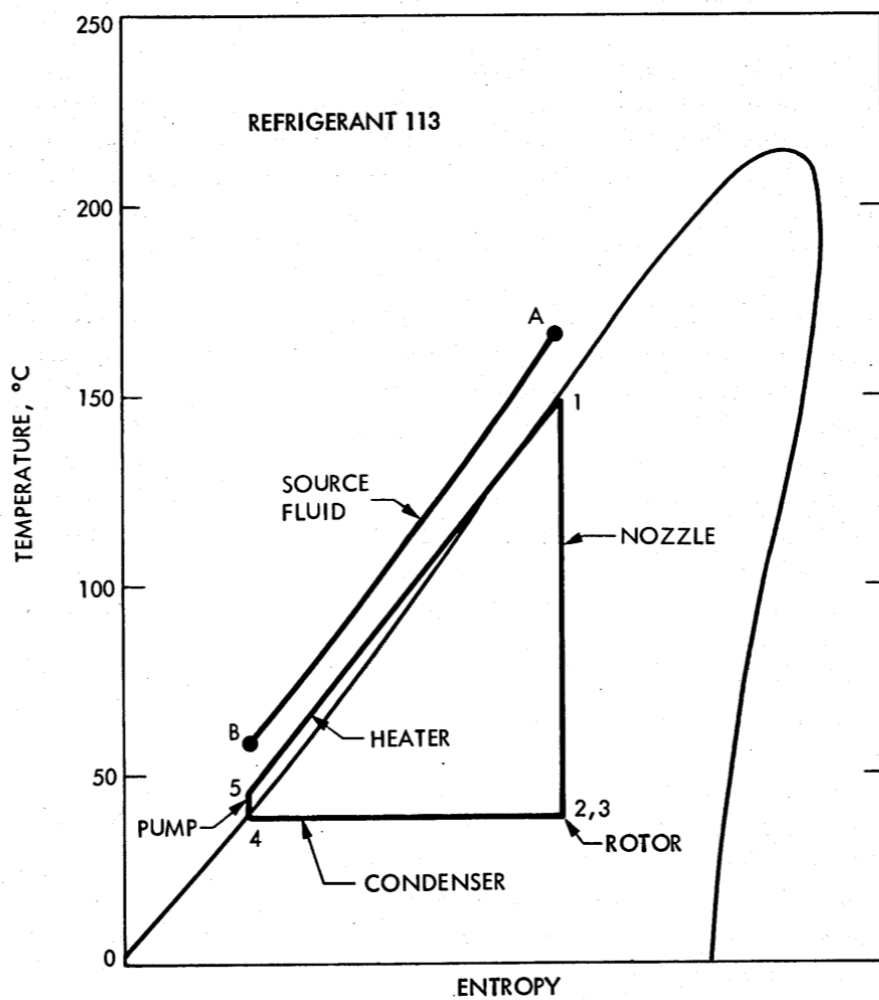


Fig. 4.3 T-s diagram of cycle of Fig. 4.2 [66]

The utilization efficiency is

$$\eta_u = \frac{P}{\dot{m}c_p(T_A - T_c)} \quad (4.2)$$

where P is the power output, and \dot{m} is the flow rate, c_p the specific heat, and T_A the initial temperature of the source fluid.

If, due to cycle limitations, the gas is cooled only part way to the cooling limit and leaves at a temperature T_B higher than T_c , then the heat input to the cycle is $\dot{m}c_p(T_A - T_B)$ and the cycle efficiency conventionally defined as

$$\eta_u = \frac{P}{\dot{m}c_p(T_A - T_B)} \quad (4.3)$$

From Eqs. (4.2) and (4.3), it can be seen that the utilization efficiency is the cycle efficiency multiplied by the ratio of actual to available source fluid temperature drop.

$$\eta_u = \eta \frac{(T_A - T_B)}{(T_A - T_C)} \quad (4.4)$$

In Fig. 4.4, the utilization efficiencies of two-phase and Rankine cycles are compared for the case in which the cooling limit is the same as the condensing, or rejection, temperature $T_R = 38^\circ\text{C}$, and the turbine and pump efficiencies are 100 percent. The two-phase cycle is 50 percent more efficient than the Rankine cycle for source fluid temperatures of 150 to 200 °C. The utilization efficiency of the two-phase cycle is close to the limiting efficiency W_A/Q_A corresponding to the available work W_A given by integration of the Carnot efficiency between T_A and T_R .

In an effort to better match the working fluid heating curve to the source fluid cooling curve, some geothermal studies have proposed supercritical Rankine cycles. Fig. 4.5 shows such a cycle using isobutane as the working fluid. The utilization efficiency, with $T_C = T_R = 380^\circ\text{C}$ and 100-percent turbine and pump efficiencies, is 0,157. A two-phase cycle using Li Refrigerant 113, Fig. 4.6, has a utilization efficiency of 0,173, a 10-percent gain.

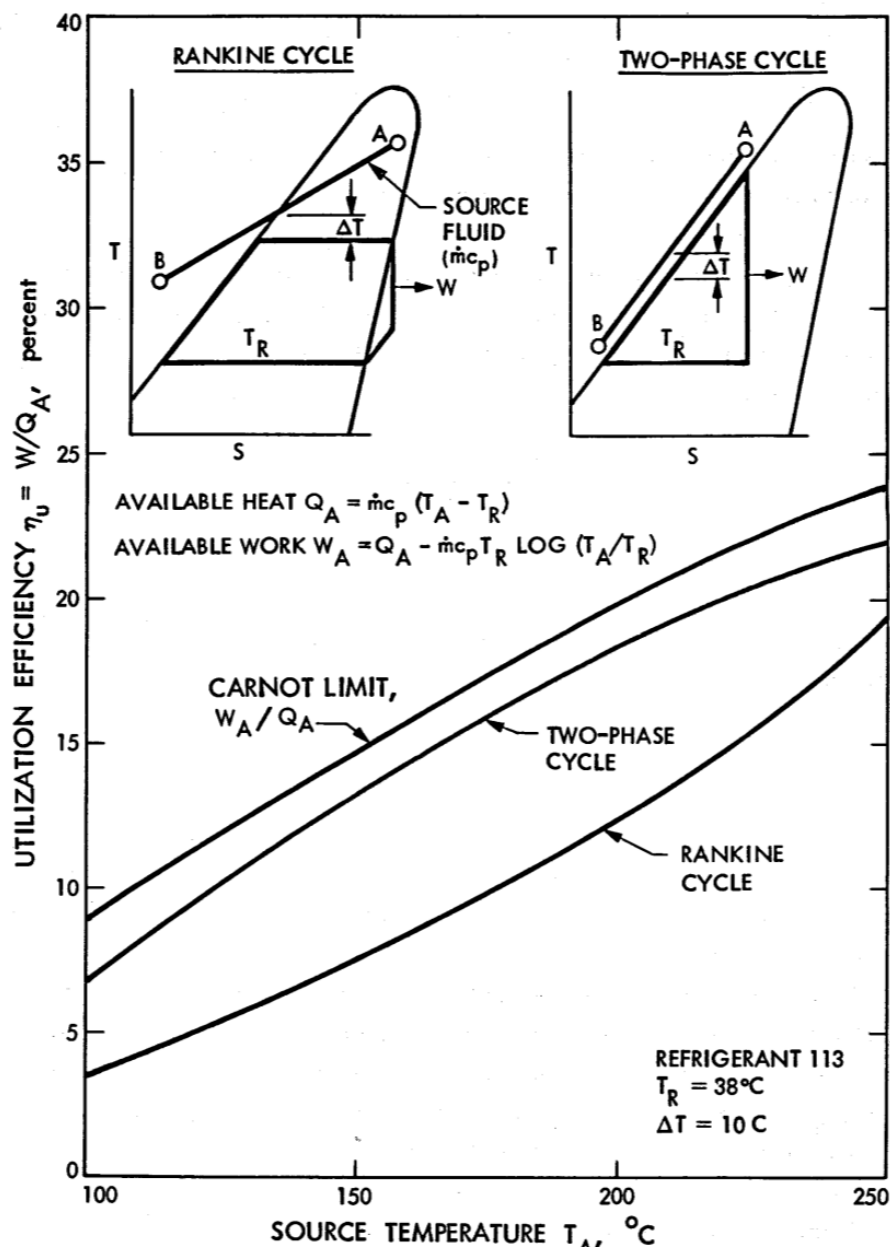


Fig. 4.4 Comparison with Rankine cycle [66]

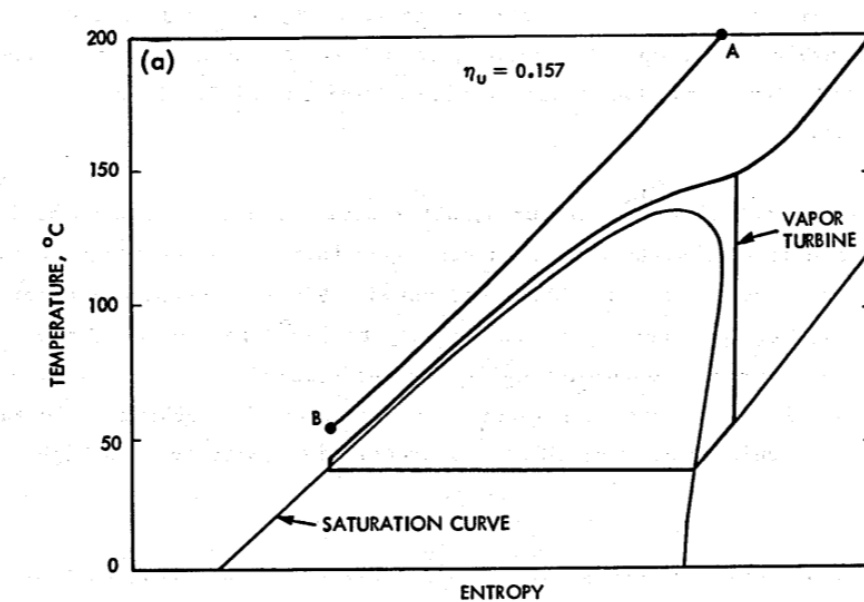


Fig. 4.5 Two phase cycle using Isobutane [66]

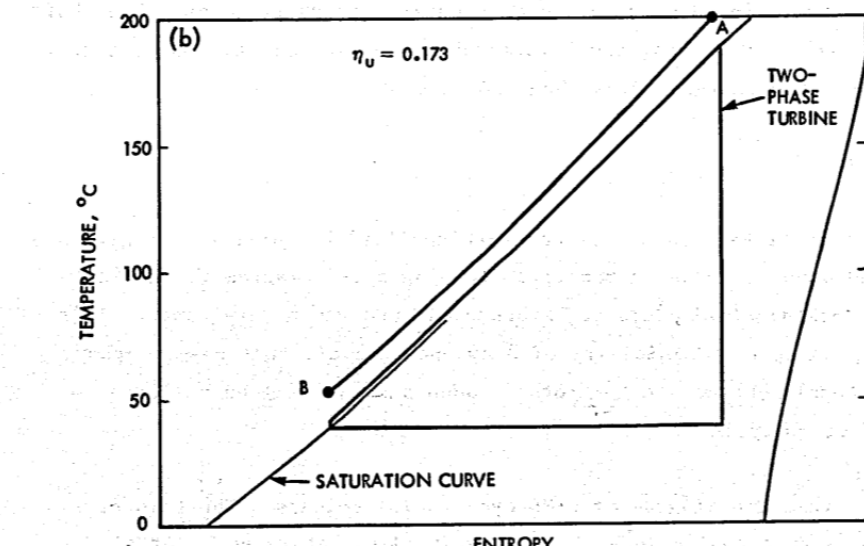


Fig. 4.6 Two phase cycle using Li Refrigerant [66]

At higher source fluid temperatures, water could be used as the working fluid. The main problem with water in a two-phase turbine is the large steam volume and high velocity at low exhaust pressures. Fig. 4.7 shows how water could be used at high pressure by expanding only to 150 °C in the two-phase cycle and using an organic bottoming cycle for the remainder of the temperature drop. In this way a good temperature match between the working fluid and the source fluid could be maintained at a source-fluid temperature as high as 350 °C.

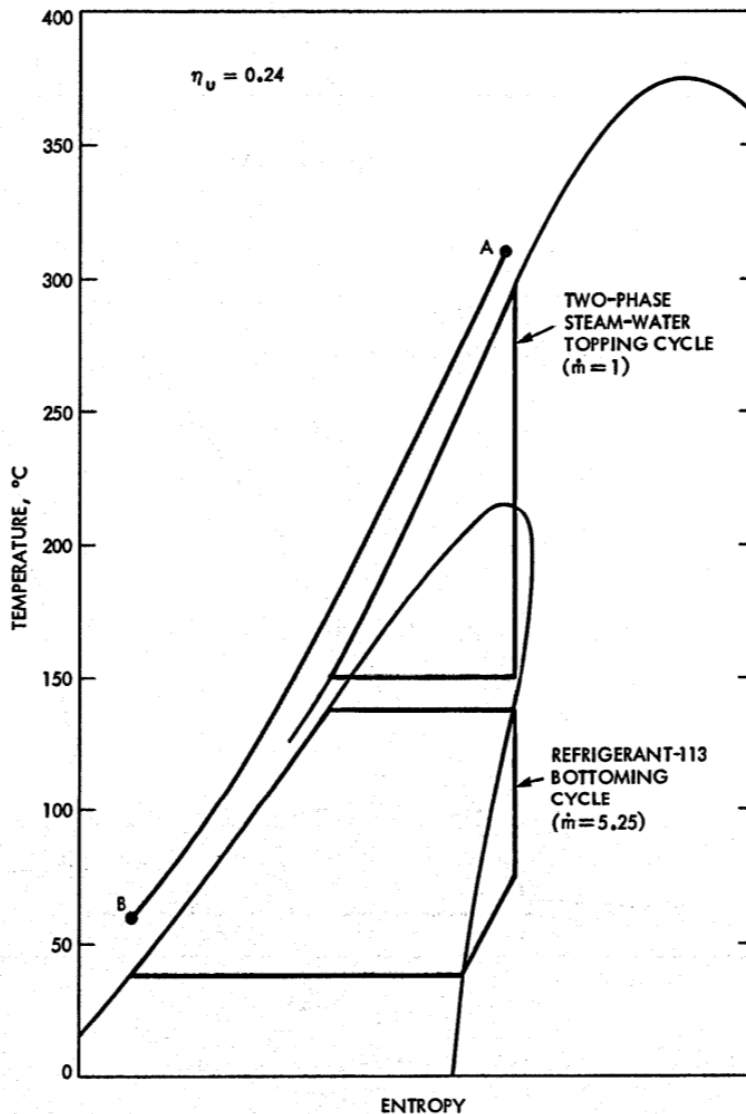


Fig. 4.7 Steam topping cycle with organic fluid bottoming cycle [66]

Another application of two-phase organic turbines is in refrigeration. Instead of throttling a refrigerant to produce cold liquid, the refrigerant could be expanded in a two-phase turbine. The work conventionally lost in the irreversible throttling process would be recovered as shaft power. The shaft power could assist in driving the compressor. The electricity consumption for refrigeration would be reduced by about 10 percent; Tesla prototype is going to be used for this application.

4.2 2D model developed in EES

A 2D thermo-fluid dynamic model was developed in Engineering Equation Solver [67]. Each procedure is thus explained.

4.2.1 Nozzle Profile

Nozzle profile was modeled using an EES code developed in [68] which takes into account a NACA 2412 profile.

This code needs the following input data:

1. Internal and external radius
2. Height of nozzle channel (H_s)
3. Number of discretization sections (N)

Considering a reference system with origin in the external radius of the stator and with a radially directed abscissa, at each subdivision of the stator is assigned its own component $Ax[i]$ and the adjacent component have a distance between them equal to d.

$$d = \frac{R_{in} - R_{out}}{N} , \quad Ax[i] = Ax[i - 1] + d \quad (4.5)$$

In the following list there are the main geometric parameters of the nozzle

1. $r[i]$ is the distance between the i-section and stator's center

$$r[i] = R_{in} - Ax[i] \quad (4.6)$$

2. $u[i]$ is the up line function

$$u[i] = \frac{5}{3} \cdot t_u \cdot ch_u \cdot \left(a_u \cdot \left(\frac{Ax[i]}{ch_u} \right)^2 + b_u \cdot \left(\frac{Ax[i]}{ch_u} \right)^3 + c_u \cdot \left(\frac{Ax[i]}{ch_u} \right)^4 \right) + u[0] \quad (4.7)$$

3. $b[i]$ is the bottom line function

$$b[i] = \frac{5}{3} \cdot t_b \cdot ch_n \cdot \left(a_b \cdot \left(\frac{Ax[i]}{ch_b} \right)^2 + b_b \cdot \left(\frac{Ax[i]}{ch_b} \right)^3 + c_b \cdot \left(\frac{Ax[i]}{ch_b} \right)^4 \right) + u[0] \quad (4.8)$$

4. $ubm[i]$ is the mean line function

$$ubm[i] = \frac{u[i] + b[i]}{2} \quad (4.9)$$

As we can see, there are many parameters to define, they describe the profile and if one of them is changed the profile is different.

$$\begin{aligned} a_u &= 0,10 & b_u &= 0,17 & c_u &= 0,19 & t_u &= 0,1 & ch_u &= 12,5 \\ a_b &= 0,10 & b_b &= 0,17 & c_b &= 0,19 & t_b &= 0,1 & ch_b &= 12,5 \end{aligned}$$

Functions described by Eqs. (4.7) and (4.8) are optimized just for an internal and an external radius, so every analysis is going to be conducted considering this boundary condition; R_{in} and R_{out} are:

$R_{in}=125$ mm

$R_{out}=100$ mm

The only way to vary this bound is changing parameters above but would be taken into account another profile.

Thermodynamic conditions depend by flow passage sections which are perpendicular to the mean line of the profile. So to define them, it's necessary to calculate angular coefficient of each section through Eq.(4.10) and then the perpendicular direction using Eq.(4.11)

$$m[i] = \frac{5}{6} \cdot t_u \cdot ch_u \cdot \left(2 \cdot a_u \cdot \frac{Ax[i]}{ch_u} + 3 \cdot b_u \cdot \left(\frac{Ax[i]}{ch_u} \right)^2 + 4 \cdot c_u \cdot \left(\frac{Ax[i]}{ch_u} \right)^3 \right) + \frac{5}{6} \cdot t_b \cdot ch_b \\ \cdot \left(2 \cdot a_b \cdot \frac{Ax[i]}{ch_b} + 3 \cdot b_b \cdot \left(\frac{Ax[i]}{ch_b} \right)^2 + 4 \cdot c_b \cdot \left(\frac{Ax[i]}{ch_b} \right)^3 \right) \quad (4.10)$$

$$m_{perp} = -\frac{1}{m[i]} \quad (4.11)$$

Every passage section is defined projecting the vertical area (A_v) along perpendicular direction

$$A_v = (u[i] - b[i]) \cdot H_s \quad (4.12)$$

$$A[i] = (u[i] - b[i]) \cdot H_s \cdot \sin(\arctan(m_{perp})) \quad (4.13)$$

Once these variables have been defined, others important nozzle's geometric parameters can be calculated:

1. $\alpha[i]$ is the flow angle of i-section

$$\alpha[i] = \arctan(m[i]) \quad (4.14)$$

2. $r[i]$ is the distance between the i-section and stator's center, this equation changes $r[i]$ calculated in eq. (4.6) because it adds $b[i]$

$$r[i] = \sqrt{(R_{in} - Ax[i])^2 + (b[i])^2} \quad (4.15)$$

3. $chord[i]$ is the distance between two consecutive point belonging to mean line

$$CHORD[i] = \sqrt{(d)^2 + (ubm[i] - ubm[i-1])^2} \quad (4.16)$$

Every section's parameters is built using equations above with Repeat-Until loop that end when the following control isn't satisfied anymore:

$$R[i-1] < R_{out}$$

In Fig. 4.8 there's a plot of the profile where we can see that $A[i]$ decreases when $u[i]$ and $b[i]$ are closer.

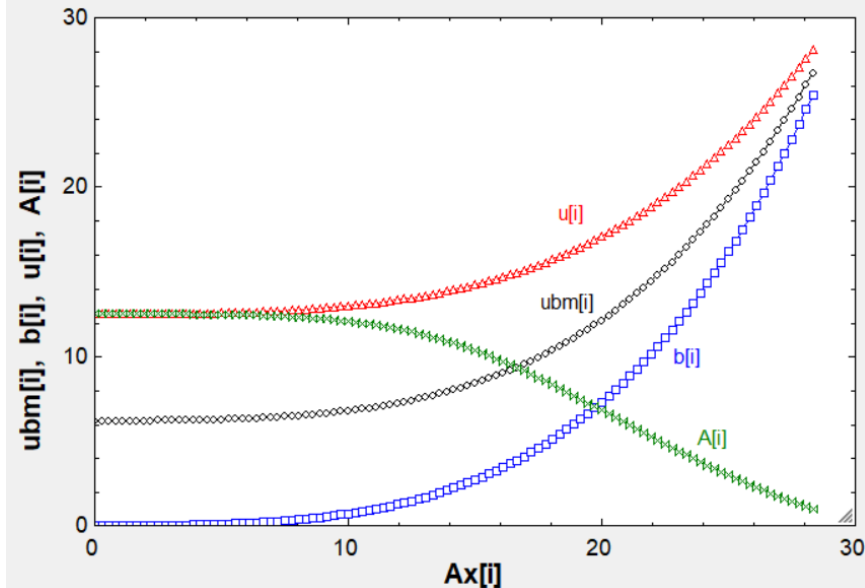


Fig. 4.8 Plot of the profile

4.2.2 Stator model

As the most original component of a Tesla turbine is the bladeless rotor, simple nozzles are commonly used instead of properly designed stator vanes. The Tesla turbine stator purpose is to generate the necessary tangential flow stream at rotor inlet and to convert the pressure energy of the flow in the plenum chamber to kinetic energy at nozzles output. The reduction of cross-sectional area for a subsonic flow produces a favorable pressure gradient and an acceleration of the fluid [69], avoiding wall separation; as a result, the efficiency of nozzles is usually very high, often exceeding 96% [70], [71]. Anyway, for small size nozzles, where the throat width is lower than 3 mm (as is the case for Tesla turbine), the boundary layer might occupy a significant portion of the cross-sectional area [72], generating increased viscous losses. In these cases, the flow is laminar ($Re < 105$) and the total pressure losses decrease with increasing the Reynolds number [72]. As discussed in several papers [73], [74], [75], [76], [77], the stator is commonly acknowledged to be one of the critical components of the Tesla turbine. It is indeed recognized among the main reasons for the low efficiency of the machine obtained in several experimental tests, as it is the source of high total pressure losses. Specifically, Guha and Smiley [76] carried out an experimental and computational study of the Tesla turbine nozzles and concluded that the stator is responsible for total pressure losses up to 35% of the total inlet conditions. In order to carry out a parametric analysis, a set of geometric and thermodynamic parameters needs to be defined. The formers: are stator blade angles, number of nozzles, height of the channel and nozzle geometry profile; which allow the definition of the full geometry (in particular the throat width and the chord length). The main thermodynamic conditions to be fixed when we take into account a two-phase flow are the inlet total pressure and temperature, the mass flow rate and the total inlet quality.

Two-phase main equations

Before showing the main equations, it's important to take into account that the model is about a two-phase flow, so others variables describing this kind of flow must be introduced. A very important parameter for a two-phase fluid is the void fraction, that is the fraction between the area occupied by gas-phase and that occupied by the whole flow.

$$\varepsilon = \frac{A_g}{A_g + A_l} = \frac{1}{1 + \left(\frac{1-x}{x}\right) * \left(\frac{\rho_g}{\rho_l}\right)^{2/3}} \quad (4.17)$$

Other fluid variables are calculated in a different way from a single-phase flow, like viscosity (eq. (4.18)) and sound speed (eq.(4.19))

$$\mu_{TP} = \frac{1}{2} \left[\mu_l \frac{2\mu_l + \mu_g - 2(\mu_l - \mu_g)x}{2\mu_l + \mu_g + (\mu_l - \mu_g)x} + \mu_g \frac{2\mu_g + \mu_l - 2(\mu_g - \mu_l)(1-x)}{2\mu_g + \mu_l + (\mu_g - \mu_l)(1-x)} \right] \quad (4.18)$$

$$SS_{TP} = \left[\frac{\varepsilon}{SS_g^2} + \frac{(1-\varepsilon)^2}{SS_l^2} + \epsilon \cdot (1-\varepsilon) \cdot \frac{\rho_l}{1,35 \cdot P_0} \right]^{-0,5} \quad (4.19)$$

Stator main equations

The thermo-fluid dynamic model for the calculation of the fluid behavior into the Tesla turbine stator assumes real fluid Equations of State (EoS). For this reason, all the thermodynamic properties were evaluated as functions of couples of local variables (typically, p and T) using the Engineering Equation Solver (EES) EoS library data. The thermodynamic of point 00 is defined from input values p_{00} and T_{00} . Point 0 is defined through iteration on density (first guess value is ρ_{00}) and application of mass flow rate definition in order to find v_0 . According to the quality, an “if loop” chooses to use single-phase’s or two-phase’s equations.

$$\dot{m} = \rho_0 \cdot A_0 \cdot v_0 \quad (4.20)$$

Once point 0 is defined, the following procedure and equations are applied to stator profile discretized in N section. Basically, a two phase pressure drop formula has been applied to every section. First of all, it has been used a separated flow model, which means that speed of gas and liquid phase are assumed different.

$$V_g = \frac{\dot{m}_{tot}}{A * \rho_g} \frac{x}{\varepsilon} \quad (4.21)$$

$$V_l = \frac{\dot{m}_{tot}}{A * \rho_l} \frac{1 - x}{1 - \varepsilon} \quad (4.22)$$

In the separated model, the Lockhart – Martinelli parameter (χ) needs to be introduced (25).

$$\chi^2 = \left(\frac{1 - x}{x} \right)^{1,8} \left(\frac{\rho_g}{\rho_l} \right) \left(\frac{\mu_l}{\mu_g} \right)^{0,2} \quad (4.23)$$

The Lockart – Martinelli parameter has been used by Chisholm in order to correlate the friction pressure gradient during the flow of gas-liquid or vapour-liquid mixtures in pipes. The proposed two-phase frictional multiplier for liquid (Eq. (4.25))and gas (Eq. (4.24)) were thus introduced.

$$\Phi_g^2 = \Phi_l^2 * \chi \quad (4.24)$$

$$\Phi_l^2 = 1 + \frac{C}{\chi} + \frac{1}{\chi^2} \quad (4.25)$$

Where:

C is the Chilsom parameter which values depends on each phase regime, as tabulated in Tab 4.1.

Liquid	Gas	c
Turbulent	Turbulent	20
Laminar	Turbulent	12
Turbulent	Laminar	10
Laminar	Laminar	5

Tab 4.1 Chilsom parameter

The phase regime is evaluated with Reynolds number of liquid and gas phase, so the hydraulic diameter of each phase has to be defined.

$A_l = A(1 - \varepsilon)$ is the section covered by the liquid phase and $A_g = A\varepsilon$ is the section covered by the gas phase. The flow type modulus for the liquid phase (α) ables to calculate the hydraulic diameter for liquid phase

$$\alpha_l = (1 - \varepsilon)^4 \Phi_l^{0,98} \quad (4.26)$$

$$A_l = \alpha_l \left(\frac{\pi}{4} D_l^2 \right) \rightarrow D_l = \sqrt{\frac{4A_l(1-\varepsilon)}{\alpha_l \pi}} \quad (4.27)$$

In a similar way, the hydraulic diameter for gas phase is calculated

$$\alpha_g = (1-\varepsilon)^4 \phi_l^{0.38} \quad (4.28)$$

$$A_g = \alpha_g \left(\frac{\pi}{4} D_g^2 \right) \rightarrow D_g = \sqrt{\frac{4A_g \varepsilon}{\alpha_g \pi}} \quad (4.29)$$

So Reynolds number of each phase can be defined and Chilsom parameter too

$$Re_l = \frac{\rho_l * v_l * D_l}{\mu_l} \quad (4.30)$$

$$Re_g = \frac{\rho_g * v_g * D_g}{\mu_g} \quad (4.31)$$

Liquid pressure gradient is defined through liquid friction factor f_l , the total friction pressure drop is found with the frictional multiplier

$$f_l = 2 \left[\left(\frac{8}{Re_l} \right)^{12} + \frac{1}{(a_m + b_m)^{\frac{3}{2}}} \right]^{\frac{1}{12}} \quad (4.32)$$

Where:

$$a_m = \left[2.457 \ln \left(\frac{1}{\left(\frac{7}{Re_l} \right)^{0.9} + \left(0.27 \epsilon / D_l \right)} \right)^{16} \right] \quad (4.33)$$

$$b_m = \left(\frac{37530}{Re_l} \right)^{16} \quad (4.34)$$

Now it's possible finding liquid (Eq. (4.35)) and friction (Eq. (4.36)) pressure gradient

$$\left(\frac{dp}{dl} \right)_{liquid} = \frac{2f_l \rho_l V^2 l}{D_l} \quad (4.35)$$

$$\left(\frac{dp}{dl}\right)_{friction} = \Phi_l^2 \left(\frac{dp}{dl}\right)_{liquid} \quad (4.36)$$

The pressure drop caused by friction is used in the Navier-Stokes equation of momentum along the camber line (Eq.(4.37)), so the infinitesimal dl is the chord of each section

$$p_i + \frac{1}{2} \rho_i v_i^2 = p_{i-1} + \frac{1}{2} \rho_{i-1} v_{i-1}^2 - chord_i \left(\frac{dp}{dl}\right)_{friction} \quad (4.37)$$

For every section this calculation was made, the hypothesis of isoenthalpic stator allows EES to calculate the others thermodynamic parameters.

Stator efficiency is calculated as:

$$\eta_{st} = \left(\frac{h_{01} - h_1}{h_{01} - h_{1s}} \right) \quad (4.38)$$

4.2.3 Stator-rotor coupling model

Assumptions

When connecting the three-separated developed flow models (stator, rotor and gap pressure losses), the following assumptions were applied:

- Conservation of total enthalpy between the stator outlet and the rotor inlet, because the transformation may be considered adiabatic and without any work transfer.
- Invariable static enthalpy, and consequently constant absolute velocity v_1 , while the flow direction changes during the gap crossing. It means that the pressure losses may be treated like an isenthalpic throttling process into a valve.
- No phase change across the gap, so according to the two-phase model the flow come out from the stator as a two-phase flow yet.

Model characteristic

The stator and rotor models only take into account of the distributed pressure losses inside the components, but they do not consider those concentrated into the stator-rotor gap. The passage of the flow from the throat of the nozzle to the gap first and to the rotor channel later, involve an abrupt cross-section enlargement followed by a contraction and generates large flow pressure losses.

Both loss coefficient (abrupt enlargement and abrupt contraction) were obtained from [78]. In order to take into account two phase effects, an iterative procedure was implemented in EES to compute average values of quality between inlet and outlet sections.

Stator–rotor losses main equations

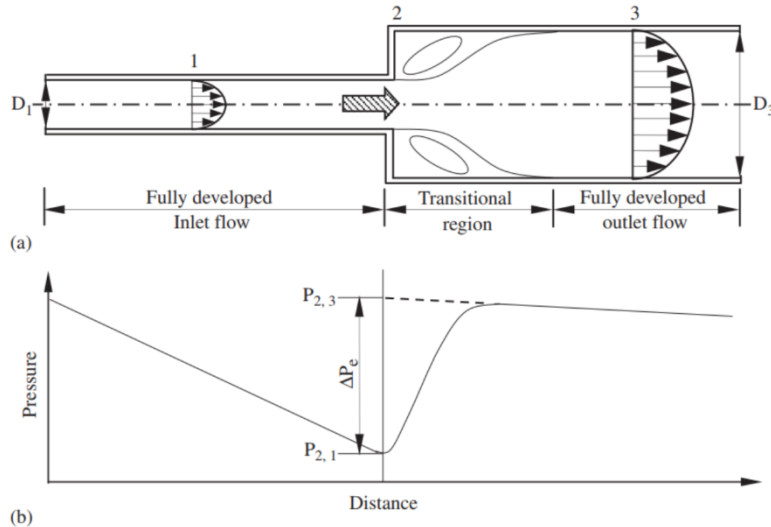


Fig. 4.9 (a) Idealized course of boundary streamlines and (b) pressure profile for a sudden expansion.

Schematic diagrams of the pressure profiles for a sudden expansion and contraction are shown in Fig. 4.9 and Fig. 4.10, respectively. Fig. 4.9 (a) shows the idealized course of the boundary streamlines for the flow through a sudden expansion whereas Fig. 4.9 (b) depicts the graph of the static pressure along the flow axis for a steady flow of a fluid across an expansion.

The total pressure loss across a sudden expansion is explained by the equation (4.39) where σ is the area ratio and the other coefficients are explained by eq. (4.41),(4.42) and (4.43)

$$\Delta P_e = \left(\frac{\dot{m}}{A_{in}} \right)^2 \left(\frac{2\rho_L}{\rho'} \sigma (\sigma - 1) - \rho_h \frac{\rho_L}{(\rho'')^2} (\sigma - 1) \right) \quad (4.39)$$

$$\sigma = \frac{A_{in}}{A_{out}} \quad (4.40)$$

$$\rho' = \left[\frac{1 - x^2}{\rho_L(1 - \varepsilon)} + \frac{x^2}{\rho_G \varepsilon} \right]^{-1} \quad (4.41)$$

$$\rho'' = \left[\frac{(1-x)^3}{\rho_L^2(1-\varepsilon)^2} + \frac{x^3}{\rho_G^2\varepsilon^2} \right]^{-1/2} \quad (4.42)$$

$$\rho_h = \left(\frac{x}{\rho_G} + \frac{1-x}{\rho_L} \right)^{-1} \quad (4.43)$$

Where A_{in} is the throat cross section, here having rectangular shape:

$$A_{in} = Z_s \cdot H_s \cdot TW \quad (4.44)$$

Due to this expression of A_{in} , \dot{m} is the total flow rate, this is taken into account for the A_{out} expression too.

A_{out} is the cross section on the disks (transversal) covered by the flow jet:

$$A_{out} = \left\{ \frac{\left[\frac{TW}{\tan(\alpha_1)} + \frac{G}{\sin(\alpha_1)} \right]}{\cos \alpha_1} - G \cdot \tan(\alpha_1) - \frac{G}{\tan(\alpha_1)} \right\} \cdot H_s \cdot Z_s \quad (4.45)$$

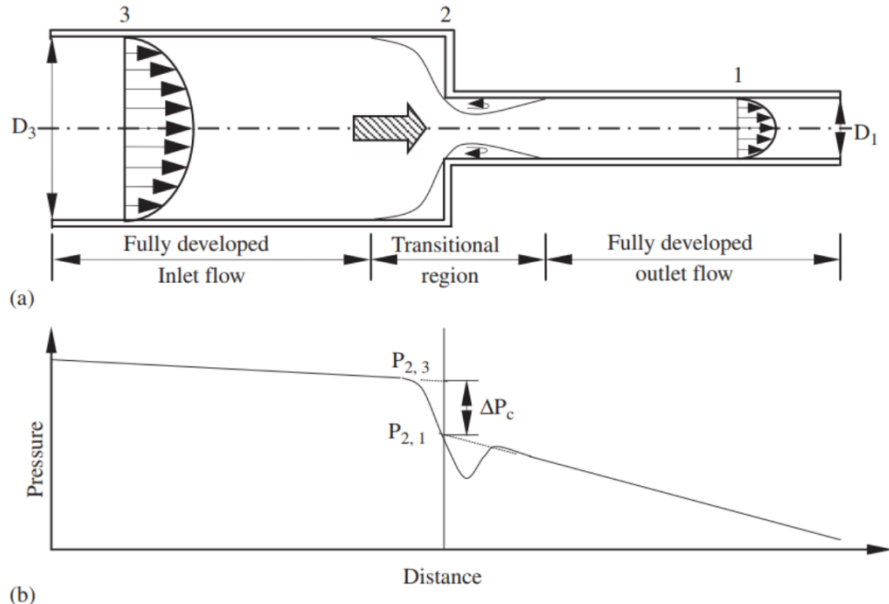


Fig. 4.10 (a) Idealized course of boundary streamlines and (b) pressure profile for a sudden contraction.

Fig. 4.10(a) shows the boundary streamlines for the flow through a sudden contraction whereas Fig. 4.10(b) depicts the graph of the static pressure along the flow axis for a steady flow of a fluid across a contraction.

The total pressure loss across a sudden contraction is explained by the equation (4.47) where σ is the area ratio, $\rho', \rho'', \bar{\rho}_h$ are two-phase coefficients explained by eq. (4.41),(4.42) and (4.43); C_c is the contraction coefficient.

$$\Delta P_c = \frac{\dot{m}^2}{A_{in}} \left\{ \frac{\bar{\rho}_h}{2} \left(\frac{1}{C_c^2 \rho_{2,1}''^2} - \frac{\sigma^2}{\rho_3''^2} \right) + \left(\frac{1}{\rho_1'} - \frac{C_c}{\rho_{2,1}'} \right) \right\} \quad (4.46)$$

$\bar{\rho}_h$ should use the average values between point 2 and point C (vena contracta point), but point 2,C and 1 have been approximated and joined at the same point so the equation takes into account just values at outlet. For the same reason the $\rho_{2,1}''$ and $\rho_{2,1}'$ become ρ_1'' and ρ_1' and equation (4.46) is approximated as the following:

$$\Delta P_c = \frac{\dot{m}^2}{A_{in}} \left\{ \frac{\rho_h}{2} \left(\frac{1}{C_c^2 \rho_1''^2} - \frac{\sigma^2}{\rho_3''^2} \right) + \left(\frac{1 - C_c}{\rho_1'} \right) \right\} \quad (4.47)$$

The above and other models which are based on the vena-contracta phenomenon, generally assume that for a particular system the vena-contracta in single-phase and two-phase flows take place in the same location, and result in identical contraction ratio, C_c . Consequently, C_c is usually found from single-phase flow data, a correlation given by [79] gives eq. (4.48):

$$C_c = 1 - \frac{1 - \sigma}{2.08(1 - \sigma) + 0.5371} \quad (4.48)$$

The areas taken into account for sudden contraction are A_{in} which is the cylindrical surface that takes into account H_s as height and A_{out} which is the inlet cylindrical surface of the rotor that takes into account the space between disks (b)

$$A_{in} = 2\pi r_2 \cdot H_s \cdot n_pack \quad (4.49)$$

$$A_{out} = 2\pi r_2 \cdot b \cdot n_ch \quad (4.50)$$

4.2.4 Rotor model

The first developed model for the rotor flow was derived from [80], [81] applying some remarkable improvements. The variable density and the other thermodynamic functions were taken as fluid properties, depending on the local variables (for example pressure and temperature). As for the stator model, the fluid properties were locally evaluated using EES EoS library data and two-phase's equations . The assumptions of steady, laminar and two-dimensional flow were kept, as

well as the viscous forces treated as body forces acting on the flow at each position [81]. It allowed simplifying and thus numerically solving the fundamental Navier–Stokes equations, expressed in cylindrical coordinates.

The shear stress in a two-phase flow can be expressed using a homogeneous or a separated model, in this section they are both explained but it has been used just the separated one.

Assumptions

In order to develop a sound analytical model, the following assumptions have been made:

- a) Steady flow regime;
- b) The viscous force is treated as a body force acting on the flow at each ($r - \theta$) position;
- c) Two-dimensional flow:
 - $V_z = 0$;
 - $V_r = \text{constant across the channel}$
 - $V_\theta = \text{constant across the channel}$
- d) Radial symmetric flow field, uniform at the inlet ($r = r_0$). The flow field is thus the same for any θ , therefore the derivative $\partial / \partial \theta = 0$ for all flow variables;
- e) $(\partial p / \partial \theta)$ negligible compared to wall friction forces

Taking into account the previous assumptions, the fundamental Navier-Stokes equations in cylindrical coordinates are reduced to:

- Continuity

$$\frac{1}{r} \frac{\partial(r\rho_{TP}V_{r,TP})}{\partial r} = 0 \quad (4.51)$$

$$r\rho_{TP}V_{r,TP} = \text{cost} \quad (4.52)$$

- Momentum, r -direction

$$V_{r,TP} \frac{\partial V_{r,TP}}{\partial r} - \frac{V_{\theta,TP}^2}{r} = -\frac{1}{\rho_{TP}} \left(\frac{\partial p}{\partial r} \right)_{TP} + f_{r,TP} \quad (4.53)$$

- Momentum, θ -direction

$$V_{r,TP} \frac{\partial V_{\theta,TP}}{\partial r} + \frac{V_{r,TP}V_{\theta,TP}}{r} = f_{\theta,TP} \quad (4.54)$$

- Momentum, z -direction

$$-\frac{1}{\rho_{TP}} \left(\frac{\partial p}{\partial z} \right)_{TP} = 0 \quad (4.55)$$

Knowing the mass flow rate inside each channel, it follows that locally:

$$V_{r,TP} = -\frac{\dot{m}_{tot}}{2\pi rb\rho_{TP}} \quad (4.56)$$

Considering a fluid element between the two disks defining the flow channel, a control volume Q_e can be defined with base surface A_e and height b . The fluid wetted area is $A_w = 2A_e$. Therefore, the hydraulic diameter D_h is equal to $2b$.

Consequently,

$$A_e = \frac{Q_e}{b} = \frac{2Q_e}{D_h} \quad A_w = \frac{4Q_e}{D_h}$$

The formulation of the viscous shear stress can be obtained through two different path, which takes into account the two-phase flow as a homogeneous flow, or which conversely distinct the two-phases.

Homogeneous flow model

Introducing the two-phase homogeneous model ($w_l = w_g = w$) ([82], [83]), the shear stress can be written as eq. (4.57)

$$\tau_w = \frac{f_{TP}\rho_{TP}}{2}w^2 = \frac{f_{TP}\rho_{TP}}{2}[(V_\theta - \omega r)^2 + V_r^2] \quad (4.57)$$

Where:

$U = \omega r = \frac{U_o}{r_o}r$ is the peripheral speed;

$\rho_{TP} = \left(\frac{x}{\rho_g} + \frac{1-x}{\rho_l}\right)^{-1}$ is the two-phase density of the fluid;

$Re_{TP} = \frac{\rho_{TP}wD_h}{\mu_{TP}}$ is the two-phase Reynolds number;

The two phase friction factor can be computed through Churchill correlation, differently from eq. (4.32), it takes into account a two phase Reynolds number and the entire hydraulic diameter.

$$f_{TP} = 2 \left[\left(\frac{8}{Re_{TP}} \right)^{12} + \frac{1}{(A + B)^{3/2}} \right]^{1/12} \quad (4.58)$$

Where:

$$A = \left[2.457 \ln \left(\frac{1}{\left(\frac{7}{Re_{TP}} \right)^{0.9} + \left(0.27\epsilon/D_h \right)} \right) \right]^{16} \quad (4.59)$$

$$B = \left(\frac{37530}{Re_{TP}} \right)^{16} \quad (4.60)$$

The force resulting from wall friction force is given by the product of the wall shear with the wetted area $\tau_w * A_w = F_{TP}$:

$$F_{TP} = \frac{f_{TP}\rho_{TP}}{2}[(V_\theta - \omega r)^2 + V_r^2] * \frac{4Q_e}{D_h} \quad (4.61)$$

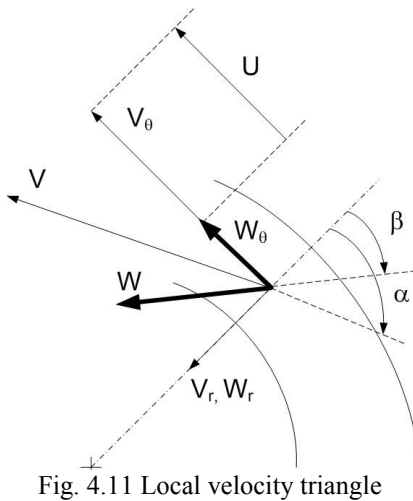


Fig. 4.11 Local velocity triangle

The radial and tangential component of the force are given by:

$$F_r = F \cos(\beta) \quad (4.62)$$

$$F_\theta = -F \sin(\beta) \quad (4.63)$$

Where β is the angle between relative velocity and the radial direction. The value of $\cos \beta$ and of $\sin \beta$ can thus be calculated as:

$$\cos \beta = \frac{V_r}{\sqrt{[(V_\theta - \omega r)^2 + V_r^2]}} \quad (4.64)$$

$$\sin \beta = \frac{(V_\theta - \omega r)}{\sqrt{[(V_\theta - \omega r)^2 + V_r^2]}} \quad (4.65)$$

Substituting (4.65) and (4.64) in (4.63) and (4.62), a compact expression of the radial and tangential forces components are obtained:

$$F_{r,TP} = F_{TP} \cos \beta = \frac{f_{TP} \rho_{TP}}{2} [(V_\theta - \omega r)^2 + V_r^2] \frac{4Q_e}{D_h} \cos \beta = \frac{f_{TP} \rho_{TP}}{2} \frac{4Q_e}{D_h} \sqrt{[(V_\theta - \omega r)^2 + V_r^2]} V_r \quad (4.66)$$

$$F_{\theta,TP} = -F_{TP} \sin \beta = -\frac{f_{TP} \rho_{TP}}{2} * \frac{4Q_e}{D_h} * (V_\theta - \omega r) * \sqrt{[(V_\theta - \omega r)^2 + V_r^2]} \quad (4.67)$$

Dividing (4.66) and (4.67) by the mass of the fluid element between two disks, the body force term in the radial and tangential direction can be expressed as:

$$f_{r,TP} = \frac{f_{TP}}{2} * \frac{4}{D_h} * \sqrt{[(V_\theta - \omega r)^2 + V_r^2]} * V_r \quad (4.68)$$

$$f_{\theta,TP} = -\frac{f_{TP}}{2} * \frac{4}{D_h} * (V_\theta - \omega r) * \sqrt{(V_\theta - \omega r)^2 + V_r^2} \quad (4.69)$$

In order to determine the local pressure and the local derivative $(\partial V_r)/\partial r$, (4.68) and (4.69) are substituted in (4.53) and (4.54):

$$V_r \left(-\frac{V_r}{r} \right) - \frac{V_\theta^2}{r} = -\frac{1}{\rho_{TP}} \left(\frac{\partial p}{\partial r} \right)_{TP} + \frac{f_{TP}}{2} * \frac{4}{D_h} * \sqrt{[(V_\theta - \omega r)^2 + V_r^2]} * V_r \quad (4.70)$$

$$V_r \left(\frac{\partial V_\theta}{\partial r} \right)_{TP} + \frac{V_r V_\theta}{r} = -\frac{f_{TP}}{2} * \frac{4}{D_h} * (V_\theta - \omega r) * \sqrt{(V_\theta - \omega r)^2 + V_r^2} \quad (4.71)$$

From the top equation the pressure gradient in radial direction is obtained (eq. (4.72)), from the bottom equation the tangential velocity is defined (eq. (4.73)).

$$\left(\frac{\partial p}{\partial r} \right)_{TP} = \frac{\rho_{TP} V_\theta^2}{r} + \frac{\rho_{TP} V_r^2}{r} + \frac{2\rho_{TP} f_{TP}}{D_h} * \sqrt{[(V_\theta - \omega r)^2 + V_r^2]} * V_r \quad (4.72)$$

$$\left(\frac{\partial V_\theta}{\partial r} \right)_{TP} = -\frac{2f_{TP}}{D_h} * \frac{(V_\theta - \omega r)}{V_r} * \sqrt{(V_\theta - \omega r)^2 + V_r^2} - \frac{V_\theta}{r} \quad (4.73)$$

Separated flow model

Same procedure is followed for the separated flow model. Considering the flow-type modulus for liquid (eq.(4.26)), it is possible to define the radial velocities of each phase (eqs.(4.21),(4.22)), considering that $A = 2\pi r b$ is the investigated section, $A_l = A(1 - \varepsilon)$ is the section covered by the liquid phase and $A_g = A\varepsilon$ is the section covered by the gas phase. Moreover Eq. (4.74) define the hydraulic diameter of the liquid phase.

$$A_l = \alpha \left(\frac{\pi}{4} D_l^2 \right) \rightarrow D_l = \sqrt{\frac{8rb(1-\varepsilon)}{\alpha}} \quad (4.74)$$

In relative coordinates equations (4.21) and (4.22) can be expressed as:

$$w_g = \frac{V_g}{\cos(\beta)} \quad (4.75)$$

$$w_l = \frac{V_l}{\cos(\beta)} \quad (4.76)$$

The same procedure used for the stator able to calculate liquid and frictional pressure drop.

The shear stress can therefore be expressed through eq. (4.77) and eq.(4.78).

$$\tau_w \frac{A}{P} = \left(\frac{dp}{dl} \right)_{friction} \quad (4.77)$$

$$\frac{A}{P} = \frac{D_h}{4} \quad (4.78)$$

Rearranging (4.36) and (4.77), we can obtain:

$$\tau_w = \frac{D_h}{4} * \Phi_l^2 \left(\frac{dp}{dl} \right)_{liquid} \quad (4.79)$$

Once obtained the expression of the shear stress, the same procedure as the homogeneous flow model is utilized. Therefore, a compact expression of the radial and tangential force components are here also obtained:

$$F_{r,TP} = F_{TP} * \cos \beta = \Phi_l^2 \left(\frac{\partial p}{\partial l} \right)_{liquid} * \frac{D_h}{4} * \frac{4Q_e}{D_h} * \frac{V_{r,TP}}{\sqrt{[(V_{\theta,TP} - \omega r)^2 + V_{r,TP}^2]}} \quad (4.80)$$

$$F_{\theta,TP} = -F_{TP} \sin \beta = -\Phi_l^2 \left(\frac{\partial p}{\partial l} \right)_{liquid} * \frac{D_h}{4} * \frac{4Q_e}{D_h} * \frac{(V_{\theta,TP} - \omega r)}{\sqrt{(V_{\theta,TP} - \omega r)^2 + V_{r,TP}^2}} \quad (4.81)$$

Dividing (4.80) and (4.81) by the mass of the fluid element between two disks, the body force term in the radial and tangential direction can be expressed as:

$$f_{r,TP} = \Phi_l^2 \left(\frac{\partial p}{\partial l} \right)_{liquid} * \frac{1}{\rho_{TP}} * \frac{V_{r,TP}}{\sqrt{[(V_{\theta,TP} - \omega r)^2 + V_{r,TP}^2]}} \quad (4.82)$$

$$f_{\theta,TP} = -\Phi_l^2 \left(\frac{\partial p}{\partial l} \right)_{liquid} * \frac{1}{\rho_{TP}} * \frac{(V_{\theta,TP} - \omega r)}{\sqrt{(V_{\theta,TP} - \omega r)^2 + V_{r,TP}^2}} \quad (4.83)$$

In order to determine the local pressure and the local derivative $(\partial V_r)/\partial r$, equations (4.82) and (4.83) are substituted in (4.53) and (4.54):

$$-V_{r,TP} \frac{V_{r,TP}}{r} - \frac{V_{\theta,TP}^2}{r} = -\frac{1}{\rho_{TP}} \left(\frac{\partial p}{\partial r} \right)_{TP} + \Phi_l^2 \left(\frac{\partial p}{\partial l} \right)_{liquid} * \frac{1}{\rho_{TP}} * \frac{V_{r,TP}}{\sqrt{[(V_{\theta,TP} - \omega r)^2 + V_{r,TP}^2]}} \quad (4.84)$$

$$V_{r,TP} \frac{\partial V_{\theta,TP}}{\partial r} + \frac{V_{r,TP} V_{\theta,TP}}{r} = -\Phi_l^2 \left(\frac{\partial p}{\partial l} \right)_{liquid} * \frac{1}{\rho_{TP}} * \frac{(V_{\theta,TP} - \omega r)}{\sqrt{[(V_{\theta,TP} - \omega r)^2 + V_{r,TP}^2]}} \quad (4.85)$$

From the top equation the pressure gradient in radial direction is obtained (4.86), from the bottom equation the tangential velocity is defined (4.87).

$$\left(\frac{\partial p}{\partial r} \right)_{TP} = \rho_{TP} \frac{V_{r,TP}^2 + V_{\theta,TP}^2}{r} + \Phi_l^2 \left(\frac{\partial p}{\partial l} \right)_{liquid} * \frac{V_{r,TP}}{\sqrt{[(V_{\theta,TP} - \omega r)^2 + V_{r,TP}^2]}} \quad (4.86)$$

$$\frac{\partial V_{\theta,TP}}{\partial r} = -\frac{V_{\theta,TP}}{r} - \Phi_l^2 \left(\frac{\partial p}{\partial l} \right)_{liquid} * \frac{1}{\rho_{TP} V_{r,TP}} * \frac{(V_{\theta,TP} - \omega r)}{\sqrt{[(V_{\theta,TP} - \omega r)^2 + V_{r,TP}^2]}} \quad (4.87)$$

Equations (4.86) and (4.87) were implemented in EES environment and numerically solved by applying a step forward method (centered finite difference): the rotor channel was discretized in radial direction with a predefined number of equal steps (NR). Increasing the discretization steps allowed a higher accuracy prediction of the local thermodynamic variables; nonetheless, the increase of accuracy was obtained at the cost of an increased computational time. Therefore, 250 discretization steps were selected, as it was found as a reasonable compromise between accuracy of results and calculation time. This equation set allows the calculation of the local values of pressure and velocity, both in absolute and relative coordinates. Finally, the rothalpy conservation (Eq.(4.88)) was applied to calculate the local value of static enthalpy:

$$h_i = I_2 - \frac{w_i^2}{2} + \frac{u_i^2}{2} \quad (4.88)$$

4.3 Two phase model results

4.3.1 Component analysis

In order to assess the performance potential of the Tesla turbine for organic Rankine cycle applications, several parametric analyses were carried out: the performance parameters were evaluated as functions of the main geometric variables and operating conditions. The R404A was adopted as the working fluid for the investigation of each component influence on the performance of the turbine, because it is the fluid actually present in the test bench of University of Florence. It is expected that in the next months a new prototype will be tested with this fluid. Initially, single variable optimization was carried out, in order to determine the most critical parameters for the Tesla turbine; successively combined parameters optimization was performed, to understand the mutual influence of the most meaningful parameters both on efficiency and power.

4.3.2 Individual variables optimization

In this Section, the influence of each single parameter on the performance of the turbine is analyzed, while keeping constant all the other geometric and thermodynamic parameters. The nozzle profile provides a limit because it has been made “ad hoc” just for the external and inner diameter mentioned in section 4.2.1, so the analysis are made taking into account moreover parameters on which stator diameters have not effect. Every analysis has been made with the same mass flow rate and a Mach number at stator exit around 0,8 was the maximum reached.

Rotor inlet diameter

The rotor inlet diameter is one of the most significant parameters, as it plays a primary role on both the power production and the size of the machine. Once inlet thermodynamic condition, flow rate and geometry are fixed, a higher rotor diameter is associated to a high peripheral velocity. The work output per unit mass of the expander is defined by the Euler equation (4.89).

$$Work = v_{\vartheta 2} u_2 - v_{\vartheta 3} u_3 \quad (4.89)$$

Since both the first and second terms increase with larger rotor diameter (increase in peripheral velocity), the specific work output presents an optimization value, while the overall power output has a monotonically increasing trend. The exit kinetic energy decreases because of the effect of compressibility: the exit velocity is more or less the same, because the outlet diameter of the rotor is the same but a higher inlet diameter leads to a higher pressure drop and a higher quality which leads to a lower density. So, rotor and total efficiencies increase and find an optimal value near the maximum rotor diameter. The following analysis should have stator diameter as a limit but it wasn't taken into account. The same nozzle profile has been considered so the stator thermodynamic conditions are always the same.

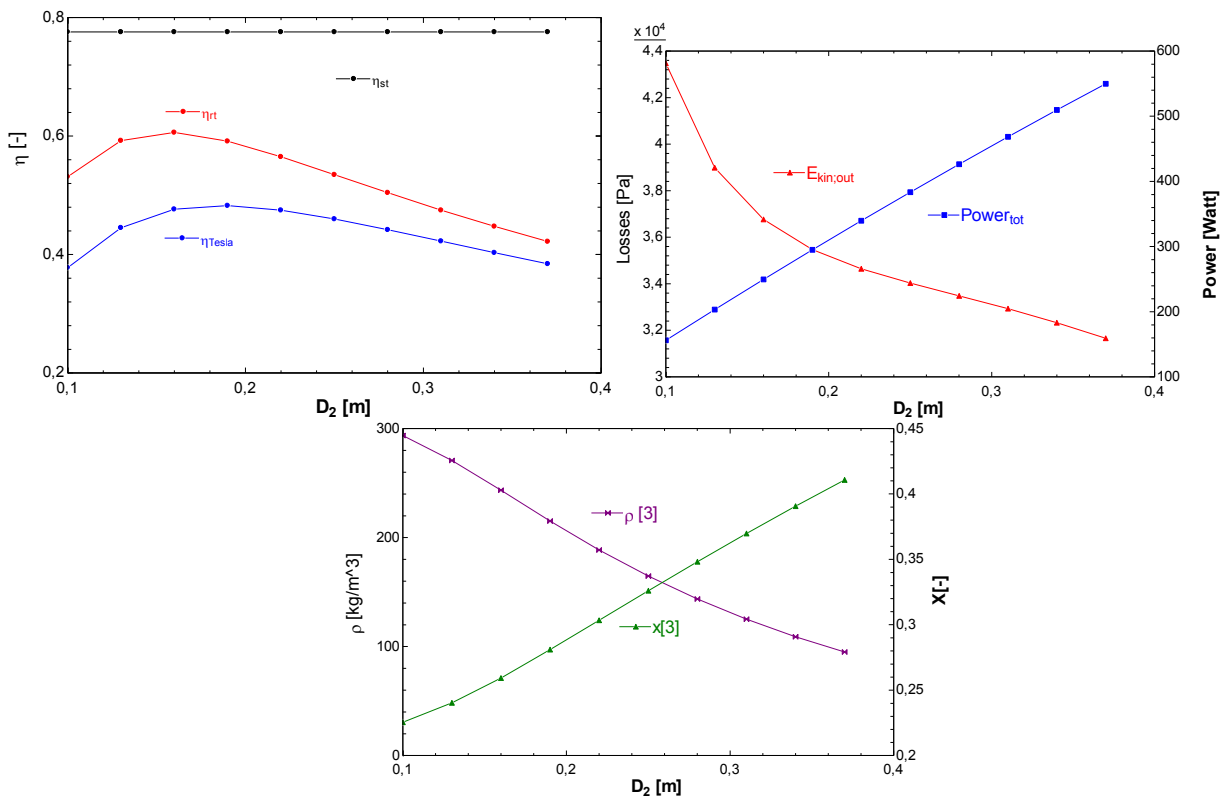
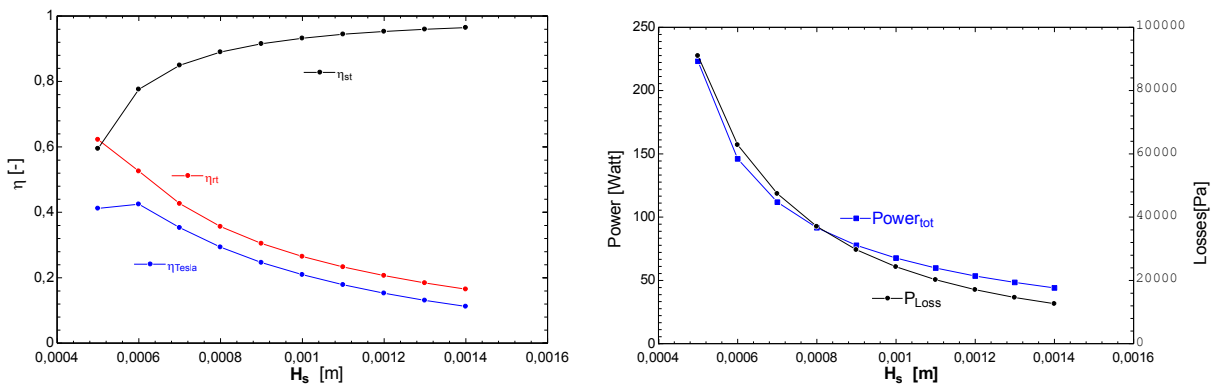
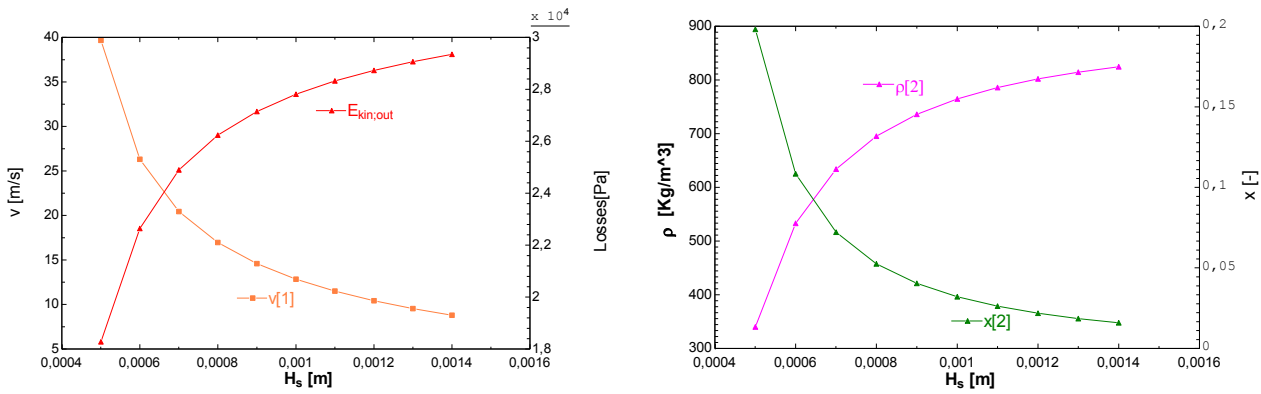


Fig. 4.12 Performance varying rotor inlet diameter

Height of the nozzle section

The height of the nozzle section directly influences the geometry and the variables at the stator output, especially the velocity at stator outlet, which strongly decreases when H_s increases. Decreasing the height of stator outlet area, the continuity equation ensures a reduced outlet velocity and, consequently, a lower quality which leads to a higher and almost constant density at stator outlet. A low-quality fluid provides less power and, opposite to the previous analysis, an increasing exit kinetic energy. So, rotor and total efficiencies decrease while stator efficiency remain almost constant, there's a maximum of total to static efficiency just close to when stator efficiency is very low compared to the other configurations. Moreover, pressure losses in the gap decreases because of an increasing enlargement area.



Fig. 4.13 Performance varying H_s

Number of nozzles

The number of nozzles (Z_{stat}) is another parameter which directly influences the exit velocity of the stator, as the stator height. So, trends are more or less the same of stator height's analysis but rotor and total to static efficiency have a more accentuated decreasing trend. On the other hand, stator exit velocity has a lower decreasing trend because it varies from 20 to 5 m/s while reducing H_s it varies from 40 to 10 m/s.

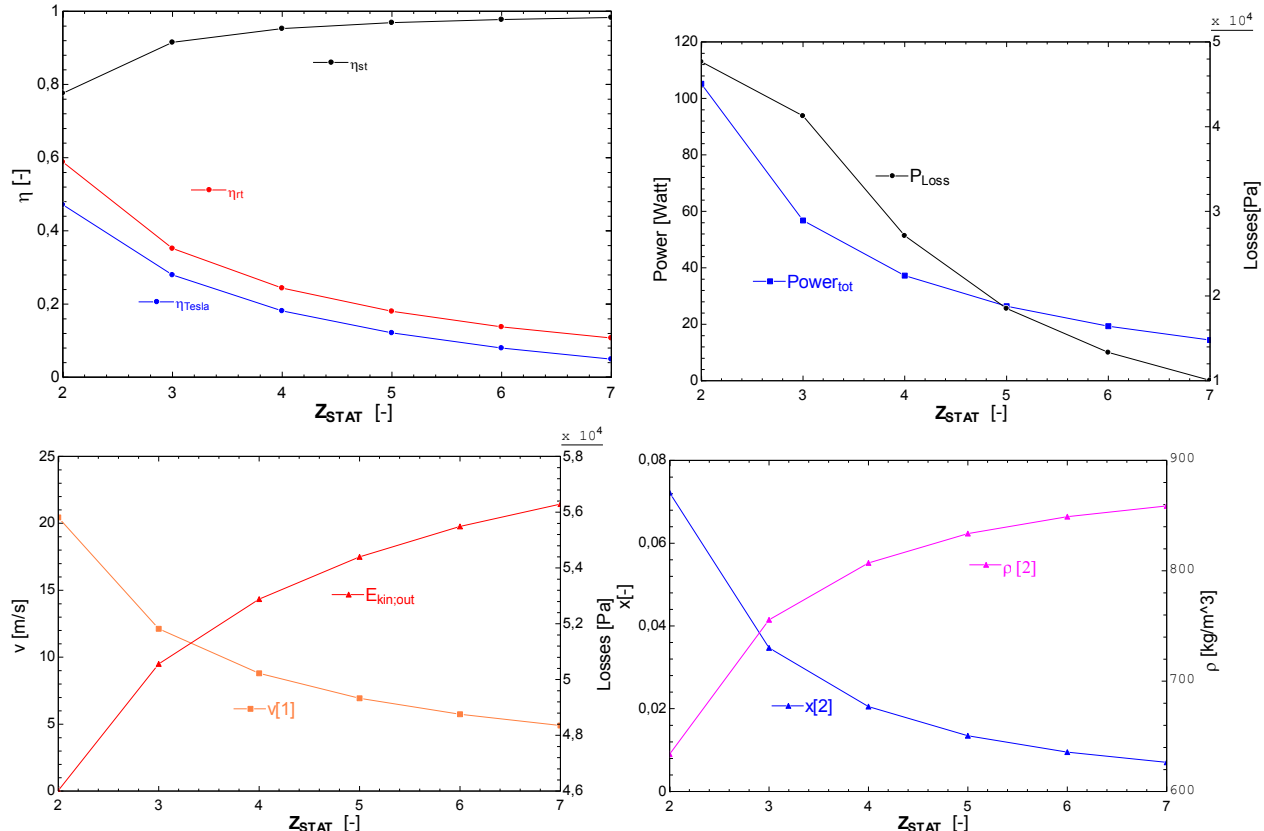


Fig. 4.14 Performance varying number of nozzles

Rotor channel height

The channel height is directly proportional to tangential velocity and inversely proportional to radial velocity. The power increases but not a lot, the configuration of 0,1 mm provides a power 5

Watt lower than the 1 mm one, it means that rotor channel height hasn't a deep impact when the velocity at stator exit is high, this feature is also in the efficiency where it's difficult finding a max. This feature advises to make a rotor channel height as wide as stator channel height for an easier manufacturing. An increasing of b leads to a lower friction which provides a lower exit velocity but also a quality closer to zero. This leads to a decreasing exit kinetic energy because a quality close to zero means there's a fluid almost incompressible and the exit density doesn't change. Pressure losses between stator and rotor are directly linked to contraction so they decrease due to increase of contraction coefficient.

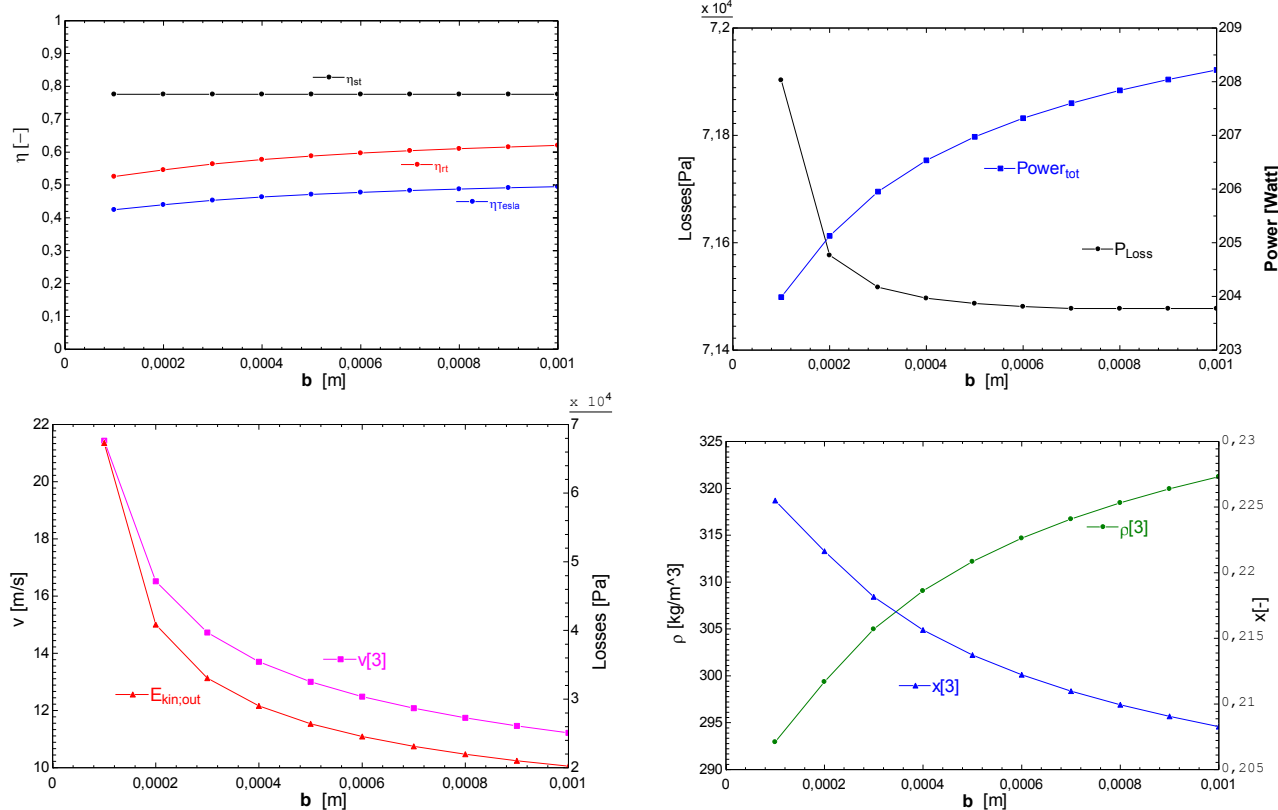


Fig. 4.15 Performance varying rotor channel height

Rotor diameter ratio

The variation of D_3/D_2 presents a significant minimum value of tangential velocity at rotor outlet, as can be deducted from Euler. Similarly, to the previous analysis, the optimizing value of outlet/inlet rotor diameter ratio D_3/D_2 is characterized by the minimum energy loss and, therefore, the maximum turbine efficiency.

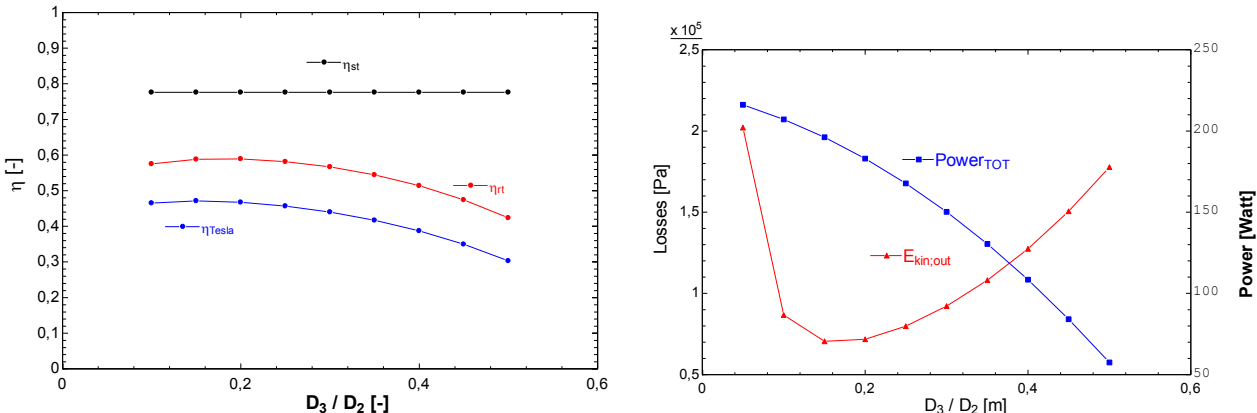


Fig. 4.16 Performance varying rotor diameter ratio

Rotor peripheral speed

The variation of the rotor peripheral speed influences the relative tangential velocity w_{t2} , thus, a value of peripheral speed above which a reversal flow condition is generated exists. At disk exit, the pressure decreases when the rotational speed increases, due to momentum equilibrium in radial direction. Rotational speeds in the range between 2000 and 4000 rpm seemed to guarantee an optimized value of the expander efficiency, as displayed in Fig. 4.17.

The maximum position is mainly characterized by an optimization of tangential velocity ratio ($\sigma = \frac{v_{t2}}{u_2}$) which is going to be discussed in section 4.3.4

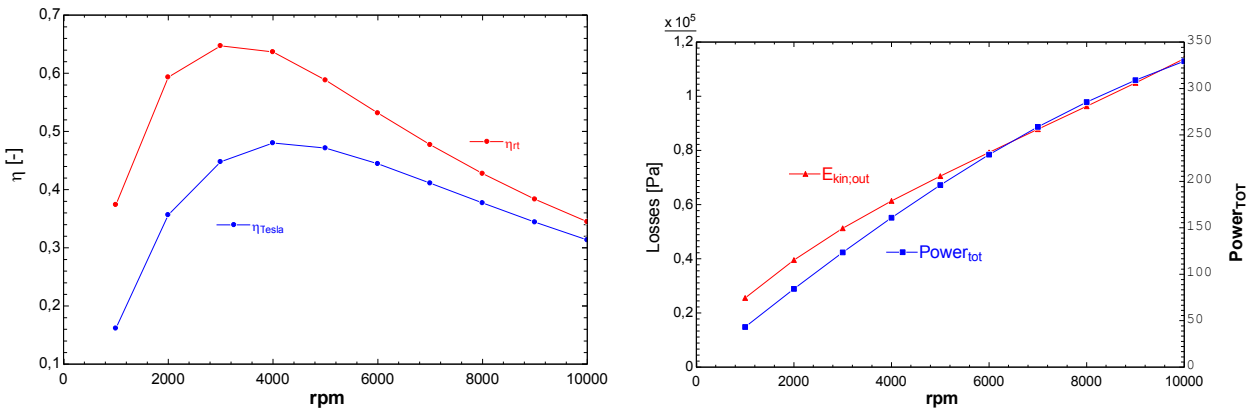


Fig. 4.17 Performance varying rpm

4.3.3 Combined variables

Single parameter optimization is necessary in order to understand the influence of each element on turbine performance, but it is not enough in order to achieve a complete optimization procedure due to the mutual influence of each variable. As reported in Fig. 4.18 , the combined assessment of both inner and outer disk's diameter displays an improvement of the expander efficiency (η) at reduced values of H_s . This trend is directly linked to the reduction of the inner velocity; power output conversely exhibits a similar behavior. Stator height has a very strong influence at low values especially for the efficiency; instead at high stator height the impact of diameter ratio is deeper.

The exit kinetic energy shows a more accentuated increase when D_3/D_2 is higher, this effect is directly linked to the efficiency behavior.

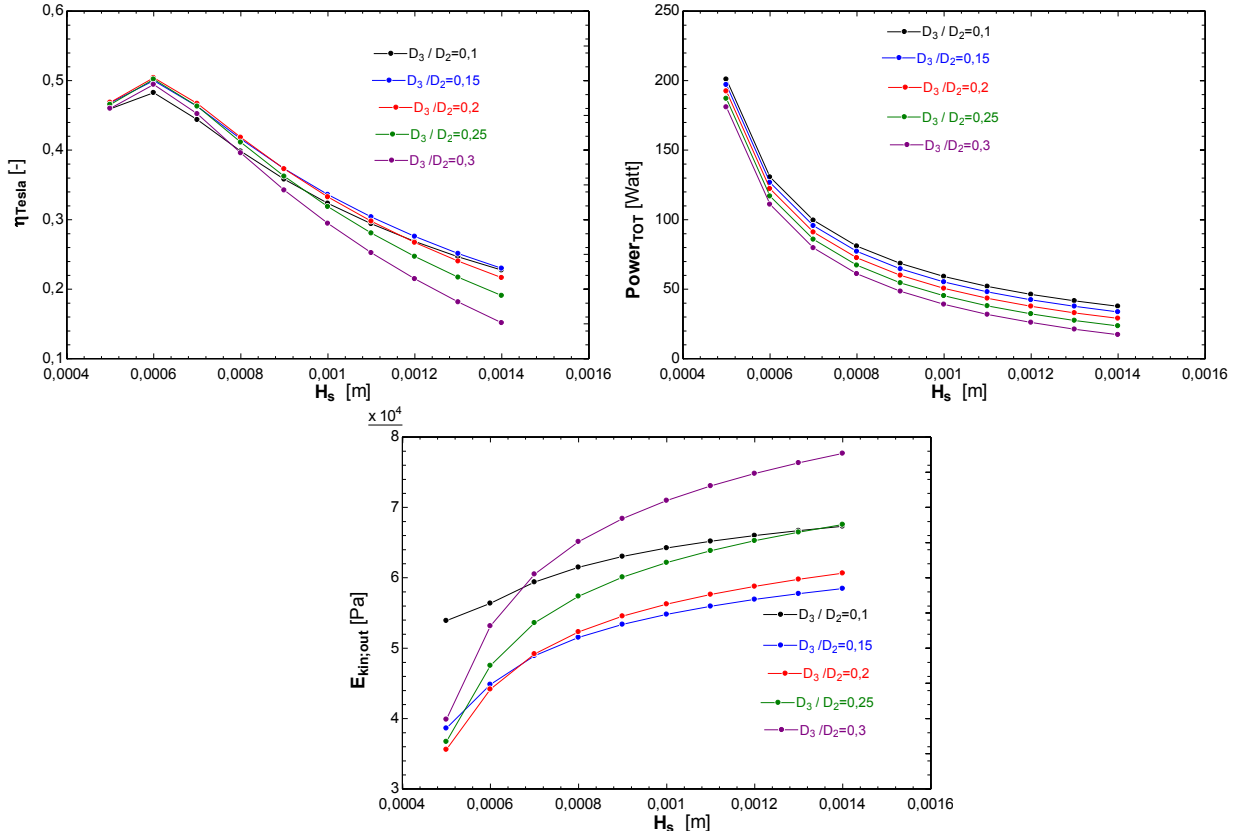
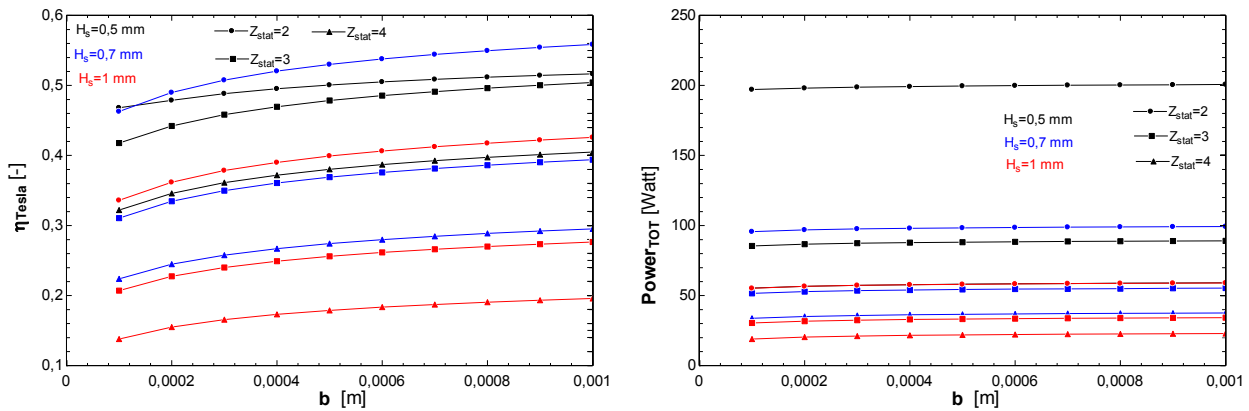
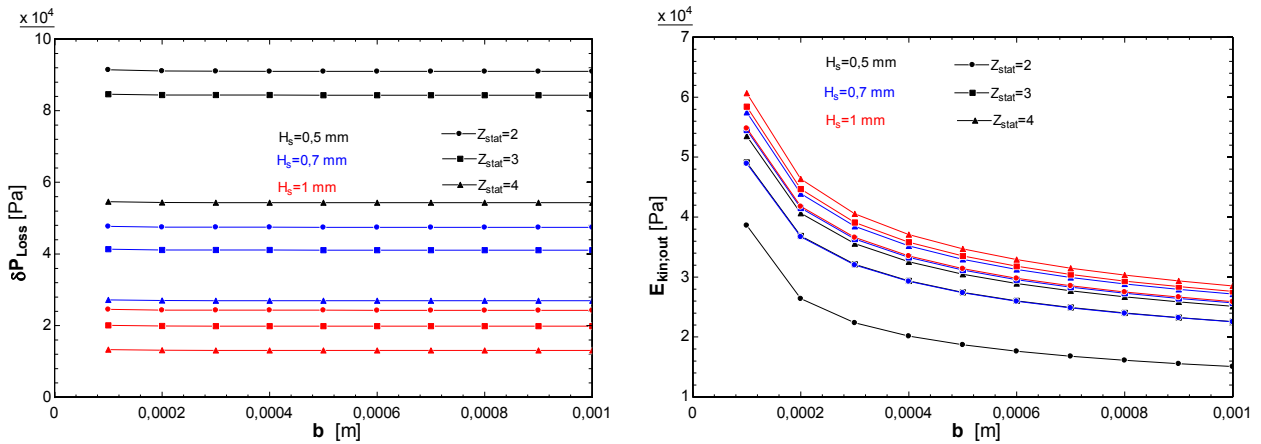


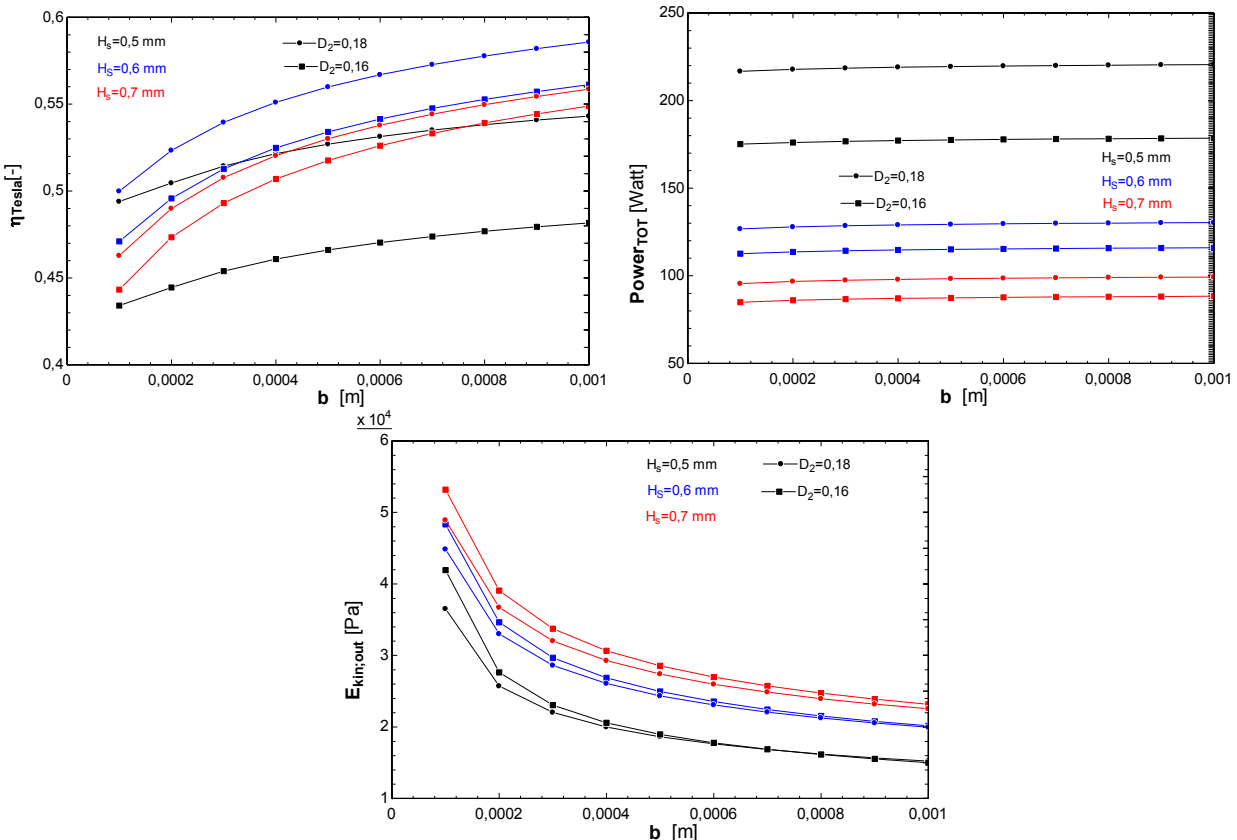
Fig. 4.18 Performance varying H_s combined with the variation of rotor diameter ratio

The number of nozzles (Z_{stat}) is important as well, in the previous section it wasn't clear which parameter was more influent between number of nozzles and stator channel height. When stator efficiency is low (H_s low) the number of nozzles hasn't a big influence because the effect of high velocity at stator exit which provides a good total to static efficiency is balanced by a low stator efficiency compared to a configuration with a wider stator height. The power and also losses have opposite behaviors because they are parameters where speed at stator exit has a key role.



Fig. 4.19 Performance varying rotor channel height combined with the variation of H_s and number of nozzles

A further analysis was carried out varying rotor channel height at different stator height and rotor inner diameter. The increase of rotor diameter and rotor channel height have positive consequence for power and efficiency, but the impact is more and more accentuated if stator height is low. For example, if $H_s=0.5$ mm the differences between two diameters are higher compared to a configuration with a higher H_s and an increase of rotor channel height provides a more accentuated increasing trend (curves has a higher inclination) This feature is directly linked to stator efficiency which obviously influences total to static efficiency, when stator efficiency is more or less constant this effect disappears. The effect provides also to many cross points in the efficiency trend which advices having a stator height characterized by a good efficiency. Exit kinetic energy too is moreover influenced by stator height.

Fig. 4.20 Performance varying rotor channel height combined with the variation of H_s and outlet rotor diameter

Collecting the result of the performed sensitivity analysis guidelines for design of an optimized and balanced Tesla turbine can be drawn; these may be summarized in the following:

- Stator, 2 convergent nozzles with a stator height of 0,6 mm
- Rotor, 10 channels 0,6 mm wide each; 1 disk for every turbine package; external diameter of 0,18 m, disks diameters ratio around 0,15;

4.3.4 Tangential velocity ratio

The tangential velocity ratio ($\sigma = \frac{v_{t2}}{u_2}$) is one of the most important parameters for Tesla turbine optimization. The right matching of rotor inlet tangential velocity and peripheral speed is of paramount importance to achieve a high efficiency. In practice, the efficiency is at its highest at $\sigma = 1$, or very close to 1 (Fig. 4.21). This is due to the right value achieved by the inlet tangential relative velocity in this condition, which is very close to zero. At higher value of σ , the fluid-machine work transfer would not be optimal, as the velocity would drop drastically at rotor inlet, dissipated into heat and not usefully transmitted to the rotor by the viscous forces. On the other hand, if a value lower than 1 is considered, a reversal flow conditions would be triggered. Indeed, if the absolute tangential velocity is lower than the rotational speed, a negative relative tangential velocity would be obtained at rotor inlet, so that the turbine would behave as a compressor at least in that region. Nonetheless, values only little lower than 1, but close to 1 may be considered to achieve high efficiency levels. Indeed, if the flow reversal region is very limited, the higher power produced by the remaining inner region of the rotor, operating at a higher rotational speed, while keeping all other parameters unchanged, counterbalances the negative effect of the flow reversal. Therefore, best values of the tangential velocity ratio σ were found in the range from 0,8 to 0,9.

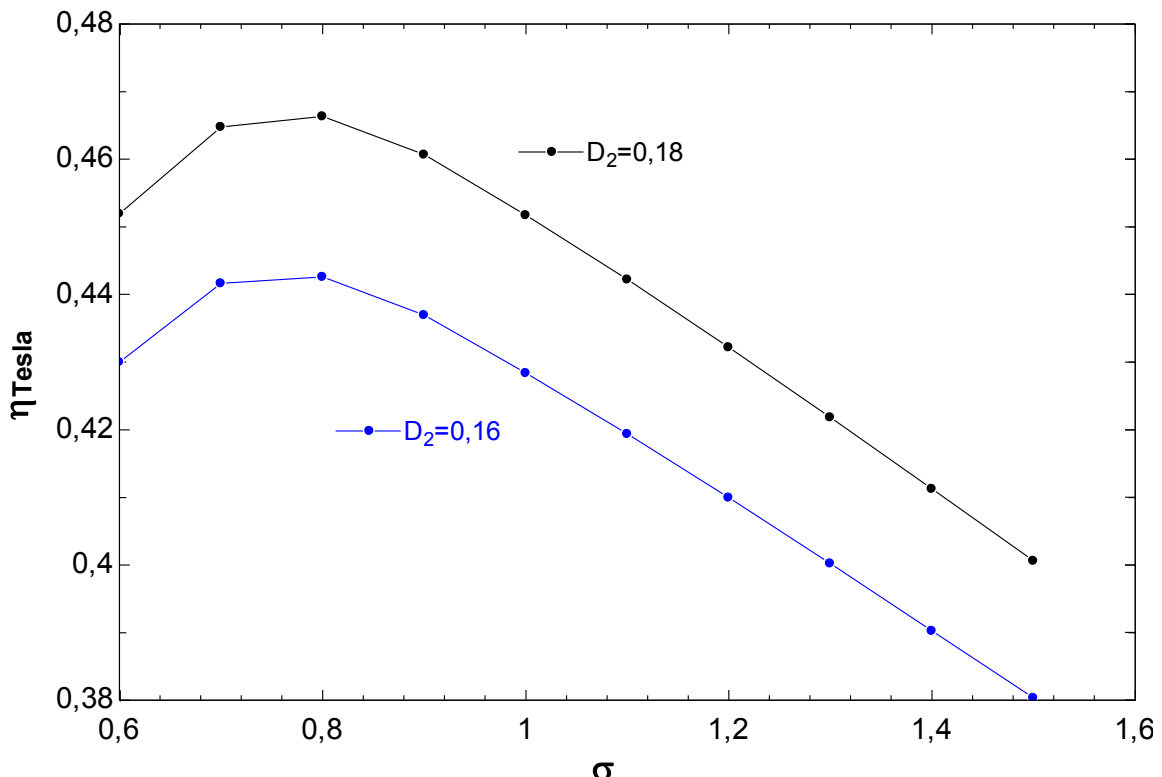


Fig. 4.21 Tangential velocity ratio

4.3.5 Compactness and rotational speed

As discussed in the previous Section, the right matching between inlet tangential velocity in the rotor and rotational speed is of paramount importance to achieve high turbine performances. In order to have the proper match, the rotational speed needs to be adapted to the rotor external diameter. Specifically, the smaller the rotor, the higher the rotational speed required for best efficiency (Fig. 4.22). The machine compactness (i.e. power output per unit volume of the turbine) is another fundamental parameter, depending on the specific requirements of the field of application, and is clearly related to the rotational speed. For example – referring to expanders in the power range from 1 to 30 kW – for the automotive sector, compactness is a fundamental parameter, and therefore a small, fast-turning Tesla turbines would be preferable; on the other hand, for domestic application, the Tesla concept offers – with respect to other possible expanders, such as centripetal turbines – the attractive possibility of direct coupling with a 3000 rpm generator and a low noise emission factor; for these applications compactness of the machine could be sacrificed. However, the rotational speed for two-phase flows is much lower than the one for single-phase flows. The compactness factor CF is the ratio between the power and the total volume of the turbine, expressed in W/m^3 . The turbine's volume should take into account the external radius, having a “profile ad hoc” it has been considered the rotor diameter multiplied by a coefficient which gives an approximate external radius result.

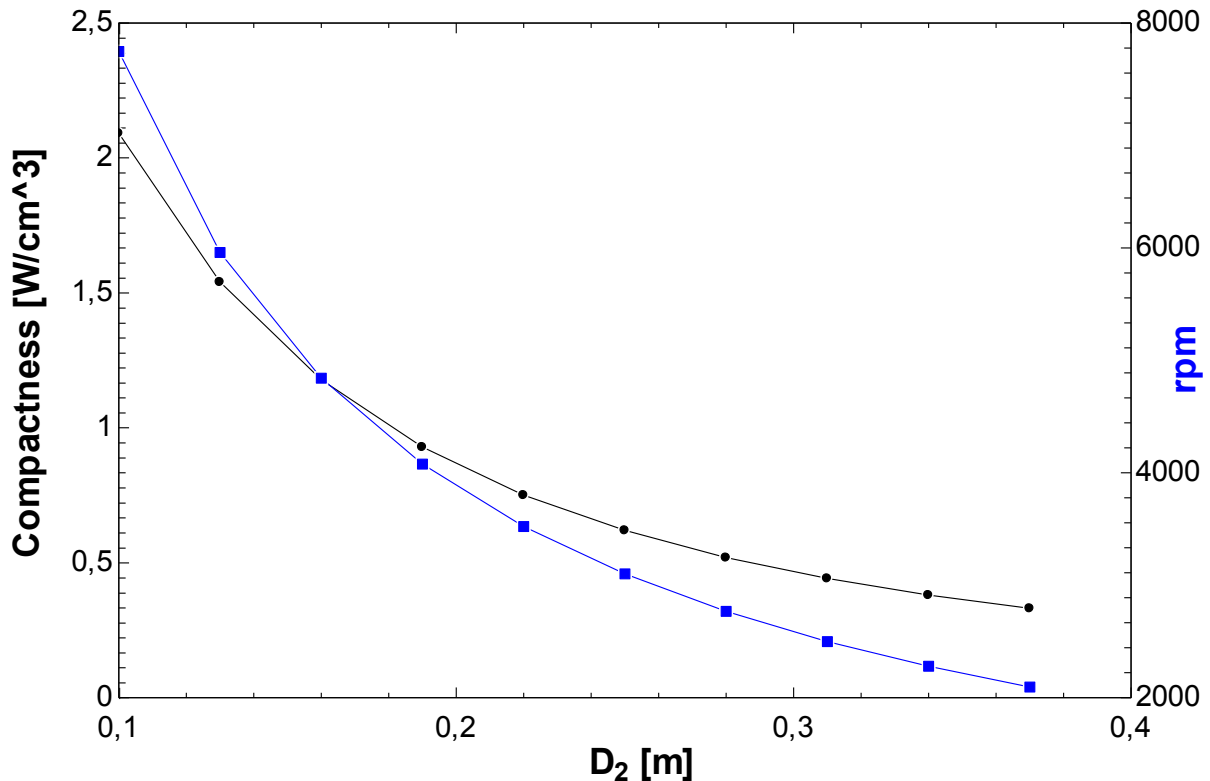


Fig. 4.22 Compactness factor and rotational speed

5 Conclusions and Recommendations

This work belongs to a line of research on small energy system that is growing over the last years, especially taking into account the Organic Rankine Cycle (ORC). In this context small expanders have a key role, but the main issue is that they do not combine the qualities of low costs, efficiency and reliability. In this domain, Tesla turbine seems to be a valuable candidate to tackle these issues, as its simple structure guarantees a low cost and reliable and expander.

This type of radial expander is characterized by the absence of rotor blades, which are replaced by multiple parallel flat disks; a little gap separates the rotor disks from the related stator parts, which consist of one or more tangential nozzles. The working fluid moves from the inlet to the outlet radius due to the difference in pressure determined by friction and by the exchange of momentum, exits from openings made on the disks at the inner radius.

5.1 Conclusions

University of Florence made an ORC prototype that has been tested in University of Liège using R1233zd(E) as working fluid. However, the torque meter used had a big range compared to turbine's torque range, this led to a big error. Because of this problem, a data's repetition was planned with a torque meter characterized by a smaller range. Unfortunately, several problems into the turbine and also Covid-19 didn't allow to conduct test:

- Stator's silicone which forces fluid to flow through the nozzles was melted before tests.
- Connection screws between shaft and rotor were unscrewed and they have unscrewed again during the first tests.

Issues described above have changed thesis objectives and a Matlab code to reduce data was performed, to judge its reliability we used data of the previous experimental campaign. First of all, the code links data acquired by Labview and collected in an Excel file to Matlab; then the Reconciliation method is applied. This method makes a data oscillation around the standard deviation allowed by the instrument and finds solutions which respects the energy balance with a very small error. Results using data of the previous experimental campaign showed that the method reduces errors in energy balance and sometimes the efficiency varies of 5 % compared to results using mean values of a configuration. This led to limit data oscillation when it's too high also if the oscillation is allowed by instrument range. The highest thermodynamic power production was 907 W and it has been reached with a flow rate of 0,3 kg/s and a superheating level above 40°C. A thermodynamic condition with a higher mass flow rate and a lower superheating level produces the same expansion ratio but a lower power, this means that a lower flow rate and a high superheating level enables a better match between tangential velocity and rotational speed. Thermodynamic power shows a monotonically increasing trend both with expansion ratio and with rotational speed. However ,shaft power trend has a parabolic trend especially for high flow rate due to mechanical losses that grows with flow rate and rotational speed, the highest shaft power production was 371 W. Thermodynamic and shaft efficiency's trend are directly related respectively to thermodynamic and shaft power, thermodynamic efficiency reached was 24% and the shaft efficiency reached was 11%. These low values of efficiencies are due to mechanical but also fluid dynamic losses , especially flow blockage due to the throttling effects of disks edges, windage between end disks and the case and pumping losses. These losses are higher at high expansion ratio and to limit them the prototype is going to be modified taking of the thinner disks, in order to facilitate flow entrance into rotor disks. This new prototype is going to be used for a two-phase flow, especially for a refrigeration cycle substituting the lamination valve. So, the second section of this work is dedicated to a code performed in EES about a two-phase flow in a Tesla turbine. The code takes into account

a NACA profile for nozzles, then stator and rotor are solved in a similar way, using a separated flow model. Compared to others models in literatures that take into account a single-phase flow in a Tesla turbine, a different approach has been used especially for the stator that has been discretized in sections like rotor instead of be solved with correlations that take into account only the first and the last section. This approach allows to simulate better a two-phase flow in a turbine's component which influences a lot its performance like the stator. Indeed, results showed that the main variables which influences Tesla performances is the stator exit velocity; when a geometric parameter provides a high velocity (nozzle's channel height for example), rotor's parameters have an influence lower and lower. The analysis conducted provides the following optimization parameters: 2 convergent nozzles with a stator height of 0,6 mm, 10 rotor channels 0,6 mm wide each, 1 disk for every turbine package, external rotor diameter of 0,18 m and disks diameters ratio around 0,15.

5.2 Recommendations

This work has taken into account both experimental and numerical research about a Tesla turbine, so they are both type of recommendations:

- The ORC prototype made by University of Florence needs a maintenance, especially screws that connect the shaft to the rotor due to high temperatures and torque to which they are subjected during tests.
- Apply the Reconciliation method to others experimental campaigns and make a comparison between experimental data and numerical model.
- Improve two-phase model, especially the nozzle profile's section which is made "ad hoc" just for an inner and an outlet stator's diameter, in order to simulate the model in a wider range of diameters
- Simulate more working fluids with the two-phase model instead of just R404a and then make a geometry assessment for each fluid
- Make a simulation exploring a wide range of thermodynamic conditions
- Perform an experimental campaign on two-phase Tesla turbines

Bibliography

- [1] M. E., "Theoretical basis of the Organic Rankine Cycle," in *Organic Rankine Cycle (ORC) Power Systems, Technologies and*, 1 Edition ed., Woodhead Publishing, Elsevier.
- [2] "Knowledge Center for Organic Rankine Cycle, History of ORC," [Online]. Available: <http://www.korc.org/en/science-technology/history/>. [Accessed 25 May 2018].
- [3] A. M. Tari  re T., "A Word Overview of the Organic Rankine Cycle Market," *Energy Procedia*, no. 129, pp. 2-9, 2017.
- [4] B. L.Y., "History of Organic Rankine Cycle systems," in *Organic Rankine Cycle (ORC) Power Systems, Technologies and Applications*, 1 ed., Woodhead Publishing, Elsevier.
- [5] I. P. S. P. Invernizzi C., "Bottoming micro-Rankine cycles for micro-gas turbines," *Appl. Therm. Eng.*, no. 27, pp. 100-110, 2007.
- [6] S. D. M. J. S. T. Chacartegui R., "Alternative ORC bottoming cycles for combined cycle power plants," *Appl. Energy*, no. 86, p. 2162–2170, 2009.
- [7] D. I. H. F. Al-Sulaiman F.A., "Exergy analysis of an integrated solid oxide fuel cell and organic Rankine cycle for cooling, heating and power production," *J. Power Sources*, no. 195, p. 2346–2354, 2010.
- [8] G. A. Vaja I., "Internal Combustion Engine (ICE) bottoming with Organic Rankine Cycles (ORCs)," *Energy*, no. 35, p. 1084–1093, 2010.
- [9] B. J. L. L. S. J. Bonilla J.J., "Technological recovery potential of waste heat in the industry of the Basque country," *Appl. Therm. Eng.*, no. 17, p. 283–288, 1997.
- [10] G. S. V. D. B. M. L. V. Q. S. Desideri A., "Experimental comparison of organic fluids for low temperature ORC (organic Rankine cycle) systems for waste heat recovery applications," *Energy*, no. 97, p. 460–469, 2016.
- [11] K. S. K. E. S. H. Schuster A., "Energetic and economic investigation of Organic Rankine Cycle applications," *Appl. Therm. Eng.*, no. 29, p. 1809–1817, 2009.
- [12] D. Y. W. J. W. R. Zhai H., "Energy and exergy analyses on a novel hybrid solar heating, cooling and power generation system for remote areas," *Appl. Energy*, no. 86, p. 1395–1404, 2009.
- [13] A. R. Lentz A., "Solar-geothermal hybrid system," *Appl. Therm. Eng.*, no. 26, p. 1537–1544, 2006.
- [14] B. D. Heberle F., "Exergy based fluid selection for a geothermal Organic Rankine Cycle for combined heat and power generation," *Appl. Therm. Eng.*, no. 30, p. 1326–1332, 2006.
- [15] M. G. R. E. T. L. Fiaschi D., "Exergoeconomic analysis and comparison between ORC and Kalina cycles to exploit low and medium-temperature heat from two geothermal sites," *Energy Conversion and Management*, no. 154, pp. 503-516, 2017.
- [16] L. H. R. S. Dong L.L., "Development of small-scale and micro-scale biomass-fuelled CHP systems – a literature review," *Appl. Therm. Eng.*, no. 29, p. 2119–2126, 2009.
- [17] L. H. R. S. Qiu G., "Expanders for micro-CHP systems with organic Rankine cycle," *Appl. Therm. Eng.*, no. 31, p. 3301–3307, 2011.
- [18] L. G. F. A. P. G. Tchanche B.F., "Low-grade heat conversion into power using organic Rankine cycles – a review of various applications," *Renew. Sust. Energy Rev.*, no. 5, p. 3963–

3979, 2011.

- [19] M. G. F. D. Tempesti D., "Thermodynamic analysis of two micro CHP systems operating with geothermal and solar energy," *Appl. Energy*, no. 97, p. 609–617, 2012.
- [20] I. C. G. M. Bombarda P., "Performance analysis of OTEC plants with multilevel Organic Rankine Cycle and solar hybridization," *ASME J. Eng. Gas Turbines Power*, no. 135, 2013.
- [21] K. S. Braimakis K., "Integrated thermoeconomic optimization of standard and regenerative ORC for different heat source types and capacities," *Energy*, no. 121, p. 570–598, 2017.
- [22] L. A. B. E. Manente G., "Design guidelines for the choice between single and dual pressure layouts in organic Rankine cycle (ORC) systems," *Energy*, no. 123, p. 413–431, 2017.
- [23] R. F. M. Y. Shokati N., "Exergoeconomic analysis and optimization of basic, dual-pressure and dual-fluid ORCs and Kalina geothermal power plants: A comparative study," *Renewable Energy*, no. 83, p. 527–542, 2015.
- [24] P. S. K. K. Lee H.Y., "Comparative analysis of thermodynamic performance and optimization of organic flash cycle (OFC) and organic Rankine cycle (ORC)," *Appl. Therm. Eng*, no. 100, p. 680–690, 2016.
- [25] Z. C. H. X. Li X., "Thermodynamic analysis of Organic Rankine Cycle with Ejector," *Energy*, no. 42, p. 342–349, 2012.
- [26] H. Y. N. Z. C. Y. L. X. Chen J., "Performance analysis of a novel organic Rankine cycle with a vapor–liquid ejector," *Energy Conversion and Management*, no. 157, pp. 382-395, 2018.
- [27] H. M. S. J. P. M. N. A. B. K. Palacz M., "A gas ejector for CO₂ supercritical cycles," *Energy*, no. 163, p. 1207–1216, 2018.
- [28] C. X. M. N. Y. Y. S. S. Zhang K., "Evaluation of ejector performance for an organic Rankine cycle combined power and cooling system," *Appl. Energy*, no. 184, p. 404–412, 2016.
- [29] M. A. Z. V. M. S. R. M. Yari M., "Exergoeconomic comparison of TLC (trilateral Rankine cycle), ORC (organic Rankine cycle) and Kalina cycle using a low grade heat source," *Energy*, no. 83, p. 712–722, 2015.
- [30] A. D. L. S. M. E. Astolfi M., "Comparison between ORC and CO₂ power systems for the exploitation of low–medium temperature heat sources," *Energy*, no. 161, p. 1250–1261, 2018.
- [31] C. E. T. C. M. T. L. J. T. A. Colonna P., "Organic Rankine Cycle Power Systems: From the Concept to Current Technology, Applications, and an Outlook to the Future," *J. of Engineering for Gas Turbines and Power*, no. 137, pp. 1-19, 2015.
- [32] Z. L. Bao J., "A review of working fluid and expander selections for Organic Rankine Cycle," *Renewable and Sustainable Energy Reviews*, no. 24, p. 325–342, 2013.
- [33] Q. G, "Selection of working fluids for micro–CHP systems with ORC," *Renewable Energy*, no. 48, p. 565–570, 2012.
- [34] V. D. B. M. D. S. D. P. L. V. Quoilin S., "Technoeconomic survey of Organic Rankine Cycle (ORC) systems," *Renewable and Sustainable Energy Reviews*, no. 22, pp. 168-186, 2013.
- [35] L. X. P. H. L. L. T. L. Wang D., "Efficiency and optimal performance evaluation of organic Rankine cycle for low grade heat power generation," *Energy*, no. 50, p. 343–352, 2013.
- [36] L. G. Talluri L., "Simulation and Design Tool for ORC Axial Turbine stage," *Energy Procedia*, no. 129, p. 277–284, 2017.
- [37] M. G. M. F. Fiaschi D., "Thermo–fluid dynamics preliminary design of turbo–expanders for ORC cycles," *Appl. Energy*, no. 97, p. 601–608, 2012.
- [38] M. G. M. F. Fiaschi D., "Design and performance prediction of radial ORC turboexpanders," *Appl. Energy*, no. 138, p. 517–532, 2014.
- [39] I. G. M. G. M. F. Fiaschi D., "Design of micro radial turboexpanders for ORC power cycles: From 0D to 3D," *Appl. Therm. Eng*, no. 99, p. 402–410, 2016.

- [40] K. G. K. P. K. P. Garg P., "Development of a generic tool to design scroll expanders for ORC applications," *Appl. Therm. Eng.*, no. 109, p. 878–888, 2016.
- [41] Q. S. C. C. L. J. Lemort V., "Testing and modeling a scroll expander integrated into and Organic Rankine Cycle," *Appl. Therm. Eng.*, no. 29, p. 3094–3102, 2009.
- [42] V. D. B. M. D. P. M. Ziviani D., "Geometry-Based Modeling of Single-Screw Expander for Organic Rankine Cycle Systems in Low-Grade Heat Recovery," *Energy Procedia*, no. 61, p. 100–103, 2014.
- [43] D. P. A. P. A. Branchini L., "Systematic comparison of ORC configurations by means of comprehensive performance indexes," *Appl. Therm. Eng.*, no. 61, p. 129–140, 2013.
- [44] D. S. L. A. G. L. L. V. Quoilin S., "Working fluid selection and operating maps for Organic Rankine Cycle expansion machines," *International Compressor Engineering Conference proceedings*, no. 1546, p. 1–10, 2012.
- [45] L. A. Lemort V., "Positive displacement expanders for Organic Rankine Cycle systems," in *Organic Rankine Cycle (ORC) Power Systems, Technologies and Applications*, 1 ed., Woodhead Publishing, Elsevier.
- [46] G. L. L. A. D. A. Q. S. Lemort V., "A comparison of piston, screw and scroll expanders for small-scale Rankine cycle systems," *Proceedings of the 3rd International Conference on Microgeneration and Related Technologies*, 2013.
- [47] D. S. Q. S. Lemort V., "Experimental characterization of a hermetic scroll expander for use in a micro-scale Rankine cycle," *Proceedings of the Institution of Mechanical Engineers, Part A: Journal of Power and Energy*, no. 226, p. 126–136, 2012.
- [48] W. Y. X. G. M. C. J. W. L. S. Y. K. Y. F. Zhang Y.Q., "Development and experimental study on organic Rankine cycle system with single-screw expander for waste heat recovery from exhaust of diesel engine," *Energy*, no. 77, p. 499–508, 2014.
- [49] K. T. I. E. Zywica G., "A review of expanders for power generation in small-scale organic Rankine cycle systems: Performance and operational aspects," *Proc. IMechE Part A: J. Power and Energy*, no. 230, p. 669–684, 2016.
- [50] L. Preetham B.S. Weiss, "Investigations of a new free piston expander engine cycle," *Energy*, no. 106, p. 535–545, 2016.
- [51] Y. M. M. L. Haiqing G., "Some design features of CO₂ swing piston expander," *Appl. Therm. Eng.*, no. 26, p. 237–243, 2006.
- [52] T. N, "Turbine," *U.S. Patent*, 1913.
- [53] D. F. G. N. L. C. L. Talluri, "Design and optimization of a Tesla turbine for ORC applications," *Applied Energy*, no. 226, pp. 300-319, 2018.
- [54] K. e. al., "Computer Control II Mathematics of control," *Chem. Eng. Prog.*, no. 57, pp. 44-47, 1967.
- [55] H. e. al., "A hierarchical procedure for adjustment and material balancing of mineral processed data," *Int. J. Miner.*, no. 7, pp. 91-116, 1980.
- [56] R. e. a. Weiss, "Data reconciliation – an industrial case study," *Comput. Chem. Eng.*, no. 20, pp. 1441-1449, 1996.
- [57] H. e. al., "Methodology for optimization of operation to reduce site-scale energy use in production plants," *Appl. Therm. Eng.*, no. 17, pp. 1005-1014, 1997.
- [58] P. e. al., "Industrial application of data reconciliation," *Comput. Chem. Eng.*, no. 22, pp. 1035- S11038, 1998.
- [59] S. e. al., "Soft sensors based on nonlinear steady-state data reconciliation in the process industry," *Chem. Eng. Process.*, no. 46, pp. 320-331, 2006.
- [60] L. e. al., "Data reconciliation and optimal operation of a catalytic naphtha reformer," *J. Process.*

- Control*, no. 18, pp. 320-331, 2008.
- [61] B. e. al., "Hybrid solar/gas Single/Double effect absorption chiller : Operational results using data reconciliation," in *Proceedings of the 2nd International Conference on Solar Air-conditionning*, Tarragona, Spain, 2007.
- [62] M. e. al., "Steady-state data reconciliation for absorption refrigeration system," *App. Therm. Eng.*, pp. 1170-1180, 2013.
- [63] S. e. al., "An optimization of redundant measurements location or thermal capacity of power unit steam boiler calculations using data reconciliation method," *Energy*, no. 92, p. 135–141, 2015.
- [64] J. e. al., "Data reconciliation based framework for integrated sensor and equipment performance monitoring in power plants," *Appl.Therm. En.*, no. 134, pp. 270-282, 2014.
- [65] Cuevas, "Contribution to the modelling of refrigeration systems," *Phd Thesis*, 2006.
- [66] D. G. Elliott, "Theory and tests of two-phase turbines," Pasadena, California, 1982.
- [67] N. G. Klein S.A., "Mastering EES," *f-Chart software*, 2012.
- [68] M. M., "Progettazione dello statore di una turbina Tesla che opera con flusso bifase," 2020.
- [69] Anderson, Fundamentals of aerodynamics, 3 ed., New York: McGraw Hill, 2001.
- [70] Sheperd, Principles of turbomachinery, 2 ed., New York: The Macmillan Company, 1956.
- [71] Shames, Mechanics of fluids, 4 ed., New York: McGraw–Hill Professional, 2002.
- [72] R. Y. C. V. Butenko V.A., "Experimental investigation of the characteristics of small–sized nozzles," *Fluid Dyn.*, no. 11, p. 936–939, 1976.
- [73] A. J.H, "An Investigation of the Performance of a Modified Tesla Turbine," 1952.
- [74] R. W, "An analytical and experimental investigation of multiple–disk turbines," *ASME Journal of Engineering for Power*, no. 87, p. 29–36, 1965.
- [75] G. A. Hoya G.P., "The design of a test rig and study of the performance and efficiency of a Tesla disc turbine," *Proc. IMechE, Part A: J. Power and Energy*, no. 223, p. 451–465, 2009.
- [76] S. B. Guha A., "Experiment and analysis for an improved design of the inlet and nozzle in Tesla disc turbines," *Proc. IMechE, Part A: J. Power and Energy*, no. 224, p. 261–277, 2009.
- [77] G. M. Neckel A.L., "Influence of geometry on the efficiency of convergent–divergent nozzles applied to Tesla turbines," *Experimental Thermal and Fluid Science*, no. 62, p. 131–140, 2015.
- [78] G. H. S. G. S. A.-K. S. J. Y. D. S. F.F. Abdelall, "Pressure drop caused by abrupt flow area changes in small channels," *Experimental Thermal and Fluid Science* , no. 29, p. 425–434, 2005.
- [79] G. Geiger, "Sudden Contraction Losses in Single and Two-Phase Flow," 1964.
- [80] R. W., "An analytical and experimental investigation of multiple–disk turbines," *ASME Journal of Engineering for Power*, no. 87, p. 29–36, 1965.
- [81] C. V.P., "Assessment of Tesla Turbine Performance for Small Scale Rankine Combined Heat and Power Systems," *J. Eng. Gas Turbines Power*, no. 132, p. 1–8, 2010.
- [82] A. &. Muzychka, 2011.
- [83] L. &. Hibiki, 2017.
- [84] P. A. D. R. L. V. Dumont O., "Experimental investigation and optimal performance assessment of four volumetric expanders (scroll, screw, piston and roots) tested in a small–scale organic Rankine cycle system," *Energy*, no. 165, p. 1119–1127, 2018.